HOMOGENEOUS AND SOME INHOMOGENEOUS COSMOGRAPHIC IMPLICATIONS OF PANTHEON+ SUPERNOVA DATA; AND MORE CONSIDERATIONS OF INHOMOGENEITY EFFECTS IN COSMOLOGY

by

Mehmet Akif Feyizoğlu

B.S., Physics, Boğaziçi University, 2015

M.S., Physics, Boğaziçi University, 2019

Submitted to the Institute for Graduate Studies in
Science and Engineering in partial fulfillment of
the requirements for the degree of
Doctor of Philosophy

Graduate Program in Physics

Boğaziçi University

2025

ACKNOWLEDGEMENTS

I would first like to thank my supervisor, Prof. İbrahim Semiz, and cosupervisor, Assist. Prof. Ali Kazım Çamlıbel. Their doors were always open whenever I ran into a trouble spot or had a question about my research or writing. They consistently allowed this thesis to be my own work, but steered me in the right direction whenever they thought I needed it.

Finally, I must express my very profound gratitude to my parents for providing me with unfailing support and continuous encouragement throughout my years of study and through the process of researching and writing this thesis. This accomplishment would not have been possible without them. Thank you.

ABSTRACT

HOMOGENEOUS AND SOME INHOMOGENEOUS COSMOGRAPHIC IMPLICATIONS OF PANTHEON+ SUPERNOVA DATA; AND MORE CONSIDERATIONS OF INHOMOGENEITY EFFECTS IN COSMOLOGY

In this thesis, we revisit/reinterpret/extend the model-independent analysis method (which we now call spread - luminosity distance fitting, spread-LDF) from our previous work. We apply it to the updated supernova type Ia catalogue, Pantheon+ and recent GRB compilations. The procedure allows us, using only FLRW assumption, to construct good approximations for expansion history of the universe, re-confirming its acceleration to be a robust feature. When we also assume General Relativity, we can demonstrate, without any matter/energy model in mind, the need for (possibly nonconstant) dark energy ("GDE"). We find hints for positive pressure of GDE at $z > 1$.

We extend the use of the spread-LDF method to a particular class of radially inhomogeneous models, in which we can show that observations allow decelerating expansion. Further, we were able to modify the spread-LDF method to be used in Buchert's averaging formalism over cosmic inhomogeneities and the effective FLRW framework derived from it, showing how the observations can be analyzed in terms of the averaged quantities and the corresponding backreaction term can be estimated.

The LDF procedure also leads to the possibility of re-coordinatizing the FLRW spacetime such that the relevant metric function is a direct observable. Finally, we present an interesting example of a spacetime, which is inhomogeneous, dynamic but in a steady-state.

ÖZET

PANTHEON+ SÜPERNOVA VERİLERİNİN HOMOJEN VE BAZI İNHOMOJEN KOZMOGRAFİK ÇIKARIMLARI; VE KOZMOLOJİDE İNHOMOJENLİK ETKİLERİNE DAİR DİĞER DEĞERLENDİRMELER

Bu tezde, önceki çalışmamızda geliştirdiğimiz model-bağımsız analiz yöntemini (şimdi "dağıtık–parlaklık mesafesi fonksiyon ataması", kısaca spread-LDF) yeniden ele alıyor, yorumluyor ve geliştiriyoruz. Bu yöntemi, güncellenmiş Tip Ia süpernova kataloğu Pantheon+ ve yakın zamanda derlenmiş GRB verilerine uyguluyoruz. Yalnızca FLRW varsayımıyla, evrenin genişleme tarihini iyi bir yaklaşıklıkla yeniden inşa edebiliyor ve hızlanmanın güvenilir bir özellik olduğunu yeniden teyit ediyoruz. Genel Görelilik de varsayıldığında, herhangi bir madde/enerji modeli öne sürmeden, değişken olabilecek bir karanlık enerjiye ("GDE") ihtiyaç olduğunu gösteriyoruz. GDE'nin $z > 1$ için pozitif basınca sahip olduğuna yönelik emareler buluyoruz.

Spread-LDF yöntemini, radyal olarak homojen olmayan belirli bir uzayzaman sınıfına da uygulayarak, gözlemlerin aslında yavaşlayan bir genişlemeyle de uyumlu olabileceğini gösteriyoruz. Ayrıca yöntemi, kozmik inhomojenlikleri inceleyen Buchert ortalama formalizmine ve bundan elde edilen etkin FLRW çerçevesine uyarlayarak, gözlemlerin nasıl ortalama nicelikler cinsinden analiz edilebileceğini ve karşılık gelen geri-tepki (backreaction) teriminin nasıl kestirilebileceğini ortaya koyuyoruz.

LDF yönteminden yola çıkarak FLRW uzayzamanı yeniden koordinatlandırılıp, anlamlı metrik fonksiyonu doğrudan gözlemlenebilir yapılabilmektedir. Son olarak, homojen olmayan, dinamik fakat 'durağan hal'de olan ilginç bir uzayzaman örneği sunuyoruz.

TABLE OF CONTENTS

ACKNOWLEDGEMENTS iii
ABSTRACT iv
ÖZET v
LIST OF FIGURES ix
LIST OF TABLES xv
LIST OF SYMBOLS xvi
LIST OF ACRONYMS/ABBREVIATIONS xvii
1. INTRODUCTION 1
1.1. Measuring the Universe 1
1.1.1. The problem of inaccessible distances 2
1.1.2. Standard candles 2
1.1.3. Luminosity Distance 4
1.2. Homogeneous and Isotropic (FLRW) Cosmologies 5
1.2.1. The Cosmological Principle 5
1.2.2. Redshift and Expansion 6
1.3. Building and Realizing FLRW Cosmological Models 7
1.3.1. Model Examples 7
1.3.2. The Concordance Model 8
1.3.3. Determining Model Parameters 9
1.4. "Model-Independent Reconstruction" of FLRW Cosmologies — Our Previous Work 10
1.4.1. Fitting Pantheon Data Directly with Diverse Ansätze 11
1.4.2. Summary of Results — Transition Redshift 12
1.5. "Semi-Model-Independent Reconstruction" —Our Previous Work . . . 13
1.5.1. Assuming Gravity Theory, but No Matter/Energy Model 13
1.5.2. Summary of Results — Dark Energy Implications 14
1.6. Averaging Inhomogeneities in the Universe 15
1.6.1. Buchert Averaging 16

1.6.2. Zalaletdinov's Macroscopic Gravity 16
1.7. Update of Previous Work with Current Data 17
1.7.1. The Improved Datasets and Our Selection 18
1.7.2. New Fit Criteria 19
1.8. Application of Our Model-Independent Analysis to Radially Inhomogeneous Models 20
1.8.1. A Specific Class of Models 20
1.8.2. A Curvature Profile Yielding Zero Present Acceleration 21
1.9. Application of Our Model-Independent Analysis to Buchert Averaging . 22
1.10. Rewriting the Metric in Supernova-Adapted Coordinates 23
1.11. Time-dependent Metric With Steady Physical Content 24
2. THE DATA AND THEIR ANALYSIS FOR THE HOMOGENEOUS UNIVERSE 26
2.1. Data Sets 26
2.2. Luminosity Distance Fitting Procedure 29
2.3. Reconstruction of the Cosmic Time–Redshift Relation 35
2.4. Calculation of Scale Factor Derivatives and Expansion History 35
3. MODEL-INDEPENDENT RESULTS FOR THE HOMOGENEOUS UNIVERSE 38
3.1. Reconstruction of the Acceleration Functions 38
3.2. Selection of Physically Acceptable Reconstructions 40
3.3. Reconstructed Expansion: Acceleration and Hubble Parameter 41
4. SEMI-MODEL-INDEPENDENT ANALYSIS FOR THE HOMOGENEOUS UNIVERSE: DARK ENERGY AND ΛCDM CONSISTENCY 47
4.1. Interpreting the Reconstructed Expansion: Energy Density 47
4.2. ΛCDM Fit to Combined Distance Data and Reconstructed $H(z)$ 51
4.3. Effective Equation of State from Reconstructed Dynamics 53
4.3.1. Linearity of the Reconstructed $w(z)$ 54
4.4. CPL Fit to the Reconstructed Hubble Function 57
4.5. Reconstructing $w(z)$ of Dark Energy 59
4.6. Evidence for sign-change in the EoS of (Generalized) Dark Energy . . . 59
4.6.1. Reconstructed Equation(s) of State for Generalized Dark Energy 61

5. EXTENDING MODEL-INDEPENDENT ANALYSIS TO RADIALLY INHOMOGENEOUS SPACETIMES 66
5.1. Validity of Our Method in Inhomogeneous Geometry 66
5.2. Modified Field Equations in the Inhomogeneous Metric 68
5.3. Extracting Effective Density Parameters from Reconstructed $H(z)$ . . . 71
6. EFFECTIVE DYNAMICS FROM SPATIAL AVERAGING: BUCHERT'S FORMALISM 75
6.1. Spatial Averaging and the Buchert Formalism 75
6.2. Applicability of the FLRW-Based Reconstruction within the Buchert Averaging Framework 78
6.3. Fitting the Effective Hubble Parameter and Extracting Backreaction . 82
7. COORDINATE SYSTEM ADAPTED TO SUPERNOVA OBSERVATIONS 86
7.1. Derivatives of the Scale Factor in the Transformed Frame 88
7.2. Acceleration from Scalar Quantities: A Coordinate-Invariant Perspective 90
7.3. Scalar and Tensor Quantities in the Transformed Frame 92
7.3.1. Expansion Scalar 92
7.3.2. Hubble Function 94
7.3.3. Einstein Equation 95
7.4. Theoretical Construction and Fitting of $b(y)$ 96
7.4.1. Constructing Theoretical $b(y)$ from ΛCDM 97
7.4.2. Empirical Fitting of $b(y)$ 99
8. A DYNAMICALLY-WARPED METRIC WITH STEADY PHYSICAL PROPERTIES 104
8.1. SEC 106
9. CONCLUSION 108
REFERENCES 111

LIST OF FIGURES

Figure 2.1. Luminosity distance $d_L(z)$ versus redshift for Type Ia supernovae in the Pantheon+ compilation. 27

Figure 2.2. Luminosity distance $d_L(z)$ as a function of redshift for the full observational dataset. Black points represent Type Ia supernovae from the Pantheon+ compilation; red points represent the rescaled GRB dataset. The GRBs extend the redshift range beyond the supernova domain. 28

Figure 2.3. BIC values in Table 2.2, illustrated as a 3D bar chart for different function families and redshift variables. The main plot (right) provides a close-up view by truncating the tallest bars for better visibility of the lower values. An inset (left) shows the full-scale chart including all bar heights for completeness. 32

Figure 2.4. Pantheon+ data in terms of luminosity distance and standard redshift, the $N = 2$ to 10 fits for the first family, simple polynomials and ΛCDM model (red), and the 1-σ confidence-level of the best-fitting member ($N = 3$) of the family F1. The insets show (i) a magnified view of the right end of the data, and (ii) a bar chart of the BIC values for the F1 fits ($N = 2$ to 10). 33

Figure 2.5. Best-fitting curves from each functional family applied to the Pantheon+ dataset, using the standard redshift variable $y_0 = z$. Each curve represents the optimal model (based on BIC) within its respective function class. This comparison illustrates how different model families approximate the observed luminosity distance–redshift relation. 34

Figure 3.1. The $\ddot{a}$ functions, computed analytically for the Pantheon+ data using Eq. (2.11). The columns represents y_0 to y_6 and rows are for families F1 to F8. Blue, black and red curves are for open, flat and closed spaces respectively. All horizontal axes converted to $y_0 = z$, with the redshift range spanning $0 \leq z \leq 1.5$. 39

Figure 3.2. The $\ddot{a}$ functions, computed analytically for the Pantheon+ and GRB data using Eq. (2.11). The columns represents y_0 to y_6 and rows are for families F1 to F8. Blue, black and red curves are for open, flat and closed spaces respectively. All horizontal axes converted to $y_0 = z$, with the redshift range spanning $0 \leq z \leq 1.5$. 40

Figure 3.3. Reconstructed average acceleration $\ddot{a}(z)$, shown for the flat curvature case ($\kappa = 0$). The red curve represents acceleration reconstructed from y5-F3. 43

Figure 3.4. Reconstructed average acceleration $\ddot{a}(z)$ with 1-σ confidence band, shown for the flat curvature case ($\kappa = 0$). The shaded region reflects propagated uncertainty from the representative fit (y5-F3). The transition redshift z_T is indicated by the zero crossing. 43

Figure 3.5. Reconstructed Hubble parameter $H(z)$ obtained from the average of 24 accepted $\dot{a}(z)$ functions. The 11 curves correspond to different values of the curvature parameter κ, with the flat case ($\kappa = 0$) shown in black, open models ($\kappa < 0$) in blue, and closed models ($\kappa > 0$) in red. The present-day value for the flat case is $H_0 \approx 73.2$ km/s/Mpc. 45

Figure 3.6. Comparison between the reconstructed Hubble parameter $H(z)$ (shown as families of red and blue curves for different curvature values κ) and observational data from cosmic chronometers [27]. The red curves correspond to positive κ, and the blue curves to negative κ. 46

Figure 4.1. Reconstructed total energy density $\rho(z)$ for 11 values of the curvature parameter κ, computed using the representative fit (y5–F3). Black curve corresponds to the flat case $\kappa = 0$; red and blue represent positive and negative curvature, respectively. 48

Figure 4.2. Flat curvature case: total energy density $\rho(z)$(black), with 1-σ upper and lower bounds (dashed-red curves) propagated from the representative fit. Each is compared with a scaled matter-only evolution $\rho_m(z) = \rho_{m,0}(1+z)^3$ (dashed-blue curves), matched at $z \approx 1$. The shaded region between $\rho(z)$ and the matter curve at low redshift highlights the minimum extra energy density required beyond matter. 50

Figure 4.3. Reconstructed Hubble parameter $H(z)$ from the average of 24 accepted $\dot{a}(z)$ curves (with $\kappa = 0$), shown with a 1-σ error band derived from the representative y5-F3 function. The solid black curve shows the best-fit flat ΛCDM model, yielding $H_0 \approx 72.8$ km/s/Mpc, $\Omega_m \approx 0.39$. 53

Figure 4.4. Reconstructed effective equation of state parameter $w(z) = p(z)/\rho(z)$ using the representative function (y5–F3) for the flat curvature case. The present-day value is $w(0) = -0.64$, indicating accelerated expansion. At higher redshifts, $w(z)$ increases toward 0, consistent with a matter-dominated universe. 55

Figure 4.5. Reconstructed effective equation of state $w(z)$ using the representative fit (y5-F3) for the flat case. The dots shows the reconstructed $w(z)$; the black line is the best-fit linear model $w(z) \approx -0.63 + 0.65z$. The near-linearity supports the use of low-order parametrizations for describing the equation of state in this redshift range. 56

Figure 4.6. Reconstructed Hubble parameter $H(z)$ from the average of 24 accepted $\dot{a}(z)$ functions (red), with 1-σ uncertainty band derived from the representative y5–F3 reconstruction (dotted red curves, shaded region). The best-fit CPL model is shown in black. 58

Figure 4.7. Reconstructed average dark energy density $\rho_{\rm DE}(z)$ for different values of $\Omega_m \in$ (0.2, 0.25, 0.3, 0.35, 0.4, 0.45). Each curve is obtained by subtracting the matter contribution $\rho(0)\Omega_m(1+z)^3$ from the total average reconstructed $\rho(z)$. The curves are ordered from top to bottom according to increasing Ω_m. 60

Figure 4.8. Reconstructed equation of state parameter $w_{\rm DE}(z)$, obtained from the previously derived $\rho_{\rm DE}(z)$ and the reconstructed pressure $p(z)$. The curves correspond to the same $\Omega_m$values as in Figure 4.7: (0.2, 0.25, 0.3, 0.35, 0.4, 0.45), with colors matched accordingly. 61

Figure 4.9. CPL parametrization of the dark energy equation of state $w(z)$ for various values of w_a, with w_0 fixed at -1. The curves illustrate the impact of different w_a values in the range -2, -1.5, -1, -0.5, 0, 0.5, 1, 1.5, 2 on the redshift evolution of $w(z)$. 62

Figure 4.10. Average reconstructed pressure for 11 values of the curvature parameter κ. Black curve correnspponds to flat case; red and blue represent positive and negative curvature, respectively. 63

Figure 4.11. Reconstructed pressure as a function of redshift for all selected functions. 63

Figure 4.12. Parametric function pressure in terms of dark energy density. The curves correspond to the same Ω_m values as in Figure 4.7: (0.2, 0.25, 0.3, 0.35, 0.4, 0.45), with colors matched accordingly. 64

Figure 5.1. Average reconstructed acceleration $\ddot{a}(z)$ for the chosen inhomogeneous profile. The result remains negative over the entire redshift range, indicating that the observed expansion history may be explained without invoking accelerated expansion in this model. . . . 72

Figure 5.2. Reconstructed Hubble parameter $H(z)$, obtained by averaging the 24 accepted $\dot{a}(z)$ functions within the inhomogeneous model using $b(r, \epsilon = 5.2)$. The shaded region represents the 1-σ confidence band derived from the y5–F3 representative function. The black curve shows the best-fit model of the form $H(z)/H_0$, with parameters given in the text. 73

Figure 6.1. Reconstructed effective Hubble parameter $H_D(z)$, obtained by averaging the 24 accepted $\dot{a}(z)$ functions. The shaded region represents 1-σ confidence band derived from the y5–F3 representative function. The black curve shows the best-fit model of the form $H_D(z) = H_{D_0}\sqrt{\Omega_m(1+z)^3 + \Omega_X(1+z)^{-n}}$. 85

Figure 7.1. Comparison of the coordinate-based (black) and coordinate-invariant (red, thick) computations of the cosmic acceleration $\frac{\ddot{a}}{a}(y)$, both using the ΛCDM-derived $b(y)$. The two curves are numerically indistinguishable, confirming the internal consistency of the two reconstruction approaches. The transition point $y_T \approx 1782$ is identical in both cases. 100

Figure 7.2. Comparison of the observationally transformed data (y_i, b_i), red curve is the theoretical $b(y)$ curve derived from a flat ΛCDM model, and black curve is the empirical Padé fit. All curves closely agree for $y < 2000$, but begin to diverge at larger values of y. This subtle divergence leads to significant differences in the second derivative $\ddot{a}(y)$, as shown in Figure 7.3 101

Figure 7.3. Acceleration profile $\ddot{a}(y)$ computed from two fitted models of $b(y)$. The red curve corresponds to the ΛCDM-predicted $b(y)$; the black curve is computed from the empirical Padé fit. Although both models produce nearly indistinguishable b(y) curves (Figure 7.2), the resulting acceleration profiles differ significantly, showing the high sensitivity of $\ddot{a}(y)$ to the form of $b(y)$. 102

LIST OF TABLES

Table 2.1. The 8 different families used in fits. y can be any one of the redshift parameters described previously (y_0 to y_6), $P_N(y)$ is the N^{th} order polynomial with zero constant term (except when using $y_6 = u$), $u(y)$ is $(1 + z)$ expressed in terms of y, $\tilde{P}(y,\ M,\ N)$ is the Padé approximant in variable y and orders M & N; and c & d are constants. 30

Table 2.2. The best fits for the Pantheon+ and GRB data. Each cell displays the internal label(s) of the best-fitting member of the row's family for the column's redshift variable, and the fit's BIC value. 31

LIST OF SYMBOLS

c	Speed of light
d_L	Luminosity distance
G	Gravitational constant
H	Hubble parameter
I	Intensity
k	Curvature parameter
L	Luminosity
p	Pressure
$\tilde{P}$	Padé approximant
R	Ricci scalar
q	Deceleration parameter
Q_D	Kinematical Backreaction
V	Volume
w	Equation of State
z	Redshift
α	$f(R)$ parameter
Θ	The Expansion Scalar
κ	Curvature function
λ	Wavelength
Λ	Cosmological constant
ρ	Energy density
$\sigma_{\alpha\beta}$	The Shear Tensor
$\omega_{\alpha\beta}$	The Rotation Tensor
Ω	Energy density fraction
Ω^{eff}	Effective Energy density fraction

LIST OF ACRONYMS/ABBREVIATIONS

CDM	Cold Dark Matter
CMB	Cosmic Microwave Background
CPL	Chevallier–Polarski–Linder
DE	Dark Energy
DM	Dark Matter
EoS	Equation of State
FLRW	Friedmann–Lemaître–Robertson–Walker
GDE	Generalized Dark Energy
GR	General Relativity
GRB	Gamma Ray Burst
MD	Matter Dominated
MPC	Mega parsec
SEC	Strong Energy Condition
SN	Supernova
SN Ia	Supernova type Ia

1. INTRODUCTION

Starting with the first human being who looked up at the night sky, people have wondered about the nature of the tiny points of lights above, their relationship to each other and to the Earth. The observation that almost all of them make uniform circular motion around the same center and with the same period gave rise to the concept of a geocentric planetary system surrounded by the celestial sphere carrying the "stars". The model of the planetary system was comprised of the periods and relative radii of the orbits of the "planets', eventually culminating in the Ptolemaic system, which added epicycles, equants and excentrics, with distances still relative. From the early versions of the model to the eventual Ptolemaic model, the distance to the celestial sphere, equivalently, the size of the universe was left unspecified, even relatively; but the implication was that all stars were at the same distance from the Earth, possibly somewhat farther away than Saturn, the planet then thought to be the farthest planet.

Galileo's telescopic observations changed this. His telescope showed stars not visible to the naked eye, which implied they were farther away than those that are, if one (reasonably) assumes that all stars are more or less the same. Hence it became legitimate to wonder how far each individual star is, at least relative to each other; a much larger universe whose three-dimensional structure needs to be ascertained.

1.1. Measuring the Universe

The new concept of the universe was not only heliocentric, but also much larger than the orbit of Saturn. The question was, how much larger, if not in fact infinite. So one needs to measure distances to individual stars, which obviously are not accessible directly.

1.1.1. The problem of inaccessible distances

The problem of measuring inaccessible distances/lengths has been with us for a while, e.g. determining the width of a river before it has been crossed, or the height of a distant mountain. The first answer that comes to mind utilizes geometry: the height of a pole or tree can be determined by measuring the length and angle of its shadow. The triangulation involved is built-in into the binocular vision of humans as well as many predatory animals, can be applied to the river and mountain problems mentioned above; and yes, stellar distances.

When the relevant angle is small, the method is called parallax; and was applied in the astronomical context first by Tycho Brahe to determine the distance to the Moon. The first stellar distances were determined in 1830's via parallax [1], constituting the first quantitative enlargement of the lower-bound on the size of the universe beyond the solar system. However, ground-based telescopes can measure parallaxes only up to about 100 light-years, even modern space observatories (first Hipparcos, then Gaia) can improve this by only one or two orders of magnitude.

On the other hand, the ideas of the galaxy, and that the universe may be much larger than our galaxy ,have also been around for quite a while, at least since Wright and Kant suggested them in 1755. Since all stars whose parallaxes can be determined are quite close (only Gaia's range approaches the size of our galaxy, but is still smaller), the second part calls for an alternative approach to estimate extragalactic distances.

1.1.2. Standard candles

The alternative approach is implied in the post-Galileo (or post-telescope) argument: Objects seen fainter must be farther away, if they are intrinsically identical. However, it was soon found out that stars do show a lot of variation (today, we know that the radiative power ("luminosity" L in astronomy parlance) can vary by about 10 orders of magnitude among stars). So to implement this approach, we need special

objects whose luminosities are known to be identical, or at least, can be determined independent of their observed apparent brightness. Such objects are called "standard candles", the term therefore being a key concept in observational cosmology.

Their utility arises from the inverse-square law: The distance d_L to a standard candle can be found in terms of its known intrinsic luminosity L and its apparent brightness (or radiative flux) F via

$$F = \frac{L}{4\pi d_L^2}. \tag{1.1}$$

The first objects used as standard candles were Cepheid variables, a class of pulsating stars where the pulsation period is monotonically related to the absolute luminosity. The monotonicity was discovered by Leavitt during her painstaking investigation of Cepheids in the Large Magellanic Cloud (since all being in LMC, their distances are approximately the same, hence apparent brightness is directly proportional to absolute luminosity) and after calibration, was used by Edwin Hubble to estimate distances to nearby galaxies (finally proving that other galaxies exist!).

The standard candles we will be dealing with in this thesis are type Ia supernovae (SNe Ia), which are unbinding thermonuclear explosions of white dwarfs (WD) in accreting binary systems, exhibiting a relatively uniform peak luminosity across different events. The uniformity comes from the feature that for the whole WD to explode, it must be already near the Chandrasekhar mass and the accretion must push it over that limit, making all of them nearly the same mass at explosion. In an accreting WD of any other mass, eventually the accreting material will undergo fusion, giving rise to a surface explosion instead of body, hence a weaker explosion giving rise to a much fainter (and nonstandard) nova. However, SNe Ia provide a consistent measure of absolute brightness after standardization using empirical correlations such as the width-luminosity or color-luminosity relationships [2]. They are also bright enough

to be seen in very far galaxies, in some sense farther than halfway across the (visible) universe, making them particularly valuable tools for cosmology.

1.1.3. Luminosity Distance

With the advent of General Relativity (GR) in the early 20th century, it became conceivable that the universe is not Euclidean, and/or not static. The distance defined via Eq. (1.1) is the distance only if the universe is static and spatially Euclidean. However, in curved space, in fact, curved spacetime, (a dynamic spacetime is curved even if the spatial sections are flat), the "actual distance at a given time" (proper distance) cannot be measured. Moreover, the concept of "at a given time" does not have a unique meaning, unless the spacetime satisfies certain symmetries (see next section).

So, in a general spacetime, Eq. (1.1) does not give us the distance, because the distance is not operationally meaningful. On the other hand, we *cannot* do any better, the distance calculated via Eq. (1.1) is still a measure of distance. This measure is called *luminosity distance* d_L, both to emphasize that it is not the distance, and because it is calculated based on the source luminosity.

Observationally, supernova data are often presented in terms of the distance modulus μ, defined as

$$\mu = m - M, \tag{1.2}$$

where m is the apparent magnitude and M is the absolute magnitude. The luminosity distance in parsecs is then given by

$$d_L = 10^{(\mu+5)/5}\text{pc}, \tag{1.3}$$

Where parsec (pc) is astronomers' preferred distance unit, and is equal to 3.26 light-years (LY).

1.2. Homogeneous and Isotropic (FLRW) Cosmologies

General Relativity (GR) mentioned above is very complicated: Its fundamental law, the Einstein Field Equations (EFE) correspond to 10 coupled *nonlinear* partial differential equations (cf. Maxwell eq's, 8 coupled linear PDE's) for 10 variables, which are elements of the metric (equivalently, line element) describing spacetime geometry mathematically. Because of this complexity, to find any meaningful solution for the spacetime in the cosmological context, one needs some simplifying assumption(s). These simplifying assumption(s) form the Cosmological Principle.

1.2.1. The Cosmological Principle

The cosmological principle postulates that the universe is, on sufficiently large scales, both homogeneous (the same at every point) and isotropic (the same in every direction). This is not a fundamental law of nature but a simplifying assumption, intellectually an extension of the Copernican Principle: Not only are we not at a special point in the universe, there is no special point or direction in the universe. While the principle at its time of formulation (late 1910's) was purely intellectual, a pragmatic simplification without any observational support, later observations, notably the isotropy of the cosmic microwave background (CMB) and the large-scale distribution of galaxies [3] provide justification for it.

Under this principle, the most general form of the spacetime metric is the Friedmann–Lemaître–Robertson–Walker (FLRW) metric

$$ds^2 = -c^2dt^2 + a(t)^2\left[\frac{dr^2}{1-kr^2} + r^2(d\theta^2 + \sin^2\theta d\psi^2)\right], \tag{1.4}$$

where $a(t)$ is the scale factor, and k is the curvature parameter: $k = 0$ for flat space,

$k = +1$ for closed (spherical) space, and $k = -1$ for open (hyperbolic) space. The coordinates are *comoving*, i.e. typical objects stay at constant spatial coordinates.

Even though the Cosmological Principle is motivated by the complexity of EFE, it is independent of GR; it and the FLRW metric form are valid for any *metric theory*.

1.2.2. Redshift and Expansion

Observations of celestial objects, including stars and galaxies, show shifts of spectral lines, interpreted usually as Doppler shifts due to the motion of the sources. Hubble made first determinations of spectral shifts of other galaxies, and found that with a few exceptions of relatively nearby galaxies, all shifts were towards the red end of the spectrum; and the inferred recession velocities were proportional to the inferred distances (via Cepheids, see Sect.1.1.2); a relation expressed as Hubble's law

$$v = Hd \tag{1.5}$$

where H, independent of the distance d, was called Hubble constant. Since all galaxies are receding away from each other, this leads to the concept of the expansion of the universe.

Assuming the Cosmological Principle leads one to think in terms of the FLRW metric, where the expansion of the universe means increase of a(t) in (1.4). As discussed above, the typical objects (galaxies) in the universe are really "at rest", hence one cannot really ascribe the redshift to motion. One can, however, analyze the propagation of light, and show that it does redshift due the expansion as

$$\frac{f_{\text{emit}}}{f_0} = 1 + z = \frac{a_0}{a(t_{\text{emit}})}, \tag{1.6}$$

where z is the redshift, the label 0 refers to today and the label emit to the time of

emission. Also the expansion of the universe is expressed as

$$H(t) = \frac{\dot{a}(t)}{a(t)}, \tag{1.7}$$

where $H(t)$ is called the Hubble parameter and agrees with the Hubble "constant" when only the relatively nearby galaxies are investigated, as Hubble did.

For farther galaxies, we look both further into the past where $a(t)$ is different from today, and also at scales where the spatial curvature, if any, is relevant. Hence, it is not possible to interpret the redshift in terms of recession speed, nor can the distance be determined as discussed in Sect. 1.1.3. Instead, all we have is a relation between the redshift and luminosity distance, a dependence $d_L(z)$ instead of Eq. (1.5). The observable function $d_L(z)$ is what encapsulates the information about the expansion history of the universe, and part of this thesis will be about how we can extract that information from the data, and how much information can be extracted.

1.3. Building and Realizing FLRW Cosmological Models

Once the metric is mostly fixed by the cosmological principle, the function $a(t)$ and the three-valued parameter k describe the universe, hence building a model entails finding/predicting/claiming this function and parameter. Usually, one begins by assuming a gravitational theory (often GR) and assumptions about the matter/energy content; and solves the equations of the theory to get $a(t)$ and k. Finally one has to compute observable consequences, e.g. the $d_L(z)$ function from $a(t)$ and k, and compares with observations.

1.3.1. Model Examples

As stated above, usually one assumes GR is valid, i.e. dynamics is introduced by Einstein's field equations. The Einstein Tensor for the FLRW metric is diagonal, and the galaxies, which are typical objects in the universe, are at rest in the FLRW coor-

dinates by design (i.e. the coordinates are comoving). Hence the energy-momentum tensor in EFE can be modeled as a perfect fluid at rest, or a superposition of them. We do know that there is radiation and matter (baryonic or dark, this is irrelevant for this purpose) in the universe, and dark energy can also be imagined (see next section). The various components contribute differently to the evolution of the universe. For instance, for flat FRW:

- Radiation dominates early, leading to $a(t) \propto t^{1/2}$.
- Matter domination leads to $a(t) \propto t^{2/3}$
- Dark energy (in the form of a cosmological constant) leads to exponential expansion $a(t) \propto e^{Ht}$

These different components would dominate at different epochs [4], the general solution for $a(t)$ being complicated but should approach the above-mentioned simple forms in epochs in which they are dominant. Or, to get an approximate model, one can try to match different simple forms at the times of transition between epochs.

1.3.2. The Concordance Model

The current standard model of cosmology is the ΛCDM model. It assumes:

- General Relativity as the correct theory of gravity,
- A cosmological constant (Λ) as dark energy,
- Cold dark matter (CDM) and ordinary baryonic matter,
- Spatial flatness (typically supported by CMB data).

The dark matter is required since the dynamically observed mass is more than the visible mass, and dark energy is required since the SN Ia observations are interpreted in this framework as an acceleration of the expansion of the universe. The parameters of the model —such as Ω_m, Ω_Λ, and H_0—are tuned to fit a wide range of observations: CMB anisotropies, baryon acoustic oscillations, large-scale structure, and Type Ia su-

pernovae [5]. The commonly quoted breakdown is approximately 5% baryonic matter, 25% dark matter, and 70% dark energy, though precise values vary slightly depending on the dataset and method of inference. The contribution of radiation is negligible today, hence it does not appear among the parameters. However, the early universe in the ΛCDM model is radiation-dominated, as in many other cosmological models.

1.3.3. Determining Model Parameters

In practice, cosmological parameters are extracted by fitting models like ΛCDM to observational data ([6] and [7]). For example:

- Supernova data constrain the luminosity distance–redshift relation,
- The CMB constrains the total energy content and geometry,
- Baryon acoustic oscillations provide a standard ruler for distance measurements.

These fits are performed using statistical techniques such as maximum likelihood estimation, χ^2 minimization, or Bayesian inference [8].

As discussed in the introduction to this section, a particularly important theoretical prediction of cosmological models is the luminosity distance–redshift relation, which connects observables to model parameters. In a homogeneous, isotropic universe with spatial curvature, the luminosity distance is given by

$$d_L(z) = (1+z)\frac{c}{H_0} S_k\left(\int_0^z \frac{dz'}{E(z')}\right), \tag{1.8}$$

where $S_k(x)$ is $\sin(x)$, x, $\sinh(x)$ for $k = 1, 0, -1$ [4].

In particular, in the ΛCDM model

$$E(z) = \frac{H(z)}{H_0} = \sqrt{\Omega_m(1+z)^3 + \Omega_r(1+z)^4 + \Omega_k(1+z)^2 + \Omega_\Lambda}. \tag{1.9}$$

Hence, by comparing the theoretical $d_L(z)$ prediction with observed values of $d_L(z)$, cosmologists can constrain the cosmological parameters that govern the expansion of the universe in this model.

1.4. "Model-Independent Reconstruction" of FLRW Cosmologies — Our Previous Work

In standard cosmological analyses, the expansion history of the universe is reconstructed by assuming a specific cosmological model — such as ΛCDM — and fitting its predicted observables to data. However, this approach tightly couples observational inferences to theoretical assumptions. An alternative strategy is to begin from observational data directly and attempt to reconstruct cosmological dynamics with minimal assumptions, a strategy often referred to as cosmography or model-independent reconstruction [9], [10].

In a previous study [11], Semiz & Çamlıbel developed such a method using Type Ia supernova data, aiming to reconstruct the expansion history of the universe directly from observations without presuming a specific matter content or initially a theory of gravity (but no assumed equation of state). The method relies only on the metric nature of gravity and the standard cosmological framework of a homogeneous and isotropic universe. The key idea is to treat the luminosity distance function $d_L(z)$ as an observable input, and to analytically derive time derivatives of the scale factor $a(t)$ as functions of redshift, enabling reconstruction of the expansion rate, acceleration, and higher-order kinematic quantities. After model-independent results, minimal implications (without matter/energy assumptions, i.e. equation of state), of a given theory of gravity can also be derived. We later [12] applied the same method for more recent and significantly better data, with improved fitting method and also considering an alternative theory of gravity in the second part.

1.4.1. Fitting Pantheon Data Directly with Diverse Ansätze

Our procedure begins with the observation that the relation between the luminosity distance and the scale factor in the FLRW metric can be inverted to express cosmic time t as a function of redshift z, given a candidate form for $d_L(z)$. The scale factor and its derivatives can then be written as analytical functions of redshift via chain-rule manipulations. This yields expressions for $\dot{a}(z)$, $\ddot{a}(z)$ and higher derivatives, without requiring explicit assumptions about the energy content of the universe or the underlying gravitational field equations.

To perform this reconstruction, we adopt a hybrid numerical–analytical method. A wide variety of functional forms (or ansätze) for the luminosity distance were considered. These included polynomial functions, Padé approximants, and exponential-polynomial hybrids, each evaluated in several redshift parameterizations such as z, $z/(1+z)$, and $\ln(1+z)$. Each candidate function was fit to the observed Pantheon dataset [13], which at the time contained 1048 Type Ia supernovae over the redshift range $0 < z < 2.3$.

To select the most suitable models, we employed a goodness-of-fit criterion based on the χ^2-probability. Importantly, we did not fix the number of free parameters in advance; instead, we allowed the data to determine the optimal complexity of each fit. The spatial curvature parameter κ was treated as an external variable, scanned over a reasonable range consistent with current constraints.

Although the analysis was designed to be fully model-independent, we found that the supernova data alone, particularly at higher redshifts, introduced noise and instabilities in the second derivatives $\ddot{a}(z)$. To mitigate this, we supplemented the data with a small number of gamma-ray burst (GRB) luminosity distance measurements, extending the redshift coverage and improving the stability of the reconstructed acceleration curves. While the reported GRB data are derived using calibrations within the ΛCDM

cosmological model, their number was limited and it was argued that their inclusion will disturb the model-independent nature of the study very little.

1.4.2. Summary of Results — Transition Redshift

The results of the analysis provided a direct, model-independent picture of the universe's expansion history. After fitting 48 different function–variable combinations and deriving the corresponding $\dot{a}(z)$ and $\ddot{a}(z)$, we constructed acceleration profiles for the universe's scale factor. These profiles consistently showed a transition from deceleration to acceleration at a redshift around

$$z_T = 0.44^{+0.04}_{-0.03}, \tag{1.10}$$

assuming a flat spatial geometry. The transition redshift shifted slightly for positive or negative curvature but remained within a narrow, robust range.

The inclusion of GRB data was particularly important for clarifying the high-redshift behavior of the acceleration function. Without it, some candidate functions yielded physically implausible oscillations or multiple transitions. With GRBs included, a more coherent picture emerged: the universe was decelerating in the past, underwent a smooth transition, and is accelerating today. Notably, this conclusion was reached without invoking a specific form of dark energy or a particular gravity theory.

This work demonstrated that key features of cosmic expansion — including the current acceleration — can be inferred directly from data under minimal assumptions. It laid the groundwork for subsequent refinements and generalizations, including those presented in this thesis.

1.5. "Semi-Model-Independent Reconstruction" —Our Previous Work

While model-independent reconstruction provides valuable insight into the expansion history of the universe, it leaves open the interpretation of the underlying energy content. In a second stage of our previous work [11, 12], we introduced minimal theoretical assumptions in order to extract further information. Specifically, we assumed the validity of general relativity (GR) and a homogeneous FLRW geometry, but did not impose any specific model for the matter or energy content of the universe.

This approach retains a significant degree of generality while enabling the use of the Einstein field equations to interpret the reconstructed expansion history in terms of the total energy density.

1.5.1. Assuming Gravity Theory, but No Matter/Energy Model

With the Hubble parameter $H(z)$ and scale factor derivatives $\dot{a}(z)$, $\ddot{a}(z)$ obtained from the reconstructed luminosity distance, we applied the Friedmann equations:

$$\rho(z) = \frac{3c^2}{8\pi G}(H^2(z) + \frac{kc^2}{a^2(z)}), \tag{1.11}$$

$$p(z) = -\frac{c^2}{8\pi G}\left(\frac{kc^2}{a^2(z)} + H^2(z) + 2\frac{\ddot{a}(z)}{a(z)}\right) \tag{1.12}$$

to determine the energy density $\rho(z)$ and pressure $p(z)$ of the universe as functions of redshift, without requiring a decomposition into matter, radiation, or dark energy components.

From these, we computed the effective equation of state parameter:

$$w(z) = \frac{p(z)}{\rho(z)}, \tag{1.13}$$

which encapsulates the total dynamical behavior of the universe's energy content. This

parameter provides a direct test of whether the expansion requires a dark energy–like component (with $w \approx -1$) or can be explained by conventional matter alone.

Additionally, we compared the reconstructed energy density $\rho(z)$ with the form $\rho_m(z) = \rho_{m,0}(1+z)^3$, which corresponds to pressureless matter. The comparison allowed us to estimate a lower bound on the dark energy density and an upper bound on the matter density, assuming flat geometry and GR. One can easily get similar results for nonzero values of curvature.

Notably, this framework can be naturally extended to alternative gravity theories. For example, in earlier work we briefly investigated reconstruction within Starobinsky gravity [14], characterized by an $f(R)$ modification of the Einstein-Hilbert action:

$$f(R) = R + \alpha R^2. \tag{1.14}$$

In this context, the cosmic dynamics are altered not only by higher-order curvature terms but also by higher derivatives of the scale factor. We searched for values of the parameter α that yield an effective energy density evolving similarly to pressureless dust, i.e., scaling as $(1+z)^3$. While such extensions lie beyond the scope of the present analysis, they illustrate how higher-order curvature corrections and associated dynamical terms can mimic late-time cosmic acceleration without invoking an explicit cosmological constant or dark energy component.

1.5.2. Summary of Results — Dark Energy Implications

Our results indicated that the reconstructed total energy density $\rho(z)$, derived from the observed expansion history, cannot be explained by matter alone. Specifically, we found a significant deviation between $\rho(z)$ and the matter-only scaling $(1+z)^3$ at low redshifts. The excess energy density required to match the observed expansion is consistent with a dark energy component.

At redshift $z = 0$, the reconstructed quantities yielded:

$$\Omega_m^{max} \approx 0.48, \quad \Omega_\Lambda^{min} \approx 0.52 \tag{1.15}$$

where the approximations reflect the interpretation that these are bounds, not best-fit model parameters. These values are consistent with those derived from ΛCDM fits, despite being obtained without assuming the existence of a cosmological constant.

These findings suggest that, under the assumption of general relativity, an additional negative-pressure component is required to explain the observed acceleration. The analysis thus provided semi-model-independent evidence for dark energy, with fewer assumptions than traditional ΛCDM fitting.

1.6. Averaging Inhomogeneities in the Universe

The standard cosmological model assumes that the universe is homogeneous and isotropic on large scales, leading naturally to the FLRW metric. However, the universe is in fact highly inhomogeneous at small and intermediate scales, featuring galaxies, clusters, voids, and filaments. While these structures are typically treated as perturbations on a smooth background, it remains an open question whether their effects might accumulate — especially in a nonlinear theory like general relativity — to influence the average dynamics of the universe in a non-negligible way.

The possibility that inhomogeneities could mimic or contribute to the observed acceleration of the universe has motivated the development of spacetime averaging frameworks. These approaches attempt to derive the effective large-scale behavior of an inhomogeneous universe without assuming a perfectly smooth background from the outset.

1.6.1. Buchert Averaging

One of the most widely studied frameworks for averaging inhomogeneous cosmologies is the Buchert formalism [15]. This approach considers scalar quantities (such as the local expansion rate and energy density) on spatial hypersurfaces and defines volume averages over a comoving domain. The resulting effective equations take a form similar to the FLRW equations but include additional terms that arise from the inhomogeneity of the local expansion and curvature. These extra terms are collectively referred to as the backreaction.

The effective scale factor $a_D(t)$, describing the average volume evolution of the domain, satisfies modified Friedmann-like equations that include:

- The averaged energy density,
- The average spatial curvature, and
- A kinematical backreaction term $Q_D(t)$, which captures the variance in local expansion rates and shear.

One intriguing implication of the Buchert formalism is that the backreaction term Q_D could, in principle, become large enough to drive accelerated expansion, even in the absence of a cosmological constant or exotic energy components. This has led to speculation that cosmic acceleration might be at least partially an artifact of interpreting inhomogeneous observations within a homogeneous model.

A detailed overview of the Buchert formalism, its assumptions, and its application to our reconstructed expansion history is provided later in this thesis.

1.6.2. Zalaletdinov's Macroscopic Gravity

An alternative and more covariant approach to averaging is Zalaletdinov's macroscopic gravity [16], [17]. This framework attempts to perform a rigorous averaging of

the full Einstein equations, including tensorial quantities, rather than just scalars. The result is a set of effective macroscopic field equations that include correlation terms representing the influence of small-scale inhomogeneities.

While conceptually appealing, macroscopic gravity is significantly more complex and less widely applied than the Buchert approach. It also faces challenges in physical interpretation and practical implementation. Nevertheless, it remains an important contribution to the theoretical study of averaging in general relativity.

In this thesis, we focus primarily on the Buchert formalism, as it offers a tractable and observationally relevant framework for testing whether cosmic acceleration might arise from averaging effects rather than requiring a separate dark energy component.

1.7. Update of Previous Work with Current Data

The model-independent and semi-model-independent framework developed in our earlier work proved successful in reconstructing the expansion history of the universe and placing bounds on dark energy without assuming a specific cosmological model. However, the precision of any reconstruction is ultimately limited by the quality and quantity of the observational data. Since our original analysis, significant improvements have been made in supernova and gamma-ray burst datasets, motivating a thorough revision and expansion of our method.

In this thesis, we revisit and extend our reconstruction using the Pantheon+ supernova compilation and a more recent GRB dataset, alongside several methodological enhancements. Our goal is not only to improve the robustness and precision of the reconstruction but also to explore new physical interpretations of the results, including applications to inhomogeneous and averaged cosmologies.

1.7.1. The Improved Datasets and Our Selection

The most substantial update to the supernova dataset is the release of the Pantheon+ compilation [18], which includes over 1500 spectroscopically confirmed Type Ia supernovae across the redshift range $0.001 < z < 2.26$. Compared to the original Pantheon set, Pantheon+ provides:

- A 50% increase in data volume,
- Improved calibration using SH0ES Cepheid hosts,
- Reduced systematic uncertainties.

These enhancements enable a more precise reconstruction of the expansion history, especially in the critical redshift range $z < 1$ where the acceleration–deceleration transition occurs.

To improve stability at high redshifts (where supernovae are sparse), we –as in previous work– incorporated a set of gamma-ray burst (GRB) [19] luminosity distance measurements extending up to $z \sim 8$. While GRBs are not strictly model-independent due to their calibration methods, their inclusion constitutes only about 10% of the dataset and primarily serves to anchor the high-redshift behavior of the fits, suppressing unphysical oscillations in second derivatives.

However, we found that different GRB calibrations can bias the reconstruction, particularly in determining the transition redshift. To address this, we compared the slopes of two independent GRB datasets and introduced a rescaling procedure to align their overall behavior. This adjustment ensured consistency with our earlier methodology and stabilized the reconstruction without introducing obvious systematic bias.

The final dataset used in this work consists of:

- The full Pantheon+ sample [18],

- A rescaled, high-redshift GRB set,
- Distance moduli converted to luminosity distances using a fixed absolute magnitude M, calibrated via SH0ES [20].

1.7.2. New Fit Criteria

With the increased volume and precision of the Pantheon+ data, our previous reliance on χ^2-based p-values for model selection became unreliable. In particular, we observed that χ^2 goodness-of-fit metrics become overly sensitive in large datasets, frequently penalizing valid fits due to small residuals.

To overcome this, we adopted the Bayesian Information Criterion (BIC) as our new model selection tool. BIC not only evaluates the goodness of fit but also incorporates a penalty term for model complexity, making it well-suited for distinguishing between competing functional forms in a statistically robust way.

We applied BIC to a wide range of candidate functions — the same eight function families and six redshift reparameterizations as in our earlier work — resulting in 48 different fits to the combined dataset. For each of the function/parameter options, the best-fit member was selected based on minimum BIC value. Some fits produced oscillatory behaviour in the $\ddot{a}(z)$ curves. Since the $z-$values and signs of the oscillations were not consistent between different curves showing oscillations, we deemed the oscillations unphysical, and eliminated fits giving rise to them. This left only those reconstructions that produced smooth, monotonic acceleration curves with a single deceleration–acceleration transition.

These updated fitting procedures, combined with the high-precision Pantheon+ data and calibrated GRB support, form the basis of the improved model-independent reconstruction presented in this thesis. They also enable more reliable comparisons to ΛCDM, tests of inhomogeneous geometry, and evaluation within the Buchert averaging framework.

1.8. Application of Our Model-Independent Analysis to Radially Inhomogeneous Models

A key assumption in standard cosmology is large-scale spatial homogeneity. While this is supported by observations on the largest scales, the possibility remains that small but systematic deviations from perfect homogeneity — for now in the radial direction (i.e., along the line of sight) — could alter the inferred expansion history. In this context, even mild inhomogeneities in curvature or geometry might mimic effects traditionally attributed to dark energy.

To investigate this possibility, we apply our model-independent reconstruction framework to a generalized class of FLRW-like spacetimes that allow for radial inhomogeneity in spatial curvature. This extension does not require abandoning the metric structure of the universe or assuming a full Lemaître-Tolman-Bondi (LTB) model, but instead introduces a minimal generalization that retains much of the symmetry of the FLRW metric while testing the impact of curvature gradients.

1.8.1. A Specific Class of Models

In this analysis, we consider a modified spatial geometry in which the spatial curvature is allowed to vary radially, encoded by a curvature function $b(r)$, where r is the comoving radial coordinate. The modified metric takes the form

$$ds^2 = -c^2dt^2 + a(t)^2\left[b(r)^2dr^2 + r^2d\Omega^2\right] \tag{1.16}$$

which reduces to the standard FLRW form when $b(r)^2 = 1/(1 - kr^2)$. By generalizing the curvature in this way, we allow for small deviations from homogeneity while maintaining spherical symmetry and preserving the notion of a cosmic scale factor.

This framework permits an effective, observationally anchored reconstruction of the expansion history even in the presence of curvature gradients. We adapt our

previously developed methodology — fitting $d_L(z)$, reconstructing $\dot{a}(z)$ and $\ddot{a}(z)$, and applying kinematic relations — to extract how the presence of radial inhomogeneity modifies the inferred energy density and acceleration behavior.

The key question we aim to address is: Can a radially varying spatial curvature function explain some or all of the observed acceleration of the universe, without invoking dark energy? Or conversely, how robust is the need for dark energy against small deviations from homogeneity?

By applying our model-independent reconstruction to this class of geometries, we are able to test whether the conclusions drawn from standard FLRW analyses persist in mildly inhomogeneous settings, or whether they are sensitive to curvature structure along the line of sight.

1.8.2. A Curvature Profile Yielding Zero Present Acceleration

To explore the limits of how radial inhomogeneity might influence the interpretation of cosmic acceleration, we focused on a specific case: a curvature function $b(r)$ constructed to yield zero or negative present-day acceleration with the reconstructed functions. Rather than aiming to construct a fully realistic cosmological model, the goal was to examine whether such a curvature profile could, at least in principle, reproduce the observed expansion history without requiring a dark energy component.

Using the expansion history reconstructed from the Pantheon+ and GRB data, we computed the Hubble parameter $H(z)$ and used it in conjunction with the radially inhomogeneous metric to extract the effective dynamical quantities. We then applied the generalized Friedmann equations to infer the corresponding effective energy density parameters, Ω_m^{eff} and $\Omega_\Lambda^{\text{eff}}$, across redshift.

This targeted exploration illustrates that the inference of dark energy — while strongly supported by data — is still contingent on assumptions about spatial geometry.

It also highlights the power of our reconstruction method in probing such assumptions in a data-driven way.

1.9. Application of Our Model-Independent Analysis to Buchert Averaging

In addition to exploring the effects of radial inhomogeneity on cosmic dynamics, we apply our model-independent reconstruction to a broader class of inhomogeneous cosmologies using the Buchert averaging formalism. This framework, introduced in Section 1.6.1 and developed in detail in Section 6 of this thesis, provides a systematic way to study the large-scale effects of inhomogeneities on cosmological evolution by averaging scalar quantities over spatial hypersurfaces.

The central idea of this approach is that the dynamics of the averaged universe may differ significantly from those of a homogeneous FLRW model, particularly if local variations in expansion rate, shear, and curvature contribute non-negligibly to the overall evolution. In this context, the backreaction term Q_D in the Buchert equations can act as an effective energy component, potentially leading to accelerated expansion even in the absence of a cosmological constant.

To test this idea, we take our reconstructed expansion history — derived directly from the observational distance data using a flexible set of fits — and reinterpret it as the effective expansion history of an averaged domain $a_D(t)$. From this, we calculate the corresponding kinematic backreaction $Q_D(t)$ and the averaged spatial curvature $\langle R \rangle_D(t)$, using the Buchert equations in reverse: that is, treating our reconstructed Hubble parameter $H_D(z)$ as a known function and solving for the required backreaction and curvature contributions that would yield this expansion.

This allows us to address a specific question: How much of the observed acceleration can be attributed to backreaction effects, rather than to dark energy?

To test this idea, we take our reconstructed expansion history — derived directly from the observational distance data — and reinterpret it as the effective expansion history of an averaged domain, $a_D(t)$, within the Buchert framework. Using the scaling solutions given by [21]: we introduce an effective energy density term, $\Omega_X(z)$, representing the combined contribution of kinematical backreaction and averaged curvature. It evolves as $\Omega_X(z) \propto (1+z)^n$, and we and fit the reconstructed Hubble parameter $H_D(z)$ using the effective Friedmann equation:

$$H_D^2(z) = H_{D_0}^2(\Omega_m(1+z)^3 + \Omega_X(1+z)^n), \tag{1.17}$$

By fitting this expression to the reconstructed expansion history, we infer the range of n and Ω_X values that could account for the observed acceleration in an averaged universe without invoking a cosmological constant. This approach provides a way to quantify how backreaction-like effects would need to behave to match observational data.

Our results show that it is possible to reproduce the reconstructed expansion history with a range of n and Ω_X values. However, whether such backreaction terms can arise from realistic inhomogeneous models remains a separate theoretical question.

1.10. Rewriting the Metric in Supernova-Adapted Coordinates

Beyond reconstructing the expansion history from supernova data, we also explore a reformulation of the FLRW spacetime in a coordinate system that is more naturally aligned with observations. Since Type Ia supernovae provide direct measurements of luminosity distance as a function of redshift, it is advantageous to work in a framework where these observational quantities appear explicitly in the metric.

Starting from the relationship between redshift, luminosity distance, and cosmic time, we perform a change of variables that replaces redshift z with a new time-like coordinate y, defined in terms of the so-called photon-count distance. This coordinate

is constructed directly from observational data and leads to a new parametrization of the spacetime metric in terms of a single function $b(y)$, which we extract by fitting to the transformed supernova data.

The resulting metric retains spherical symmetry and is equivalent to the FLRW form, but written in terms of y and $b(y)$, with the key advantage that all model assumptions are absorbed into a single function that can be directly compared to data. Once $b(y)$ is known, the expansion history — including the scale factor, Hubble parameter, and acceleration — can be expressed analytically in terms of it.

This approach allows us to reconstruct not only the expansion rate but the metric itself, using observational data as the starting point. It also provides a new route to identifying the transition redshift — the point at which the universe's expansion switched from deceleration to acceleration — by analyzing the shape and derivatives of the fitted $b(y)$ function.

1.11. Time-dependent Metric With Steady Physical Content

In this exploratory section, we investigate a curious class of inhomogeneous and anisotropic metrics whose components evolve exponentially with time but whose physical quantities remain entirely time-independent. Despite the strong time dependence of the metric coefficients, all curvature invariants — including the Ricci scalar and the Kretschmann scalar — are time-independent. The trace and mixed-index components of the Einstein tensor are also time-independent, even though the metric itself evolves, resulting in a stress-energy tensor that describes an anisotropic but temporally steady fluid configuration. Spatial slices of the metric are flat, and comoving observers follow geodesics with nonzero but time-independent expansion. We also show that this spacetime violates the Strong Energy Condition (SEC) for all real-valued choices of the warp functions. While we make no claim of novelty for this solution, we were unable to find an existing discussion of it in the literature. It may serve as a useful toy model

for studying SEC-violating matter or field dynamics in curved, but physically static, backgrounds.

2. THE DATA AND THEIR ANALYSIS FOR THE HOMOGENEOUS UNIVERSE

In this chapter, we discuss the cosmological supernova and GRB data that we will be using; and review the method, introduced in previous work and to be used in the following two chapters, of constructing the time-derivatives of the scale factor from these data, assuming the cosmological principle.

2.1. Data Sets

In this work, we primarily utilize the Pantheon+ compilation of Type Ia supernovae [18], which provides luminosity distance measurements for over 1500 supernovae across the redshift range $0.001 < z < 2.26$. Compared to earlier datasets, Pantheon+ offers substantially reduced statistical and systematic uncertainties, allowing for a more precise reconstruction of the expansion history. A plot of the Pantheon+ data is shown in Figure 2.1. When compared to Pantheon data used in previous work ([12], Figure 1 in same format), wider z-range and smaller errors are apparent. To further stabilize the high-redshift behavior of the reconstructed functions, we supplement the supernova sample with a set of Gamma-Ray Burst (GRB) [19] luminosity distance measurements extending up to $z \sim 8$. Although GRB distance indicators are not completely model-independent due to calibration relations, the GRB dataset constitutes only approximately 10 percent of the total number of data points. Their inclusion primarily serves to anchor the high-redshift fits without significantly affecting the results in the low-redshift regime where the supernova data dominate. Additionally this procedure suppresses numerical oscillations in second derivatives.

We note that GRB luminosity distance measurements are not fully model-independent and can vary significantly depending on the calibration method employed. In our previous work [12], the inclusion of a small GRB dataset helped stabilize the reconstruction without materially affecting the inferred transition redshift. However, in this work,

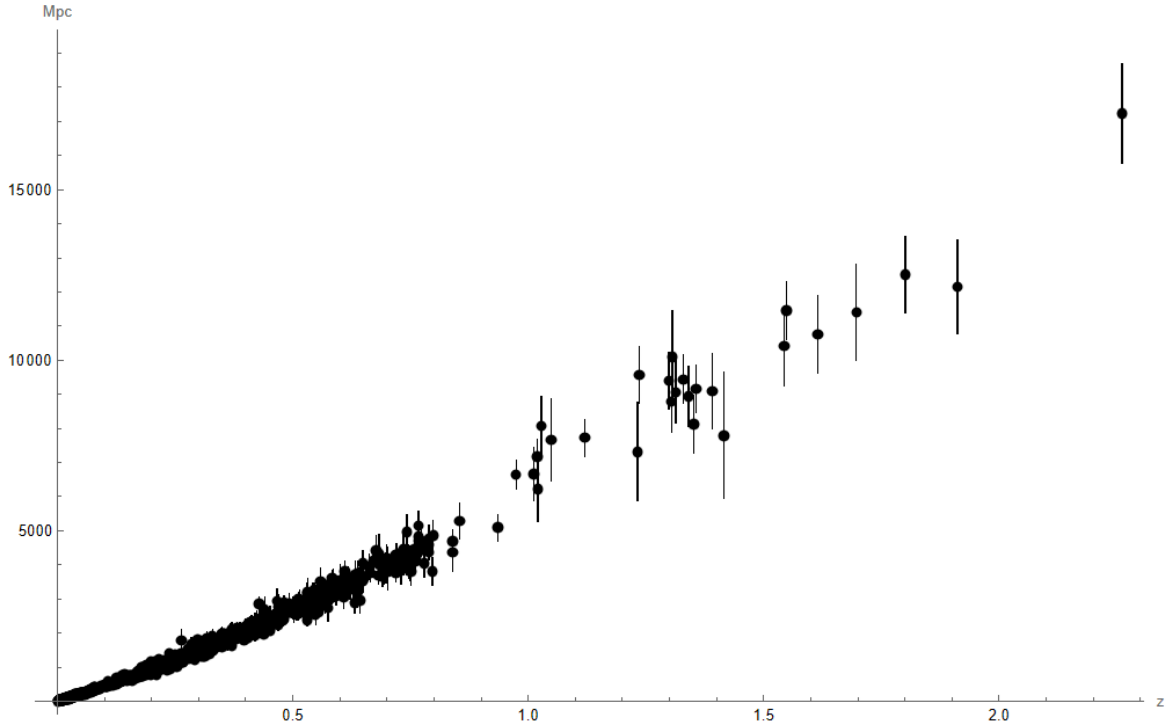


Figure 2.1. Luminosity distance $d_L(z)$ versus redshift for Type Ia supernovae in the Pantheon+ compilation.

we incorporated a more recent GRB dataset [19], which, although still constituting only approximately 10 percent of the total data, resulted in a noticeable shift in the transition redshift when included.

To mitigate this issue, we compared the luminosity distance–redshift slopes of the older [22] and newer [19] GRB datasets. We found that the slope of the older dataset was approximately 1.7 times greater than that of the newer dataset. Since we use GRB data primarily to anchor the high-redshift behavior of the fits rather than to extract direct cosmological conclusions, we chose to rescale the luminosity distances of the newer GRB dataset by a constant factor such that its effective slope matched the average of the two datasets' slopes. This adjustment ensures that the influence of the GRB dataset remains consistent with that of the earlier work, while minimizing potential systematic biases in the reconstructed transition redshift. We verified that after this rescaling, the transition redshift obtained with and without the inclusion of GRB data remained in reasonably good agreement.

The Pantheon+ collaboration provides standardized distance moduli $\mu(z)$ for each supernova, corrected using the Tripp (1998) method [23]. The zero-point calibration, including the fiducial absolute magnitude M, is based on Cepheid-host distances from the SH0ES 2021 analysis [20]. Although the absolute scale of the luminosity distance depends on this calibration, the overall shape of the $d_L(z)$ curve, which governs the reconstruction of the expansion history, is largely unaffected. We adopt the provided $\mu(z)$ values directly and convert them to luminosity distances using the standard relation

$$d_L(z) = 10^{\mu(z)/5-5}\text{Mpc}. \tag{2.1}$$

A combined plot of the Pantheon+ and rescaled GRB data is given in Figure 2.2, illustrating the wider redshift coverage of the GRB data and the relation of the two observational datasets used in our analysis.

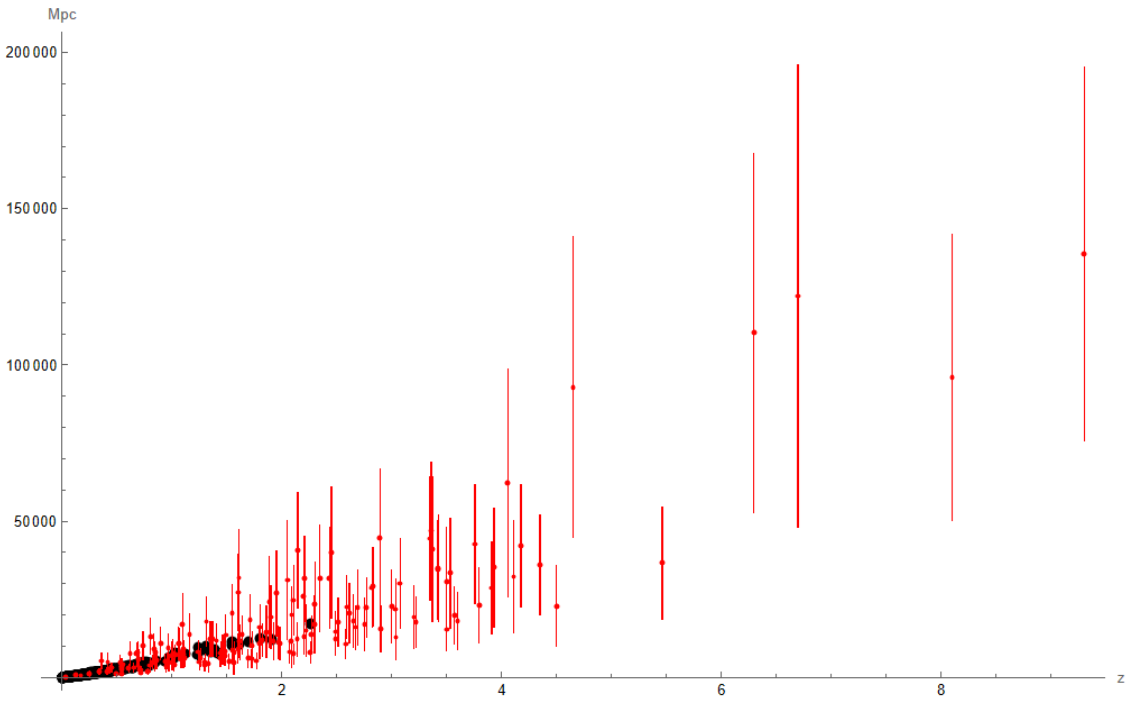


Figure 2.2. Luminosity distance $d_L(z)$ as a function of redshift for the full observational dataset. Black points represent Type Ia supernovae from the Pantheon+ compilation; red points represent the rescaled GRB dataset. The GRBs extend the redshift range beyond the supernova domain.

2.2. Luminosity Distance Fitting Procedure

To reconstruct the expansion history in a model-independent manner, we fit smooth functions to the data (Pantheon+ and GRB). We consider eight distinct families of functions, including polynomials, Padé approximants, and other commonly used basis expansions in cosmography. In addition, we explore six different redshift reparameterizations, defined by variables

$$y_0 = z, \quad y_1 = \frac{z}{z+1}, \quad y_2 = \arctan\frac{z}{z+1}, \tag{2.2}$$

$$y_4 = \arctan z, \quad y_5 = \ln(1+z), \quad y_6 = u = z+1, \tag{2.3}$$

in order to improve convergence properties and capture possible nontrivial redshift behavior.

The eight families we use are shown in Table 2.1. In each family, the best-fitting function is selected based on the Bayesian Information Criterion (BIC). Since we aim for a model-independent reconstruction, our function candidates are designed to be as generic and flexible as possible. We begin with simple polynomials without a constant term [except when using $y_6 = u = z+1$, where we impose the condition $d_m(u=1) = 0$ by adjusting the constant term]. To introduce additional flexibility, we consider modifications of the polynomial family by multiplying them with exponential functions, where the exponent is linear or quadratic in y_i. Further generalizations involve multiplying the original polynomial and exponential-polynomial families by $(1+z)$. Another widely used generalization is the Padé approximant [24–26], defined as

$$\tilde{P}(y, M, N) = \frac{P_M(y_i)}{P_N(y_i) + 1} \tag{2.4}$$

where $P_M(y_i)$ denotes an M^{th} order polynomial without constant term. We also con-

struct a variant by multiplying the Padé approximant by $(z + 1)$, resulting in an additional function family. This range of function forms ensures sufficient generality to capture the essential features of the luminosity distance data without introducing unnecessary bias.

Table 2.1. The 8 different families used in fits. y can be any one of the redshift parameters described previously (y_0 to y_6), $P_N(y)$ is the N^{th} order polynomial with zero constant term (except when using $y_6 = u$), $u(y)$ is $(1 + z)$ expressed in terms of y, $\tilde{P}(y,\, M,\, N)$ is the Padé approximant in variable y and orders M & N; and c & d are constants.

Designation	Function family
F1	$P_N(y)$
F2	$P_N(y)u(y)$
F3	$P_N(y)\exp(cy)$
F4	$P_N(y)u(y)\exp(cy)$
F5	$P_N(y)\exp(cy + dy^2)$
F6	$P_N(y)u(y)\exp(cy + dy^2)$
F7	$\tilde{P}(y,\, M,\, N)$
F8	$u(y)\ \tilde{P}(y,\, M,\, N)$

For each combination of function family and redshift variable, we perform a separate fit to the data, resulting in a total of 48 fitted functions. The number of free parameters in each fit is determined by minimizing the Bayesian Information Criterion (BIC), ensuring an optimal balance between goodness-of-fit and model complexity. This selection method avoids overfitting, especially given the large number of available data points in the Pantheon+ sample. All of the best fits of each family and redshift variable, together with their BIC values are shown in Table 2.2 and illustrated in Figure 2.3. The fit with the lowest BIC for each redshift reparameterization was selected for further analysis. The fitted functions $d_L(z)$ serve as the basis for reconstructing the

cosmic time–redshift relation, the scale factor derivatives, and the Hubble parameter as described in the following subsections.

Table 2.2. The best fits for the Pantheon+ and GRB data. Each cell displays the internal label(s) of the best-fitting member of the row's family for the column's redshift variable, and the fit's BIC value.

family \ variable	$y_0 = z$	y_1	y_2	y_4	y_5	$y_6 = u$
F1	4; 19418.9	4; 19425.6	6; 19431.1	4; 19425.3	3; 19412.4	4; 19418.9
F2	3; 19413.3	3; 19412.6	3; 19412.8	3; 19411.8	3; 19413.7	3; 19413.3
F3	4; 19423.6	2; 19516.5	2; 19690.4	2; 19480.3	4; 19416.8	3;19416.2
F4	2; 19408.8	2; 19405.5	2; 19431.3	2; 19444.4	3; 19413.1	2; 19408.8
F5	4; 19417.4	3; 19416.5	4; 19423.5	4; 19422.7	3; 19412.7	4; 19417.4
F6	3; 19414.4	3; 19412.9	3; 19412.	3; 19411.8	3; 19412.7	3; 19414.4
F7	2;1; 19413.1	2;1; 19416.2	1;2; 19412.6	1;1; 19411.2	2;1; 19414.0	2;1; 19413.1
F8	2;1; 19418.0	2;1; 19413.1	1;1; 19406.0	1;2; 19411.8	1;2; 19412.1	1;2; 19413.5

Among all the fits, the combination of the y_1 redshift parameterization with the Family 4 function form (polynomial multiplied by $(1+z)$ and exponential) yielded the lowest BIC value. This indicates that, within the set of candidate functions considered, the y_1-F4 combination provides the most statistically favored description of the luminosity distance data according to the BIC criterion. Nevertheless, to ensure robustness and to account for possible biases introduced by specific functional choices, we use all fits with acceptable BIC values for further analysis. Our subsequent reconstruction of the expansion history is thus based on the ensemble of selected fits rather than solely on the single best-fit function.

As a demonstration of how the first family of functions—polynomial models—fit the data, Figure 2.4 displays the Pantheon+ dataset in terms of luminosity distance versus standard redshift $z = y_0$. We include polynomial fits with model complexity ranging from $N = 2$ to $N = 10$, where N denotes the number of free parameters in the fit. The figure highlights the best-fitting model within this family ($N = 3$) along with its 1-σ confidence region. For comparison, the theoretical ΛCDM curve is also shown. It is worth noting that the theoretical ΛCDM curve lies within the 1-σconfidence region of

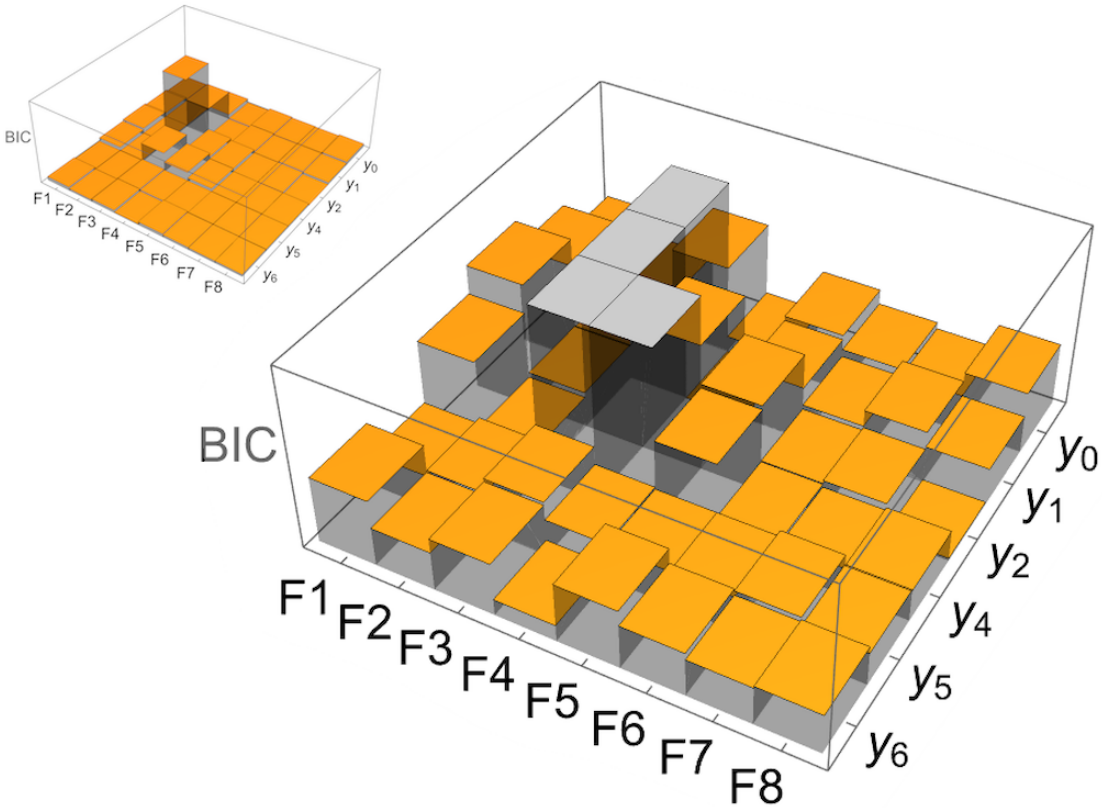


Figure 2.3. BIC values in Table 2.2, illustrated as a 3D bar chart for different function families and redshift variables. The main plot (right) provides a close-up view by truncating the tallest bars for better visibility of the lower values. An inset (left) shows the full-scale chart including all bar heights for completeness.

the best-fitting cubic polynomial ($N = 3$), suggesting that the standard cosmological model is statistically compatible with this model-independent reconstruction of the expansion history. The increasingly erratic behavior observed in the higher-order fits is a typical manifestation of overfitting, in which the model starts to track individual data fluctuations rather than capturing the smooth underlying trend.

In Figure 2.5, we show the best-fitting model from each family of functions considered, all using the standard redshift variable $y_0 = z$. Each curve is plotted alongside the Pantheon+ dataset, enabling a visual comparison of how different functional forms represent the observed luminosity distance data.

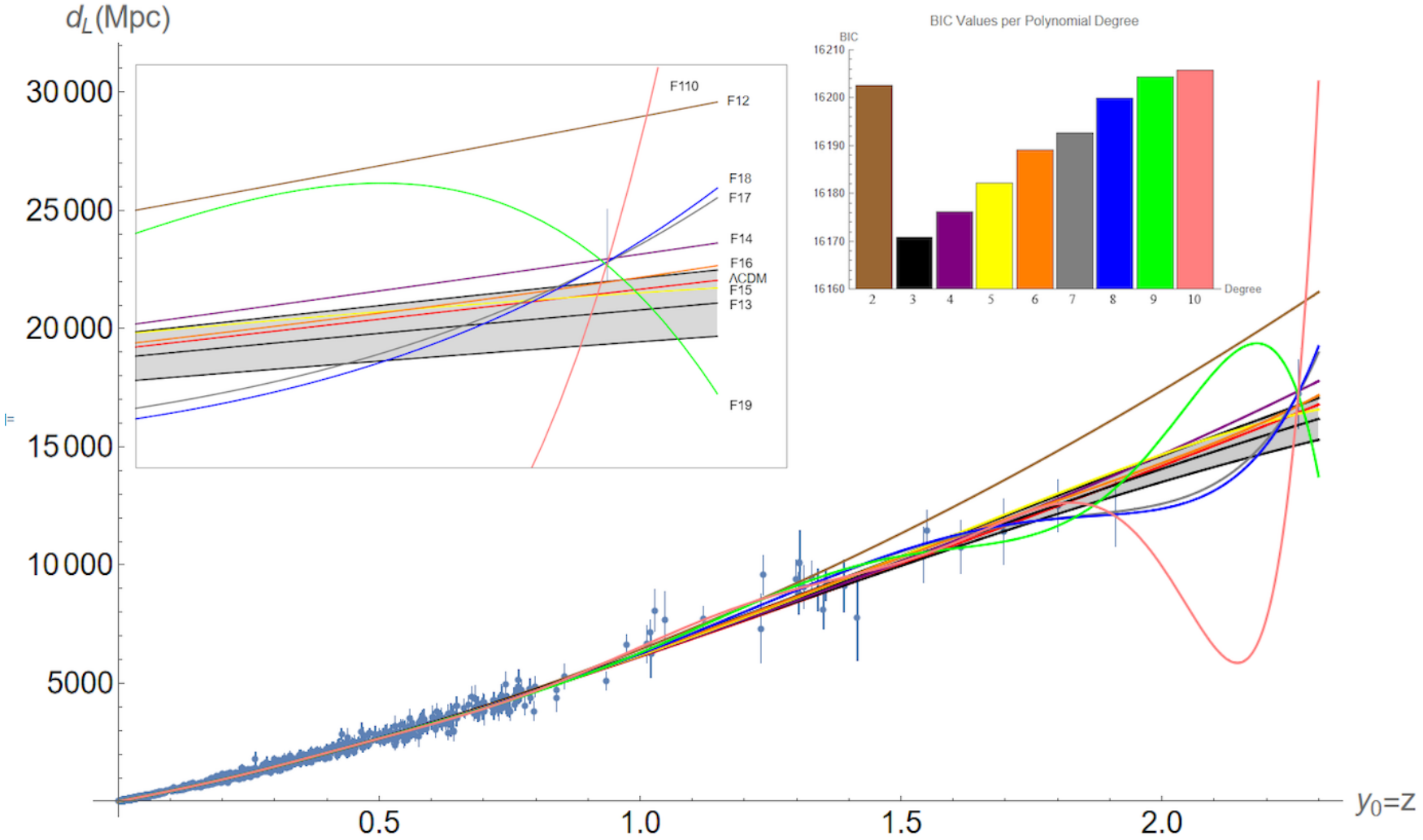


Figure 2.4. Pantheon+ data in terms of luminosity distance and standard redshift, the $N = 2$ to 10 fits for the first family, simple polynomials and ΛCDM model (red), and the 1-σ confidence-level of the best-fitting member ($N = 3$) of the family F1. The insets show (i) a magnified view of the right end of the data, and (ii) a bar chart of the BIC values for the F1 fits ($N = 2$ to 10).

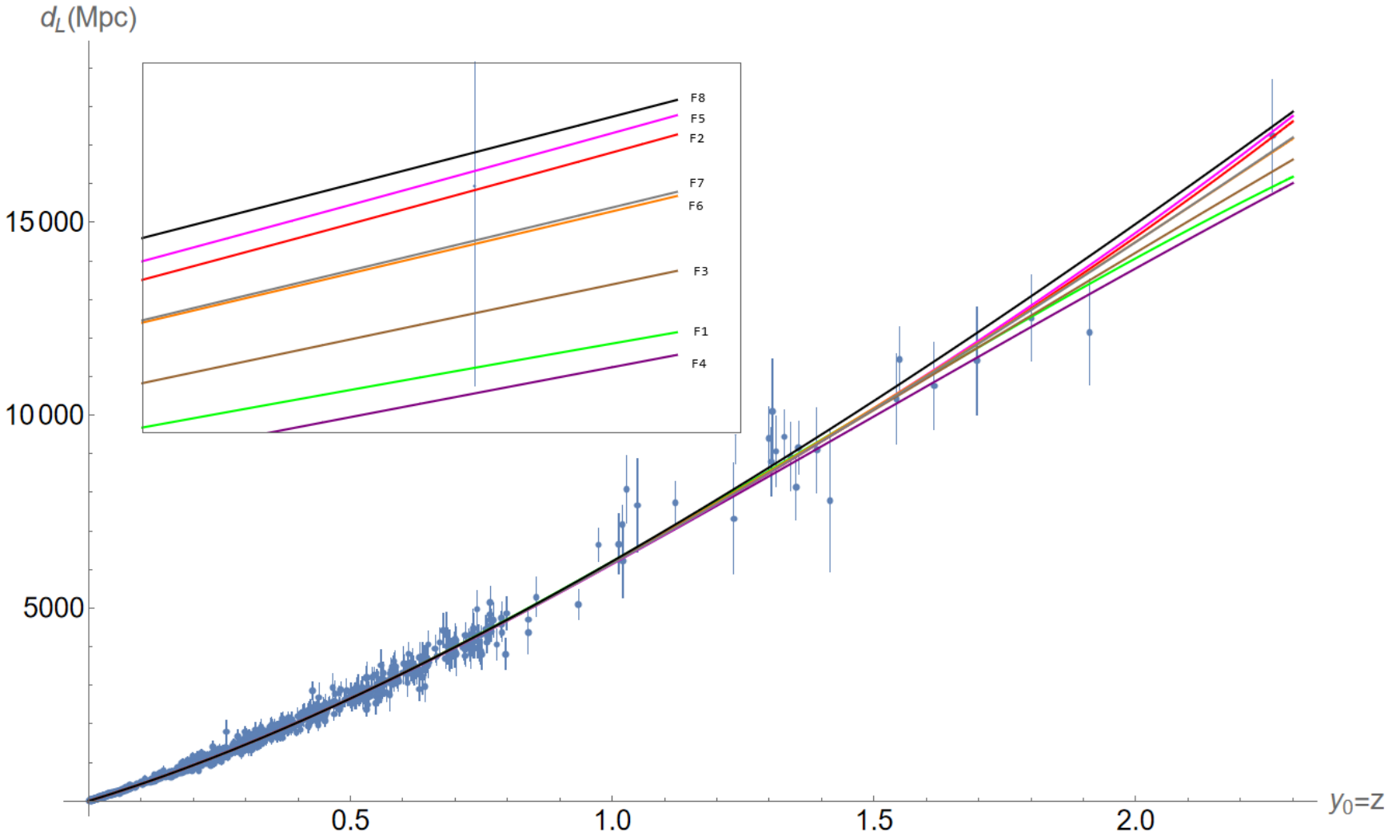


Figure 2.5. Best-fitting curves from each functional family applied to the Pantheon+ dataset, using the standard redshift variable $y_0 = z$. Each curve represents the optimal model (based on BIC) within its respective function class. This comparison illustrates how different model families approximate the observed luminosity distance–redshift relation.

2.3. Reconstruction of the Cosmic Time–Redshift Relation

Having obtained smooth functional fits to the luminosity distance $d_L(z)$, we next reconstruct the relation between cosmic time and redshift, $t(z)$, using the null geodesic condition appropriate for the standard FLRW metric. Using the scale factor-redshift relation and the definition of the luminosity distance

$$a(t) = \frac{a_0}{1+z}, \quad d_L = a_0(1+z)r. \tag{2.5}$$

We can derive the following relation for the differential of cosmic time with respect to redshift;

$$\frac{dt}{dz} = -\frac{1}{c(1+z)} \frac{1}{\sqrt{1-\kappa\frac{d_L^2}{(1+z)^2}}} \frac{d}{dz}\left(\frac{d_L(z)}{1+z}\right). \tag{2.6}$$

Since the expression for $\frac{dt}{dz}$ in Eq. (2.6) contains the spatial curvature parameter k and the current scale factor a_0, we define the combination $\kappa = \frac{k}{a_0^2}$, which has units of inverse length squared. As the supernova data alone do not directly constrain the spatial curvature, κ is treated as free parameter. For practical purposes, we set $a_0 = 10,000$ Mpc, a representative large cosmological distance, and explore 11 equally spaced values of κ in the range $-\kappa_0 \leq \kappa \leq +\kappa_0$, where $\kappa_0 = (10,000 \text{ Mpc})^{-2}$. This allows us to consider flat, open, and closed geometries consistently.

With this parametrization, we can compute $\frac{dt}{dz}$ from each fitted luminosity distance function, and consequently reconstruct the scale factor's firts and second derivatives $\dot{a}(z)$, $\ddot{a}(z)$, the Hubble parameter $H(z)$.

2.4. Calculation of Scale Factor Derivatives and Expansion History

Having reconstructed the cosmic time–redshift relation $dt/dz(z)$ through the fitted luminosity distance functions, we proceed to calculate the derivatives of the scale

factor $a(t)$ with respect to cosmic time. Since the scale factor is related to redshift by

$$a(z) = \frac{a_0}{1+z}, \tag{2.7}$$

we can compute the first derivative $\dot{a}(z)$ via the chain rule:

$$\dot{a}(z) = \frac{da}{dt} = \frac{da}{dz}\left(\frac{dt}{dz}\right)^{-1}. \tag{2.8}$$

Given that

$$\frac{da}{dz} = -\frac{a_0}{(1+z)^2}, \tag{2.9}$$

this yields

$$\dot{a}(z) = -\frac{a_0}{(1+z)^2}\left(\frac{dt}{dz}\right)^{-1}. \tag{2.10}$$

Similarly, the second derivative $\ddot{a}$ can be obtained by differentiating $\dot{a}(z)$ with respect to z and applying the chain rule:

$$\ddot{a}(z) = \left(\frac{dt}{dz}\right)^{-1}\left(\frac{2a_0}{(1+z)^3}\left(\frac{dt}{dz}\right)^{-1} + \frac{\partial}{\partial z}\left(\frac{dt}{dz}\right)\frac{a_0}{(1+z)^2}\left(\frac{dt}{dz}\right)^{-2}\right). \tag{2.11}$$

Finally, the Hubble parameter $H(z)$ is given by

$$H(z) = \frac{\dot{a}(z)}{a(z)} = -\frac{1}{1+z}\left(\frac{dt}{dz}\right)^{-1}. \tag{2.12}$$

We believe the idea of fitting a function to the observed data, the $d_L - z$ pairs, and derive $\dot{a}(z)$, $\ddot{a}(z)$, and hence some other cosmological functions of interest analytically from the original $d_L(z)$ fit, is different enough to merit its own name. We suggest "luminosity-distance-fitting (LDF) procedure". In our works we used a range of tem-

plate functions and independent variables for the same relation, a "spread-LDF", so we worked with a range of implicit models, making our works model-independent by averaging over the space of possible models, or at least part of it.

For each reconstructed function, uncertainties can be propagated from the fitted parameters by standard linear error propagation. Specifically, the variance of a derived quantity $A(z)$, (where $A(z)$ is any reconstructed function), depending on fit parameters $\{a_i\}$ is computed as

$$\sigma_A^2(z) = \Sigma_i \left(\frac{\partial A}{\partial a_i}\right)^2 + 2\Sigma_{i<j} \left(\frac{\partial A}{\partial a_i}\right)\left(\frac{\partial A}{\partial a_j}\right) \mathrm{Cov(a_i, a_j)}, \tag{2.13}$$

where $\sigma_{a_i}^2$ and $\mathrm{Cov}(a_i, a_j)$ are the variances and covariances of the fitted parameters provided by the fitting procedure. We can then construct 1-σ confidence bands around the reconstructed quantities by plotting $A(z) \pm \sigma_A(z)$.

3. MODEL-INDEPENDENT RESULTS FOR THE HOMOGENEOUS UNIVERSE

In this chapter, we present and discuss the results of the data and the procedure (spread-LDF) discussed in Chapter 2. This constitutes an update of the relevant part of our previous work, needed due to availibility of newer data.

3.1. Reconstruction of the Acceleration Functions

Using the methodology spread-LDF described in Section 2, we reconstructed the second derivative of the scale factor $\ddot{a}$ for each of the 48 fitted luminosity distance functions. Each reconstruction is obtained by differentiating the fitted $d_L(z)$ function as detailed in Section 2.4 and applying the chain rule relations connecting redshift, cosmic time, and the scale factor.

To illustrate the influence of high-redshift data on the reconstruction, we first present the set of $\ddot{a}$ functions reconstructed without including Gamma-Ray Burst (GRB) data. Figure 3.1 displays all 48 reconstructed acceleration functions over the redshift range $0 < z < 1.5$. Each panel corresponds to a different combination of fitting family and redshift reparameterization. As seen in Figure 3.1, some of the reconstructed acceleration functions exhibit significant oscillatory behavior. These oscillations are primarily artifacts arising from noise amplification during second-order differentiation and do not reflect physically meaningful features.

Next, in Figure 3.2, we show the corresponding reconstructions when the GRB dataset, rescaled as described in Section 2.1, is included along with the Pantheon+ data. The inclusion of the GRBs serves to anchor the high-redshift behavior of the fits, thereby significantly suppressing the oscillations in $\ddot{a}(z)$ without introducing spurious features at lower redshifts. Comparison of Figures [3.1] and [3.2] demonstrates that the GRB data primarily act to stabilize the high-redshift reconstructions while leaving

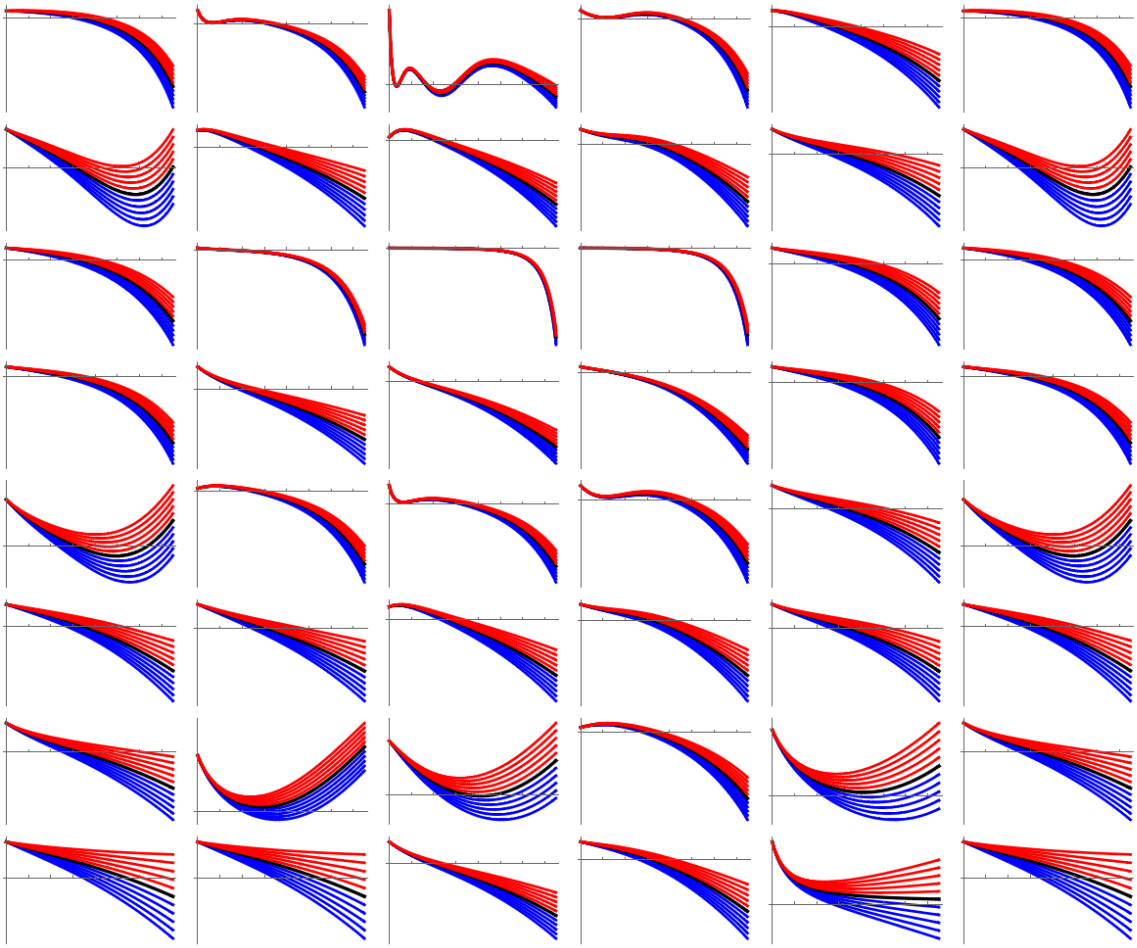


Figure 3.1. The $\ddot{a}$ functions, computed analytically for the Pantheon+ data using Eq. (2.11). The columns represents y_0 to y_6 and rows are for families F1 to F8. Blue, black and red curves are for open, flat and closed spaces respectively. All horizontal axes converted to $y_0 = z$, with the redshift range spanning $0 \leq z \leq 1.5$.

the low-redshift behavior, which is most critical for determining the transition from deceleration to acceleration, largely unchanged.

In the following subsection, we apply selection criteria to identify physically acceptable reconstructions for further analysis.

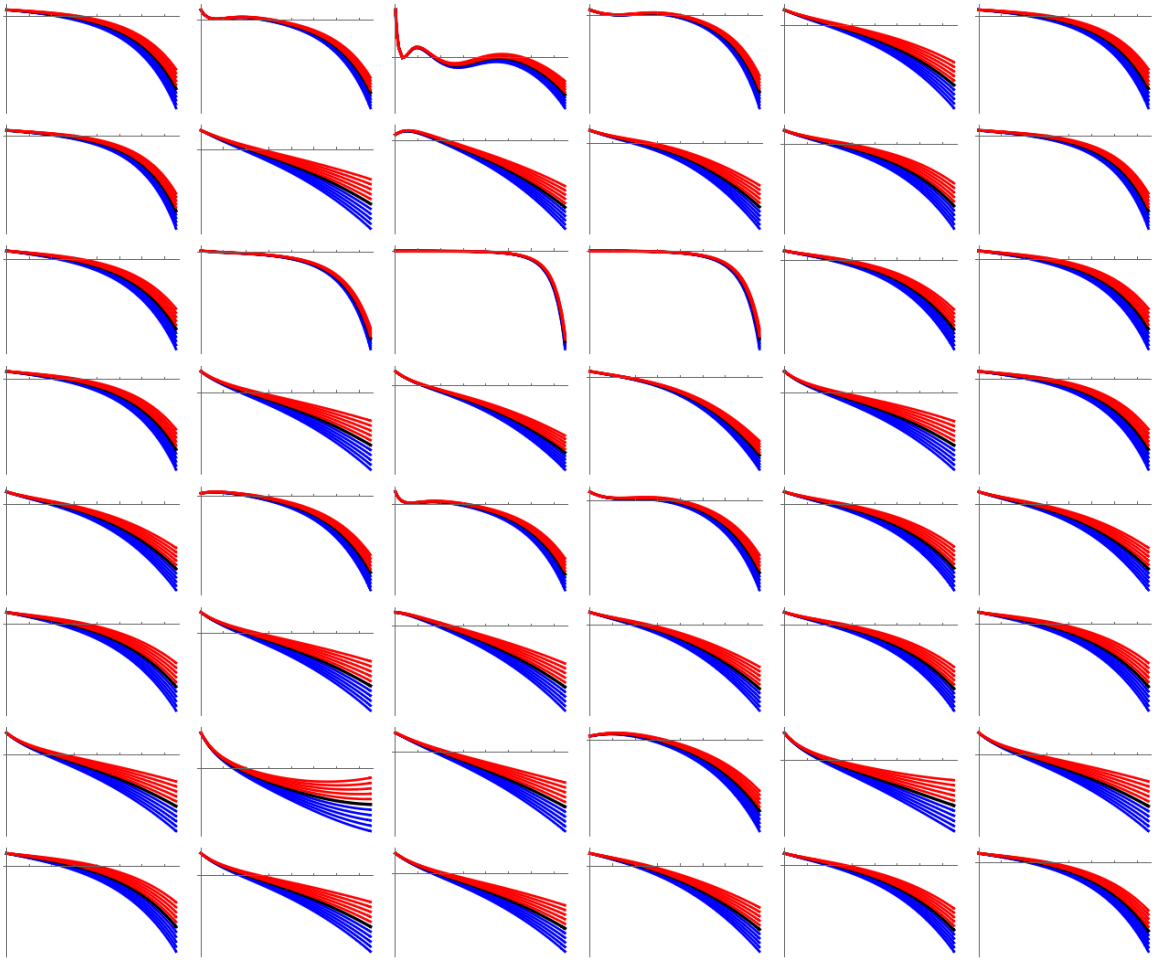


Figure 3.2. The $\ddot{a}$ functions, computed analytically for the Pantheon+ and GRB data using Eq. (2.11). The columns represents y_0 to y_6 and rows are for families F1 to F8. Blue, black and red curves are for open, flat and closed spaces respectively. All horizontal axes converted to $y_0 = z$, with the redshift range spanning $0 \leq z \leq 1.5$.

3.2. Selection of Physically Acceptable Reconstructions

As evident from the reconstructed acceleration functions shown in Section 3.1, not all fits yield physically plausible behavior. In particular, some of the functions exhibit significant oscillations, including features such as multiple transitions between acceleration and deceleration. These are unphysical, since they are not consistent across any subset of the 48 functions, even a small subset.

To systematically select acceptable reconstructions, we applied an elimination procedure based on the grid layout of the 48 functions. Specifically, we examined the reconstructed $\ddot{a}(z)$ curves organized by fitting family (rows) and redshift reparameterization (columns). Entire rows or columns where oscillatory or unphysical behavior was dominant in one figure were eliminated from consideration. This conservative approach ensures that the selection criteria are applied uniformly across all function families and parameterizations, minimizing subjective bias.

In particular, we eliminated:

- Rows 1 and 5, corresponding to F1 and F5 (from table 2.1),
- Columns 3 and 4, corresponding to $y_2 = \arctan\frac{z}{1+z}$, $y_4 = \arctan z$

Although some acceptable individual fits existed within these rows and columns, the majority showed problematic behavior, motivating the removal of the entire group for consistency.

After this selection, we retained 24 reconstructions, which are sufficiently smooth and exhibit a single, physically reasonable transition from deceleration to acceleration. These selected functions form the basis for our subsequent analysis of the cosmic acceleration history.

3.3. Reconstructed Expansion: Acceleration and Hubble Parameter

After selecting the 24 physically acceptable reconstructed acceleration functions, we proceeded to compute an averaged acceleration curve. The average $\ddot{a}_{\text{avg}}(z)$ was constructed by simply taking the arithmetic mean of the 24 individual $\ddot{a}(z)$ functions at each redshift point. Each of the 24 selected $\ddot{a}(z)$ reconstructions contains 11 curves corresponding to different values of the curvature parameter $\kappa \, \epsilon \, [-\kappa_0, +\kappa_0]$. Consequently, the averaged $\ddot{a}_{\text{avg}}(z)$ also yields 11 curves, one for each κ.

To estimate the uncertainty associated with the averaged curve, we selected a representative function among the 24 fits. Given the similarity in fitting behavior among the selected functions, this approximation provides a reasonable estimate of the uncertainty without significantly affecting the derived transition redshift. The representative fit was chosen as the one minimizing the integrated absolute difference with respect to the averaged curve over the redshift range $0 < z < 1.5$, that is, minimizing

$$\Delta = \int_0^{1.5} |\ddot{a}_{\rm fit}(z) - \ddot{a}_{\rm avg}(z)|\, dz. \tag{3.1}$$

This selection ensures that the chosen representative closely matches the behavior of the average and is thus appropriate for estimating the 1-σ confidence band. With this method, fit y5-F3 becomes the representative fit.

The uncertainty on $\ddot{a}(z)$ was propagated from the fit parameters of the representative function using standard linear error propagation (see Section 2.4), including covariance terms. The resulting $\sigma_{\ddot{a}}(z)$ was used to construct the 1-σ confidence region around the averaged curve.

In Figure 3.3, we present the averaged $\ddot{a}(z)$ curve together with the closest acceleration reconstructed from y5-F3. It is evident that at $z = 0$, all selected acceleration functions, as well as the averaged curve, yield $\ddot{a}(0) > 0$, confirming the current accelerated expansion of the universe. To estimate the uncertainty on this average, we used the representative function (y5–F3), identified by its minimal integrated deviation from the average curve. To avoid visual clutter, we present the 1-σ confidence band only for the $\kappa = 0$ (flat) case, shown in Figure 3.4. This curve provides a clear visual of the reconstructed acceleration history and the corresponding transition redshift for the flat geometry.

For completeness, we also extract the transition redshift z_T for the extreme curvature values $\kappa = \pm\kappa$. The results are summarized in table below, showing that while

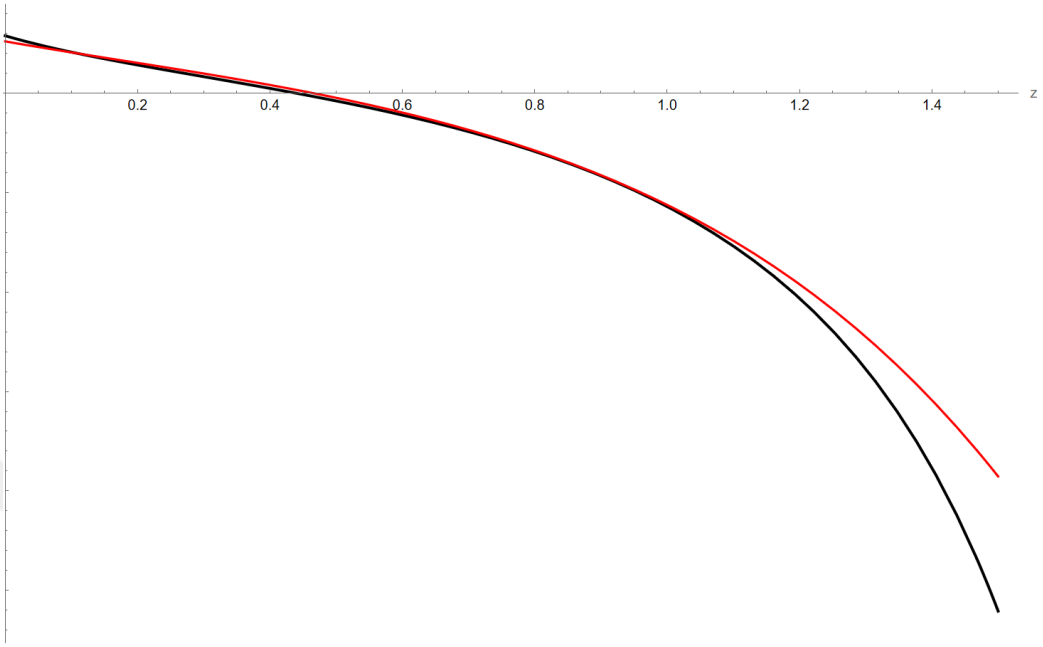


Figure 3.3. Reconstructed average acceleration $\ddot{a}(z)$, shown for the flat curvature case ($\kappa = 0$). The red curve represents acceleration reconstructed from y5-F3.

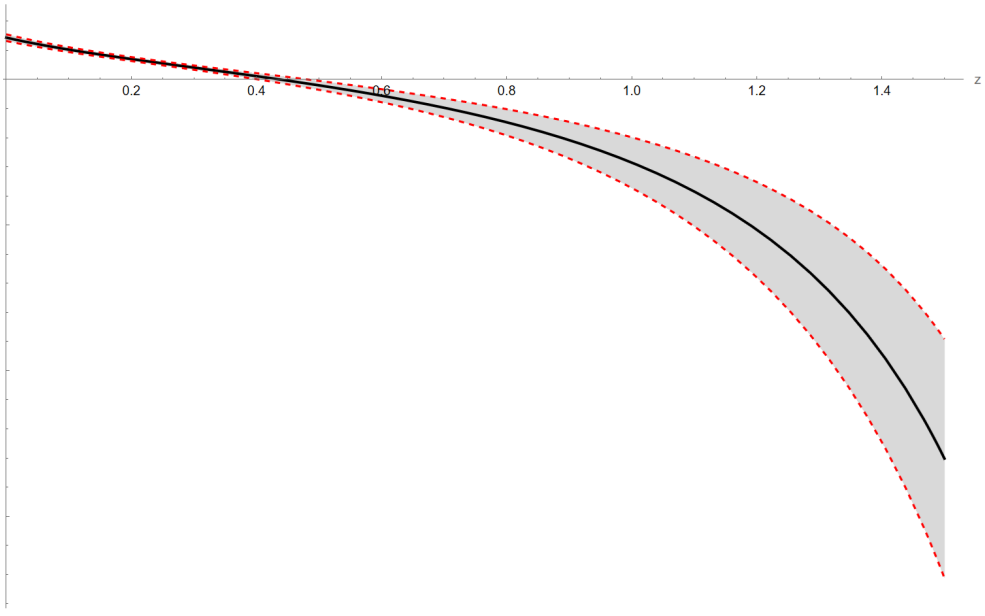


Figure 3.4. Reconstructed average acceleration $\ddot{a}(z)$ with 1-σ confidence band, shown for the flat curvature case ($\kappa = 0$). The shaded region reflects propagated uncertainty from the representative fit (y5-F3). The transition redshift z_T is indicated by the zero crossing.

spatial curvature slightly shifts the value of z_T, the overall conclusion of a transition from deceleration to acceleration remains robust.

Curvature κ	$z_T \pm \delta z_T$
-κ_0	$0.37^{+0.03}_{-0.03}$
0	$0.44^{+0.04}_{-0.03}$
+κ_0	$0.53^{+0.08}_{-0.05}$

Using the average of the reconstructed $\dot{a}(z)$ functions, we compute the Hubble parameter via Eq. (2.12) and show the resulting 11 $H(z)$ curves corresponding to the 11 values of the curvature parameter κ in Figure 3.5. The flat case ($\kappa = 0$) yields a present-day Hubble constant of

$$H_0 = H(z = 0) \approx 73.23 \pm 0.24 \text{ km/s/Mpc}, \tag{3.2}$$

which is in agreement with our ΛCDM fits in Section 4.2 and with local measurements from SH0ES [20]. The increasing trend of $H(z)$ with redshift is consistent with expectations from standard cosmological models, where the expansion rate was higher in the past due to matter domination. The spread among the curves for different κ values illustrates the degeneracy between spatial curvature and the expansion history, where different values of κ can lead to similarly shaped $H(z)$ curves, particularly at low redshifts.

Our reconstructed value of $H_0 = 73.23 \pm 0.24$ is consistent with the SH0ES calibration adopted in the Pantheon+ distance moduli. However, the quoted error does not reflect full cosmological uncertainty, as it omits correlated systematics. Therefore, this result should not be interpreted as an independent constraint on H_0, but rather as a consistency check within a SH0ES-calibrated framework.

Since the Pantheon+ distance moduli are calibrated using a fiducial absolute magnitude M derived from SH0ES 2021 Cepheid host distances, our reconstructed $H(z)$

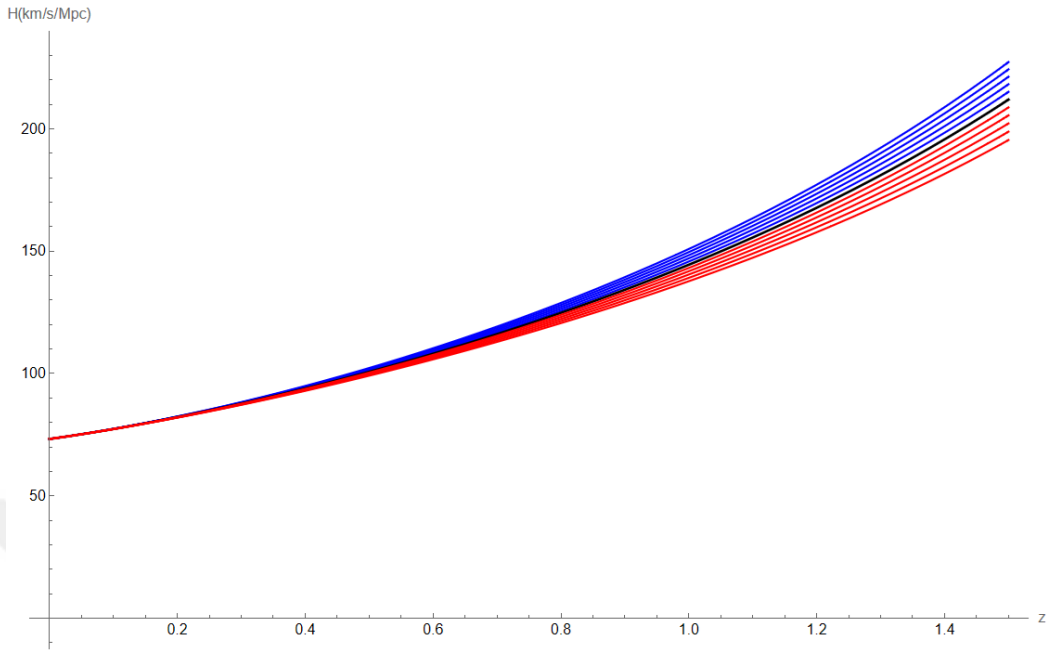


Figure 3.5. Reconstructed Hubble parameter $H(z)$ obtained from the average of 24 accepted $\dot{a}(z)$ functions. The 11 curves correspond to different values of the curvature parameter κ, with the flat case ($\kappa = 0$) shown in black, open models ($\kappa < 0$) in blue, and closed models ($\kappa > 0$) in red. The present-day value for the flat case is $H_0 \approx 73.2$ km/s/Mpc.

inherits this normalization. Consequently, the absolute value of H_0 should be interpreted in the context of this calibration, though the shape of $H(z)$ remains meaningful for probing the expansion history.

As an additional consistency check, we compare our reconstructed $H(z)$ to direct Hubble parameter measurements from cosmic chronometers [27]. As shown in Figure 3.6, our model-independent curves remain within the 1-σ range of the observational data across $0 < z < 1.5$, demonstrating good agreement and further validating the reliability of the reconstruction.

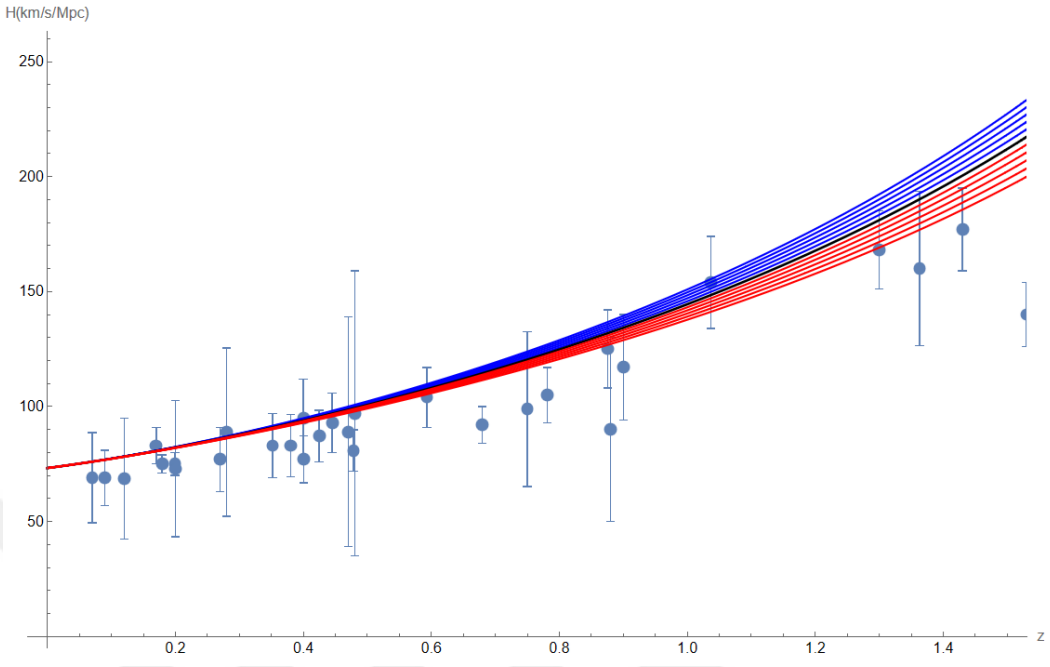


Figure 3.6. Comparison between the reconstructed Hubble parameter $H(z)$ (shown as families of red and blue curves for different curvature values κ) and observational data from cosmic chronometers [27]. The red curves correspond to positive κ, and the blue curves to negative κ.

4. SEMI-MODEL-INDEPENDENT ANALYSIS FOR THE HOMOGENEOUS UNIVERSE: DARK ENERGY AND ΛCDM CONSISTENCY

Having completed our model-independent reconstruction of the expansion history in Chapter 3, we now transition to a semi-model-independent analysis; that is, we assume a gravity model (GR) but no matter/energy model. So, we use the Einstein field equations to interpret the reconstructed quantities in terms of stress-energy-momentum tensor components. This step allows us to compare the reconstructed expansion history with standard cosmological models such as ΛCDM, and evaluate the inferred matter and dark energy content; still with the underlying assumptions about geometry, which ultimately follow from the cosmological principle.

In several parts of this section, we treat reconstructed functions such as $H(z)$, $\rho(z)$, and $w(z)$ as effective datasets in order to fit model-dependent expressions. These functions are evaluated at discrete redshift intervals, and their uncertainties are estimated using the 1-σ error propagation from the representative fit y5–F3. This approach avoids the prohibitively complex task of propagating the full set of uncertainties from all 24 accepted fits, each of which involves several parameters. While the y5–F3-derived uncertainty band provides a reasonable approximation—as validated in Section 3.3—we note that this method neglects correlations between adjacent redshift points that naturally arise from shared functional dependencies. As such, the resulting fits should be interpreted as indicative rather than precision estimates.

4.1. Interpreting the Reconstructed Expansion: Energy Density

Having reconstructed the expansion history in a model-independent manner, we now interpret it within the framework of General Relativity by applying the first Friedmann equation. From the previously obtained $\dot{a}(z)$, the total energy density $\rho(z)$ can

be computed as

$$\rho(z) = \frac{3c^2}{8\pi G}\left(H^2(z) + \kappa c^2(1+z)^2\right) \tag{4.1}$$

where $\kappa = k/a_0^2$ is the spatial curvature parameter, and we take $a(z) = a_0/(1+z)$. We evaluate this expression for the 11 values of κ used in our reconstruction, including the flat case $\kappa = 0$ as well as positive and negative curvature values. The resulting energy density functions are shown in Figure 4.1, illustrating how curvature influences the inferred total energy density across redshift.

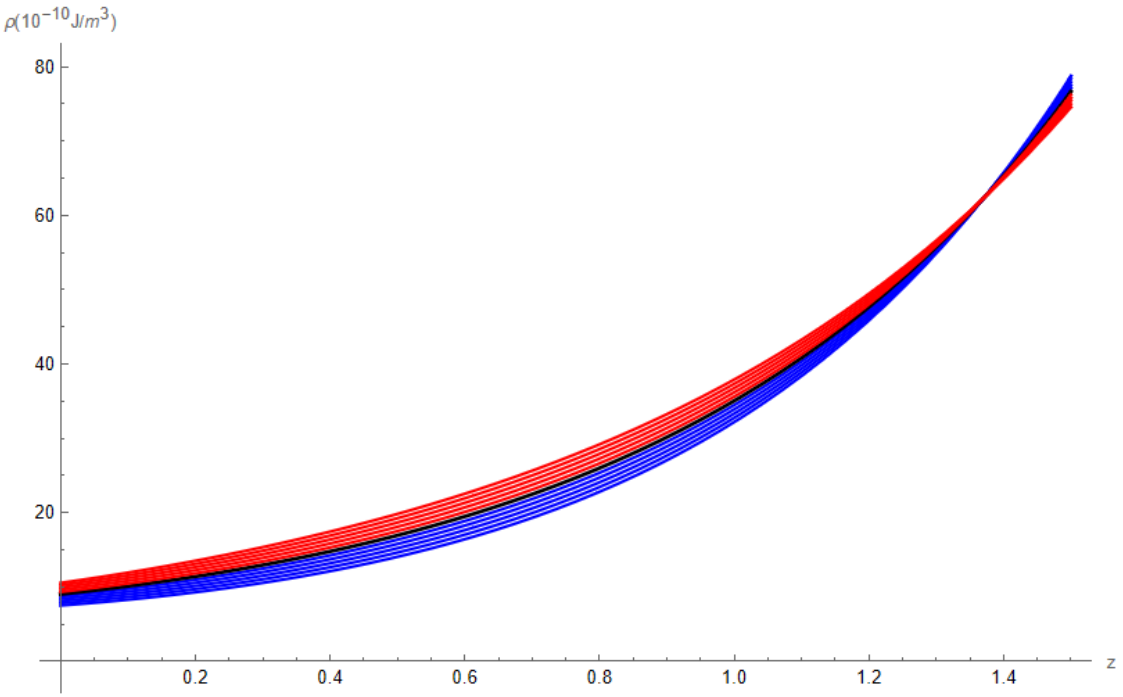


Figure 4.1. Reconstructed total energy density $\rho(z)$ for 11 values of the curvature parameter κ, computed using the representative fit (y5–F3). Black curve corresponds to the flat case $\kappa = 0$; red and blue represent positive and negative curvature, respectively.

Focusing on the flat case, we also compute the 1-σ confidence band for $\rho(z)$ by propagating the uncertainty from the representative fit function y5-F3 (see Section 3.3). This yields three curves: $\rho(z)$, $\rho(z)+\sigma_\rho(z)$, and $\rho(z)-\sigma_\rho(z)$ shown in Figure 4.2.

For each of these, we also plot a matter-only energy density curve of the form

$$\rho_m(z) = \rho_{m,0}(1+z)^3, \tag{4.2}$$

where $\rho_{m,0}$ is scaled such that matches the corresponding ρ_m curve at a reference redshift $z \approx 1$. This ensures the comparison isolates any excess energy density emerging at low redshift.

As shown in Figure 4.2, the reconstructed $\rho(z)$ curves flatten at low redshift and lie significantly above the matter-only evolution. The difference between these curves at $z = 0$ can be interpreted as a lower limit on the non-matter component—consistent with dark energy. Furthermore, the highest scaled $(1+z)^3$ curve that remains below the reconstructed $\rho(z)$ defines an effective upper bound on the present-day matter density Ω_m, which can be accommodated by the expansion history derived from observations.

At redshift $z = 0$, we find the reconstructed total energy density to be

$$\rho(0) = 9.04 \pm 0.06 \text{ in units of } 10^{-10}\text{Joule/m}^3. \tag{4.3}$$

The corresponding scaled matter-only curve yields

$$\rho_m(0) = 4.35 \pm 0.23 \text{ in units of } 10^{-10}\text{Joule/m}^3 \tag{4.4}$$

where the uncertainty arises from the 1-σ bounds on the reconstructed $\rho(z)$ curves. This leads to a clear excess of energy density at low redshift:

$$\rho_{\text{DE,min}}(0) = \rho(0) - \rho_m(0) = 4.69 \pm 0.24 \text{ in units of } 10^{-10}\text{Joule/m}^3 \tag{4.5}$$

which can be interpreted as a lower bound on the dark energy density under the assumption of flat geometry and General Relativity. These values correspond to the

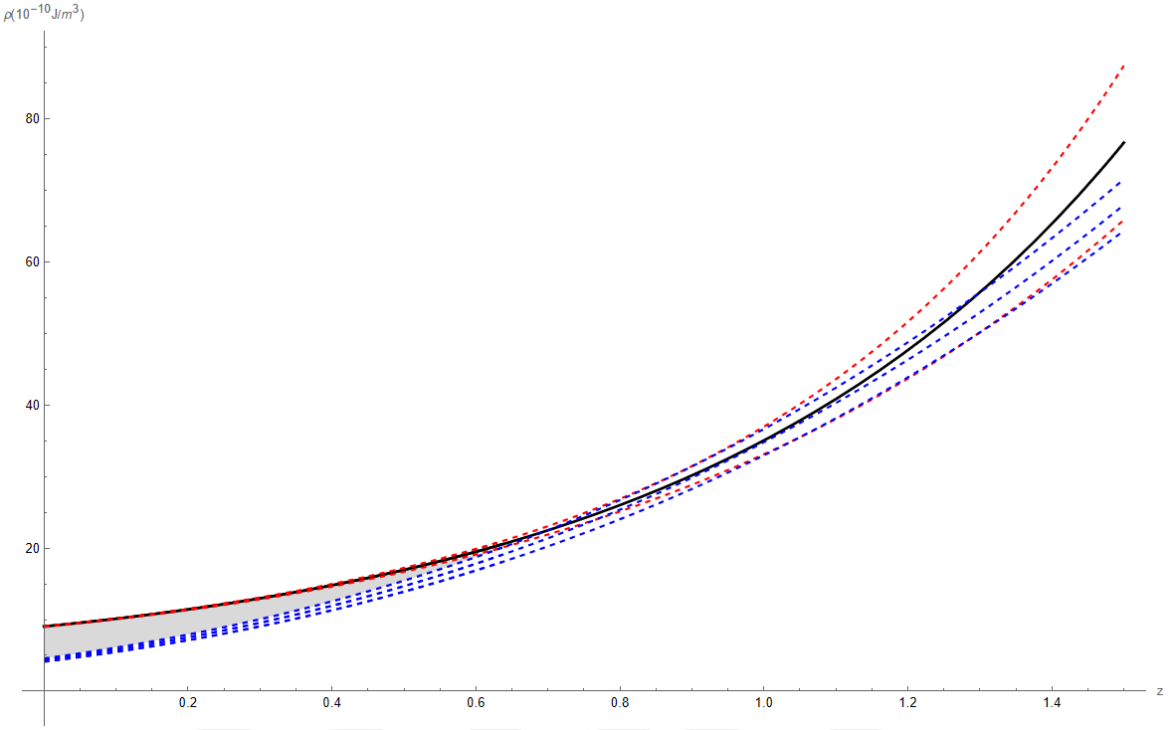


Figure 4.2. Flat curvature case: total energy density $\rho(z)$(black), with 1-σ upper and lower bounds (dashed-red curves) propagated from the representative fit. Each is compared with a scaled matter-only evolution $\rho_m(z) = \rho_{m,0}(1+z)^3$ (dashed-blue curves), matched at $z \approx 1$. The shaded region between $\rho(z)$ and the matter curve at low redshift highlights the minimum extra energy density required beyond matter.

following fractional density parameters:

$$\Omega_m < \frac{\rho_m(0)}{\rho(0)} = 0.481^{+0.029}_{-0.028}, \quad \Omega_\Lambda > \frac{\rho_\Lambda(0)}{\rho(0)} = 0.519^{+0.028}_{-0.029}. \tag{4.6}$$

These values reinforce the conclusion that, even without any assumptions on the contents of the universe (beyond the default existence of matter/dust to some unspecified extent), the expansion history implied by the data requires a non-matter component to explain the observed acceleration — which can be called dark energy. Recall that the conclusion is reached under the assumption that General Relativity remains valid on cosmological scales.

4.2. ΛCDM Fit to Combined Distance Data and Reconstructed $H(z)$

To compare our model-independent reconstruction with standard cosmology, we fit a flat ΛCDM model to the combined Pantheon+ and GRB luminosity distance dataset; and then we fit a flat ΛCDM Hubble function to our reconstructed $H(z)$, again for $\kappa = 0$.

The ΛCDM prediction for the luminosity distance is

$$d_L(z) = (1+z)\frac{c}{H_0}\int_0^z \frac{dz'}{\sqrt{\Omega_m(1+z')^3 + (1-\Omega_m)}}, \tag{4.7}$$

which we fit numerically. Fixing $H_0 = 70$ km/s/Mpc yields a best-fit value of $\Omega_m = 0.56$, which is higher than typical ΛCDM values. However, allowing H_0 to vary freely leads to a significantly improved fit, yielding:

$$\Omega_m = 0.37, \quad H_0 \approx 73 \text{ km/s/Mpc} \tag{4.8}$$

which is fully consistent with our reconstructed Hubble function (Section 3.3), as well as SH0ES [20] estimates.

The theoretical ΛCDM prediction for $H(z)$ is given by:

$$H(z) = H_0\sqrt{\Omega_m(1+z)^3 + (1-\Omega_m)}, \tag{4.9}$$

where H_0 is the Hubble constant and Ω_m is the present-day matter density parameter. We perform this fit using the reconstructed $H(z)$ derived from the average of the 24 accepted $\dot{a}(z)$ functions described in Section 3.3.

Propagating uncertainties from all 24 fits directly is impractical due to the large number of parameters involved. Instead, we adopt the $\sigma_H(z)$ error band from the representative function (y5-F3) as a proxy for the uncertainty in the average curve.

This approximation is justified by the close agreement between the y5-F3 curve and the overall average, as established earlier.

Using these uncertainties in a weighted least-squares fit, we find:

$$\Omega_m \approx 0.39, \quad H_0 \approx 72.8 \text{ km/s/Mpc}, \tag{4.10}$$

which are consistent with local distance ladder measurements of H_0 (e.g., SH0ES) and within reasonable range for ΛCDM expectations, though the matter density is slightly elevated compared to Planck's [5] value of $\Omega_m \approx 0.31$. The resulting ΛCDM curve is shown in Figure 4.3, overlaid on the reconstructed $H(z)$ with 1-σ confidence bands. However, the sensitivity of parameter inference to the reconstruction method, weighting scheme, and dataset (e.g., GRB calibration) highlights the value of model-independent cross-checks like ours.

These best-fit values are in close agreement with those obtained earlier in this section by fitting the ΛCDM luminosity distance expression directly to the combined Pantheon+ and GRB data. Although the two approaches — one model-dependent, the other model-independent — are conceptually distinct, they yield consistent estimates of H_0 and Ω_m within the redshift range where observational constraints are strongest. This consistency supports the reliability of our reconstruction framework and suggests that the standard ΛCDM model remains broadly compatible with the reconstructed expansion history, at least up to $z < 1$.

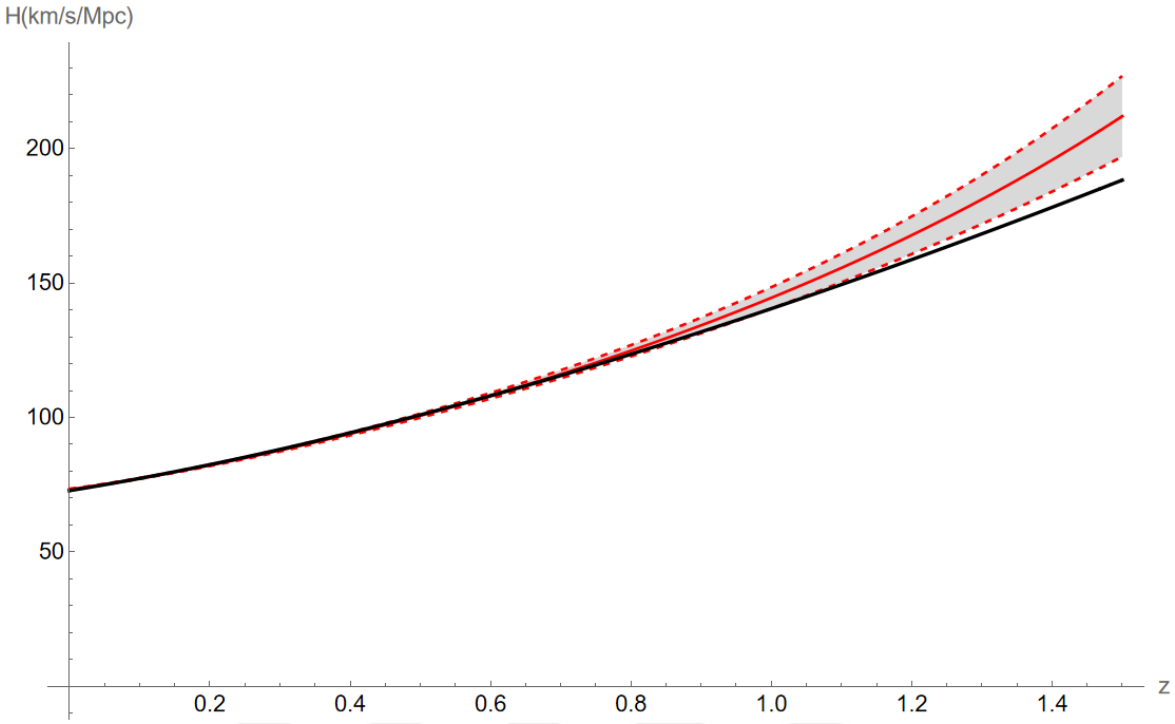


Figure 4.3. Reconstructed Hubble parameter $H(z)$ from the average of 24 accepted $\dot{a}(z)$ curves (with $\kappa = 0$), shown with a 1-σ error band derived from the representative y5-F3 function. The solid black curve shows the best-fit flat ΛCDM model, yielding $H_0 \approx 72.8$ km/s/Mpc, $\Omega_m \approx 0.39$.

4.3. Effective Equation of State from Reconstructed Dynamics

In addition to reconstructing the total energy density $\rho(z)$, we now derive the effective pressure $p(z)$ using the second Friedmann equation:

$$p(z) = \frac{c^2}{8\pi G}\left(-\kappa c^2(1+z)^2 - H(z)^2 - 2\frac{\ddot{a}(z)}{a_0}(1+z)\right). \tag{4.11}$$

This expression allows us to compute the pressure evolution of the cosmic fluid under the assumption of spatial homogeneity and General Relativity. Using the representative reconstruction (y5-F3), we evaluate both $\ddot{a}$ and $\rho(z)$ for the flat curvature case $\kappa = 0$,

and compute the effective equation of state parameter:

$$w(z) = \frac{p(z)}{\rho(z)}. \tag{4.12}$$

This function describes the total dynamical behavior of the universe's energy content as a function of redshift, without assuming any particular decomposition into matter and dark energy components.

In Figure 4.4 , we plot the reconstructed $w(z)$ over the redshift range $0 < z < 1.5$. At redshift $z = 0$, we find

$$w(0) = -0.640^{0.025}_{0.025} \quad (\text{for } \kappa = 0) \tag{4.13}$$

indicating that the effective cosmic fluid behaves as a mixture of pressureless matter and a dark energy–like component with negative pressure. The value lies between the matter-like value $w = 0$ and the cosmological constant value $w = -1$, consistent with a transitioning universe.

The shape of $w(z)$ provides an additional diagnostic of the expansion dynamics. In principle, significant deviations from $w = -1$ at low redshift could hint at a time-varying dark energy or modifications to the gravitational sector, though in our case the reconstruction is still consistent with a $w(z)$ smoothly interpolating between matter and Λ-dominated epochs.

4.3.1. Linearity of the Reconstructed $w(z)$

Upon inspecting the reconstructed effective equation of state function $w(z) = p(z)/\rho(z)$, we observe that it exhibits a remarkably linear behavior over the redshift interval $0 < z < 1.5$. To quantify this observation, we perform a quadratic fit to the reconstructed $w(z)$ in this interval. For this purpose, we construct synthetic $w(z)$ data by sampling equally spaced redshift points and assigning uncertainties based on

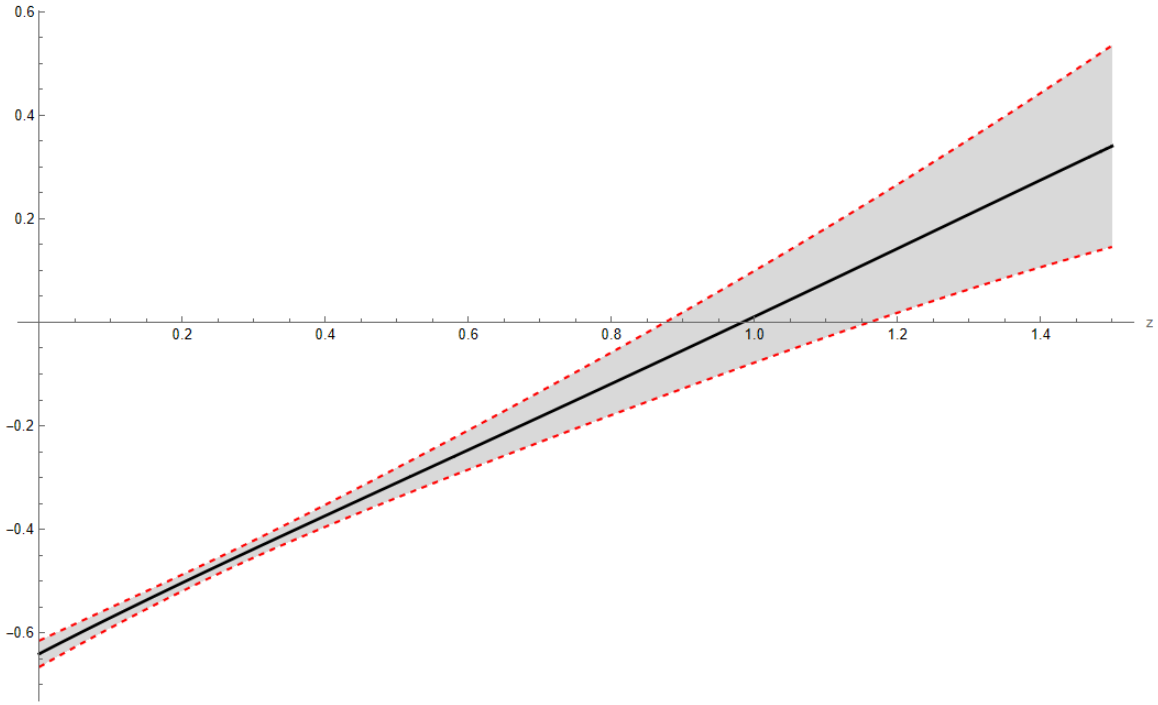


Figure 4.4. Reconstructed effective equation of state parameter $w(z) = p(z)/\rho(z)$ using the representative function (y5–F3) for the flat curvature case. The present-day value is $w(0) = -0.64$, indicating accelerated expansion. At higher redshifts, $w(z)$ increases toward 0, consistent with a matter-dominated universe.

the error band of the representative fit y5–F3, which was shown to closely match the average behavior 4.5. We do not make a Taylor expansion for two reasons, the first being that a Taylor expansion will also be influenced by the behaviour of the function beyond the range, where it is not really representative of our data; and the second, that it will not allow incorporation of the errors which are not uniformly spread along z. The weighted least-squares fit yields

$$w(z) \approx -0.64 + 0,66z - 0.01z^2 \tag{4.14}$$

where the smallness of the quadratic term confirms that $w(z)$ is well approximated by a linear form across the redshift range considered. If we then default to a linear fit

using same synthetic data and errors (weights), we get

$$w(z) \approx -0.63 + 0.65z. \tag{4.15}$$

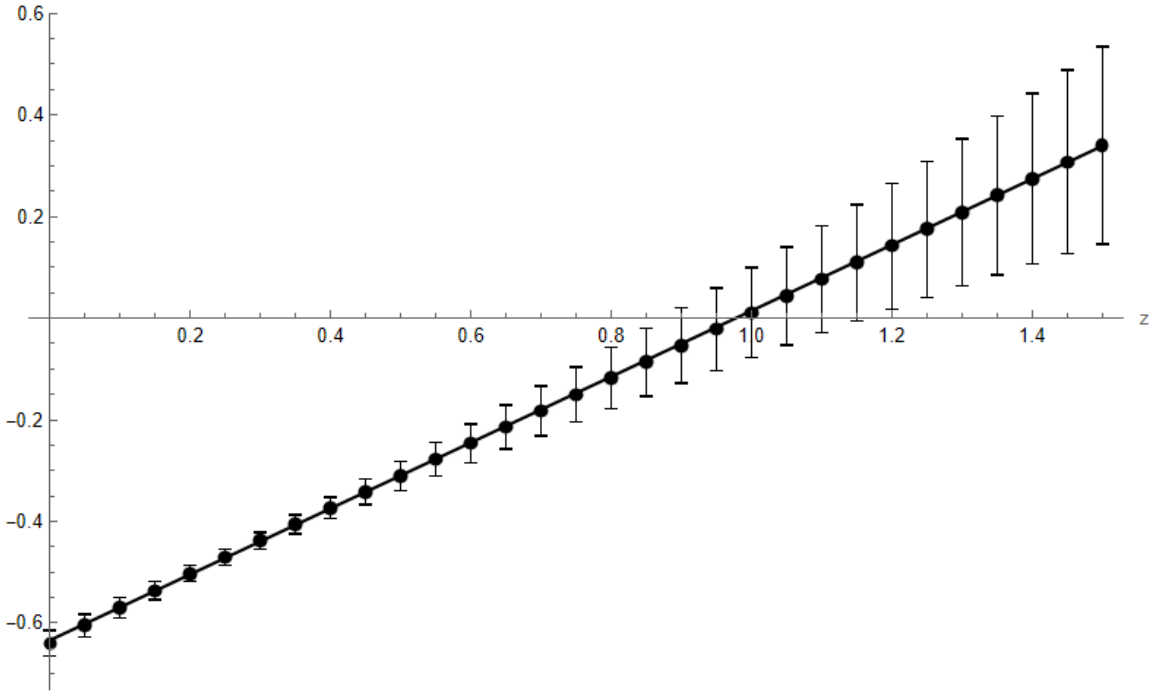


Figure 4.5. Reconstructed effective equation of state $w(z)$ using the representative fit (y5-F3) for the flat case. The dots shows the reconstructed $w(z)$; the black line is the best-fit linear model $w(z) \approx -0.63 + 0.65z$. The near-linearity supports the use of low-order parametrizations for describing the equation of state in this redshift range.

It is important to emphasize that the $w(z)$ reconstructed here represents the effective equation of state of the total cosmic fluid, derived directly from the total energy density and pressure as inferred from the expansion history. It does not rely on any explicit separation between matter and dark energy components. We also note that the computation of $w(z)$ relies on both $\dot{a}(z)$ and $\ddot{a}(z)$, and is thus sensitive to small fluctuations in the input $d_L(z)$ fits, the y5-F3 representative fit was selected because its resulting $\ddot{a}(z)$ curve most closely matches the average of all physically acceptable

reconstructions (see Section 3.3). We therefore consider it a reliable proxy for extracting the effective equation of state.

4.4. CPL Fit to the Reconstructed Hubble Function

We now investigate whether a cosmological model with the somewhat popular time-varying equation of state of the Chevallier–Polarski–Linder (CPL) [28, 29] form provides a better fit to the reconstructed expansion history than ΛCDM. The CPL parametrization assumes

$$w_0 + w_a \frac{z}{1+z} \tag{4.16}$$

and predicts a Hubble function of the form:

$$H(z) = H_0 \sqrt{\Omega_m (1+z)^3 + \Omega_{CPL} g(z)}, \tag{4.17}$$

where

$$g(z) = \exp\left[\int_0^z \frac{1+w(z')}{1+z'} dz'\right] = (1+z)^{3(1+w_0+w_a)} \exp\left[-3w_a \frac{z}{1+z}\right]. \tag{4.18}$$

Here, $\Omega_{\mathrm{CPL}} = 1 - \Omega_{\mathrm{m}}$ ensures flatness.

We fit this model to $H(z)$ data reconstructed as described in the above subsection. The resulting best-fit parameters are:

$$H_0 \approx 73.1 \pm 0.3 \text{ km/s/Mpc}, \ \Omega_m = 0.47, \ w_0 \approx -1.17, \ w_a \approx -1.41. \tag{4.19}$$

These values indicate a present-day equation of state more negative than a cosmological constant, and a significant evolution toward less negative values at higher redshift.

To assess the robustness of the result, we also performed a fit with H_0 fixed to the reconstructed value $H(z = 0) = 73.2$ km/s/Mpc. This fixed-H_0 fit produced a slightly higher BIC value, with ΔBIC=4, favoring the floating-H_0 model. Additionally, the CPL model fit provides a substantially lower BIC value than the ΛCDM fit described in Section 4.2, indicating a better overall description of the reconstructed expansion history.

Figure 4.6 shows the reconstructed $H(z)$ (red curve) with 1-σ uncertainty band (light gray shaded area between dotted red curves), overlaid with the best-fit CPL model (black solid line). The CPL curve closely follows the reconstructed expansion for $z < 1$, but approaches the edge of the 1-σ interval as z grow towards 1.5.

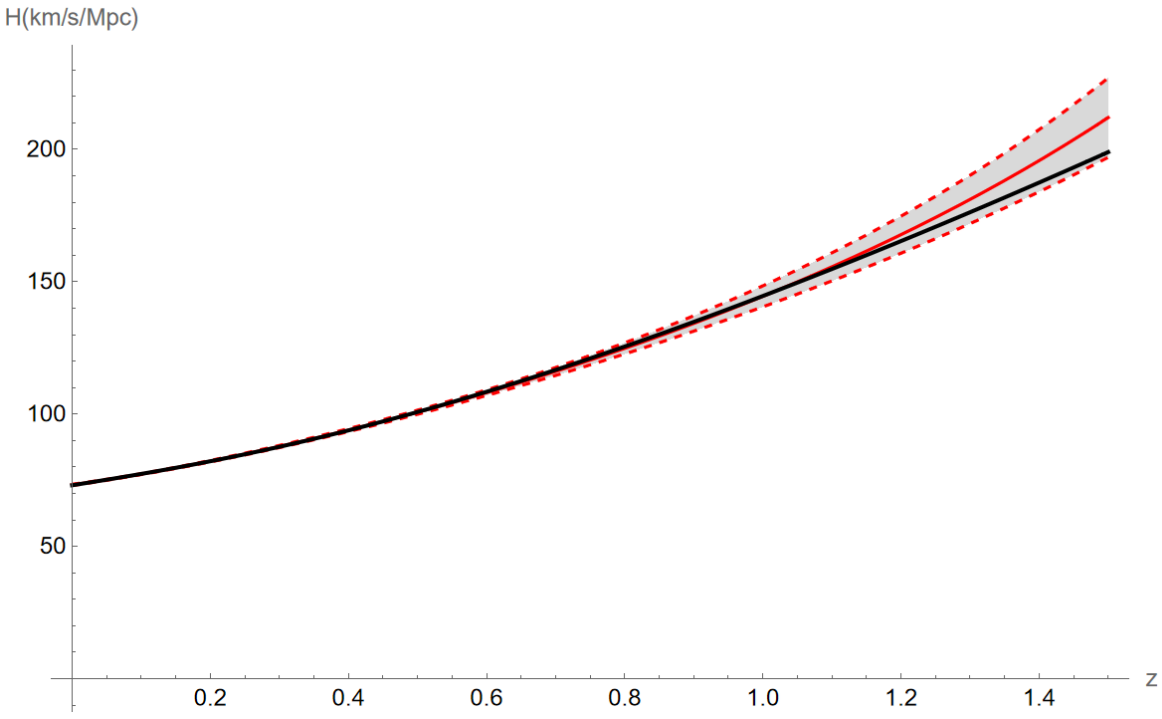


Figure 4.6. Reconstructed Hubble parameter $H(z)$ from the average of 24 accepted $\dot{a}(z)$ functions (red), with 1-σ uncertainty band derived from the representative y5–F3 reconstruction (dotted red curves, shaded region). The best-fit CPL model is shown in black.

4.5. Reconstructing $w(z)$ of Dark Energy

Our spread-LDF procedure gave us the total energy density of the universe as a function redshift via Eq. (4.1). We previously recalled that the matter energy density has the form (4.2), and the balance is what is usually called dark energy, and used this relationship to derive an upper-bound on matter density and lower-bound on dark energy density in section 4.1. Now we want to focus on the mentioned balance, but we do not really know $\rho_m(0)$. The usually quoted Ω_m value of 0.3 comes from the concordance ΛCDM model, and we do not want to make that assumption here. But we do have the upper-bound of 0.48 from section 4 .1 and a lower-bound of $\approx$0.2 from dynamical (non-cosmological) measurements up to the scale of galaxy clusters. So we decide to plot the density of dark energy as function of redshift for Ω_m values 0.2, 0.25, 0.3, 0.35, 0.4 and 0.45 (Figure 4.7) to see how we can proceed. We also plot the corresponding $w_{\rm DE}(z)$ curves (Figure 4.8). The latter figure can be compared with the CPL w(z) curves shown in Figure 4.9, where we held w_0 fixed (changing it would simply move all the corresponding graphs vertically up or down) and plotted curves for a range of w_a values. It is apparent that none of the CPL $w(z)$ curves has similar qualitative features to any of the $w_{\rm DE}(z)$ curves. It is tempting to try an alternative $w_{\rm DE}(z)$ parametrization, (e.g. the curves of another parametrization that can be found in the literature, the Barboza-Alcaniz parametrization [30], are also qualitatively dissimilar) but finding a reasonably simple one seems to be a prohibitive task. In fact, a $w_{\rm DE}(z)$ parametrization may not be the most "physical" approach, as we will discuss in the next section.

4.6. Evidence for sign-change in the EoS of (Generalized) Dark Energy

In producing the $w_{\rm DE}(z)$ curves (Figure 4.8), we naturally used the expression of pressure, Eq. (4.11), which we divided by the density of dark energy, similar to Eq. (4.12). It turns out that the pressure (rather, the average of the pressures resulting from the spread of the fitted luminosity distance functions) changes from negative to positive at $\approx$0.98 (Figure 4.10), hence, the sign of $w_{\rm DE}(z)$, will switch sign at the same

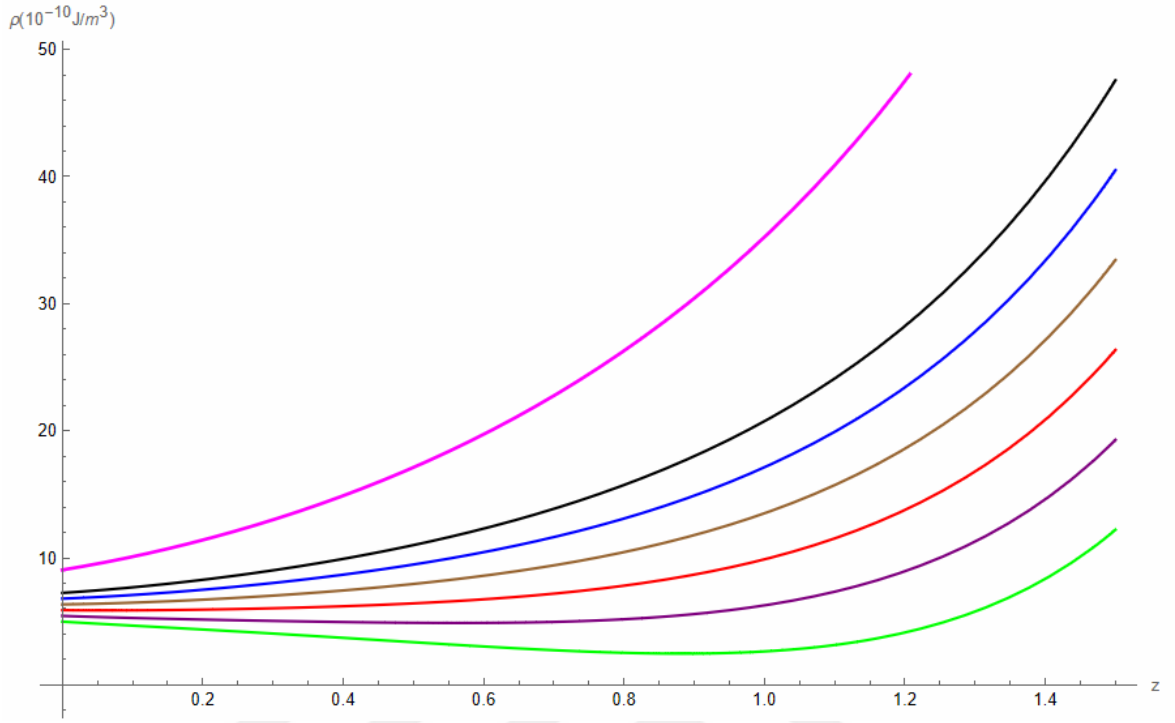


Figure 4.7. Reconstructed average dark energy density $\rho_{\mathrm{DE}}(z)$ for different values of $\Omega_m \in (0.2, 0.25, 0.3, 0.35, 0.4, 0.45)$. Each curve is obtained by subtracting the matter contribution $\rho(0)\Omega_m(1+z)^3$ from the total average reconstructed $\rho(z)$. The curves are ordered from top to bottom according to increasing Ω_m.

redshift. This is the reason why all curves in Figure 4.8 have the same z-intercept. Each curve has one intercept and no singularity, since we assume the energy density of dark energy to be always positive. In fact, this is how we derived an upper-bound on the present matter density; to get negative energy density of dark energy (around $z \approx 1$) we would have to assume an even larger Ω_m. In other words, it appears that adopting sign-changing dark energy [31, 32] requires increasing Ω_m substantially. But positive pressure for $z > 1$ seems to be a quite significant claim, not compatible with matter or cosmological constant. Radiation does have positive pressure, however radiation domination is supposed to have ended long ago, around $z \approx 1000$. So let us look at the graphs more closely, and instead of looking at the average of the spread of 24 functions, let us plot them separately (Figure 4.11). We can see that most curves do make a transition to positive pressure, although a few curves behave very differently from the rest (another illustration of the danger of getting trapped in a discordant

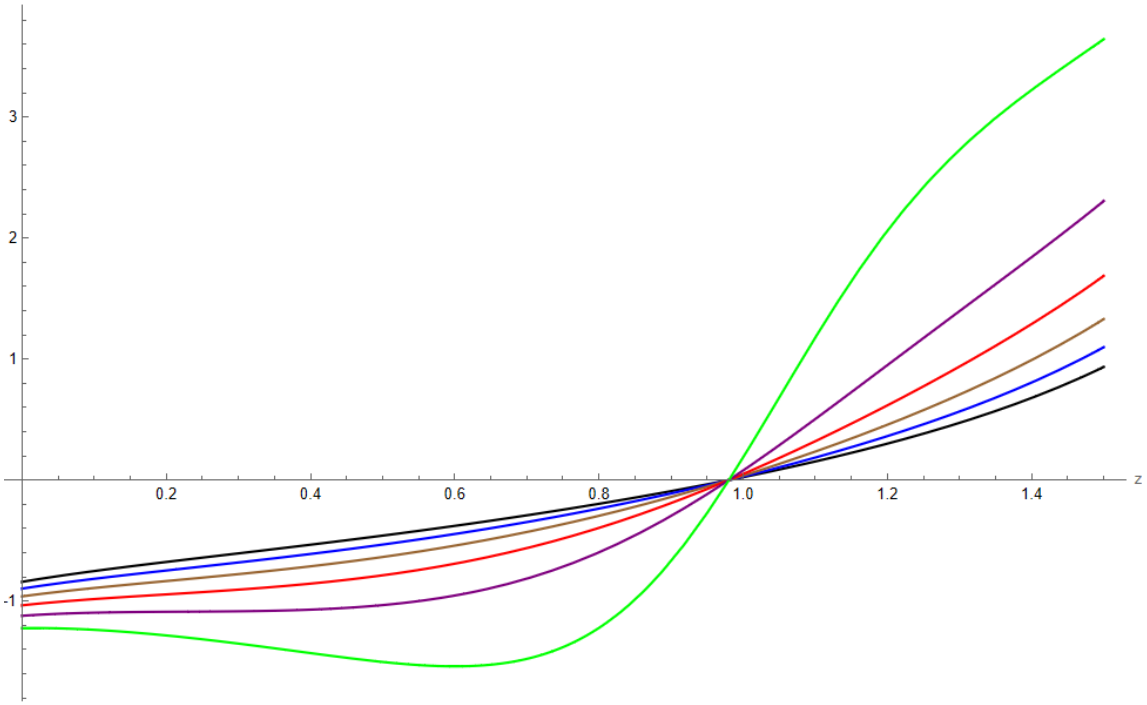


Figure 4.8. Reconstructed equation of state parameter $w_{\mathrm{DE}}(z)$, obtained from the previously derived $\rho_{\mathrm{DE}}(z)$ and the reconstructed pressure $p(z)$. The curves correspond to the same $\Omega_m$values as in Figure 4.7: (0.2, 0.25, 0.3, 0.35, 0.4, 0.45), with colors matched accordingly.

model by making unlucky assumptions, without strong physical motivation). This increases our confidence in the transition from negative p to positive p. However, it is desirable to continue this investigation for higher values of z, where SnIa data are not available. Recently, there have been significant efforts to standardize sources up to $z \approx 8$, GRB's [33] and quasars [34, 35], and we plan to do this in future work.

4.6.1. Reconstructed Equation(s) of State for Generalized Dark Energy

So far, we have discussed $w_{\mathrm{DE}}(z)$, however, the w parameter is not epistemologically very meaningful if it is not constant. For example, in FLRW cosmology we can say that $\rho \approx a^{-3(1+w)}$ if w is constant, but we cannot express ρ in terms of w directly if w is variable. In fact, strictly speaking, the equation of state in physics is a relation between pressure and density, (in most contexts, usually entropy per fluid particle is assumed constant). Until recently, in cosmology the ratio $p/\rho = w$ was taken constant

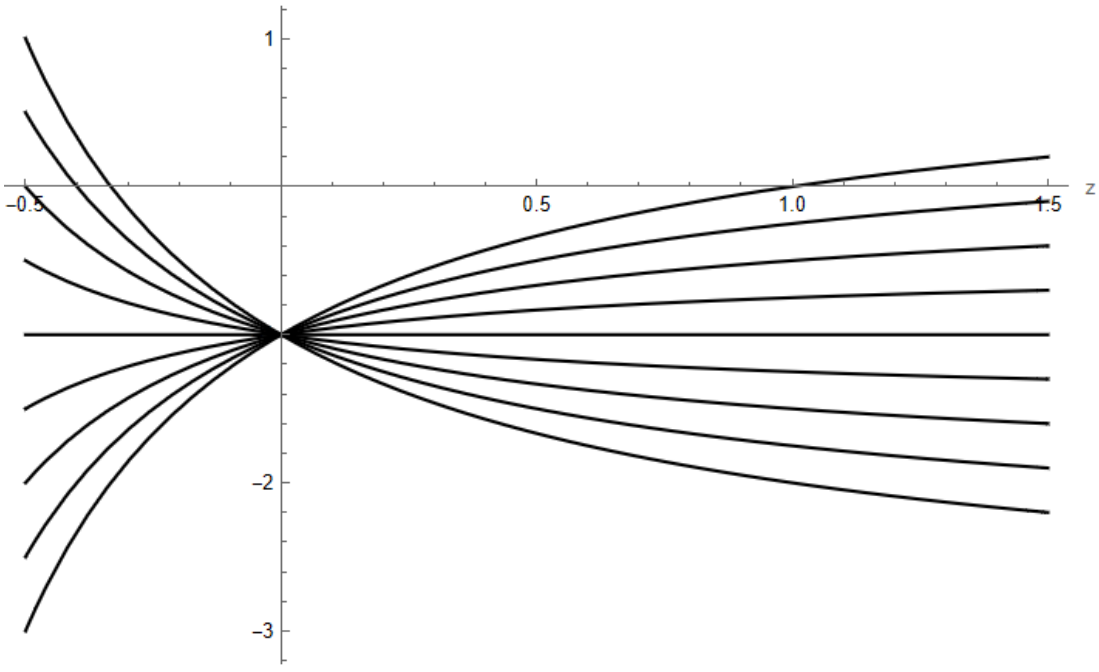


Figure 4.9. CPL parametrization of the dark energy equation of state $w(z)$ for various values of w_a, with w_0 fixed at -1. The curves illustrate the impact of different w_a values in the range -2, -1.5, -1, -0.5, 0, 0.5, 1, 1.5, 2 on the redshift evolution of $w(z)$.

and called the equation-of-state-parameter, but if it is not constant, as suspected in recent years, it is not very meaningful to use the ratio, one should default back to the relation. Expressing the relation in terms of z does not seem to be very meaningful either: The relation $f(p, \rho) = 0$ is a *local* relation, as befits a fluid consisting of particles, or by causality arguments; but z is not a local variable, there is no apparent reason that the local behaviour of a fluid should depend on z, the redshift, or indirectly, the age of the universe (time-translational invariance of laws of physics). One might argue that z also determines the scale of the universe, or in non-flat cases, its curvature; the answer for the latter aspect is the equivalence principle, that local physics can be applied as if the universe is locally flat, and the answer for the former aspect is partially the same principle, partially the principle of causality/locality, that what happens far away in the universe cannot significantly affect what happens here.

Hence we decide to investigate the relation between pressure and density of the non-matter part of the source of Einstein equations, as derived from the data. We

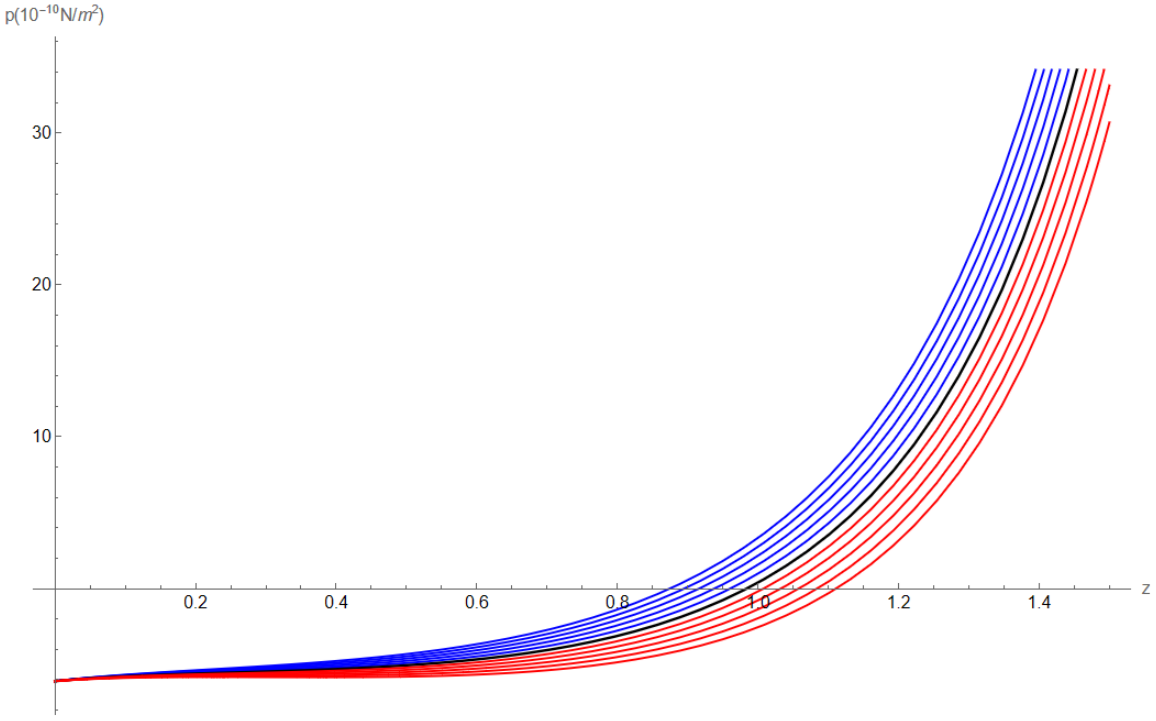


Figure 4.10. Average reconstructed pressure for 11 values of the curvature parameter κ. Black curve correnspponds to flat case; red and blue represent positive and negative curvature, respectively.

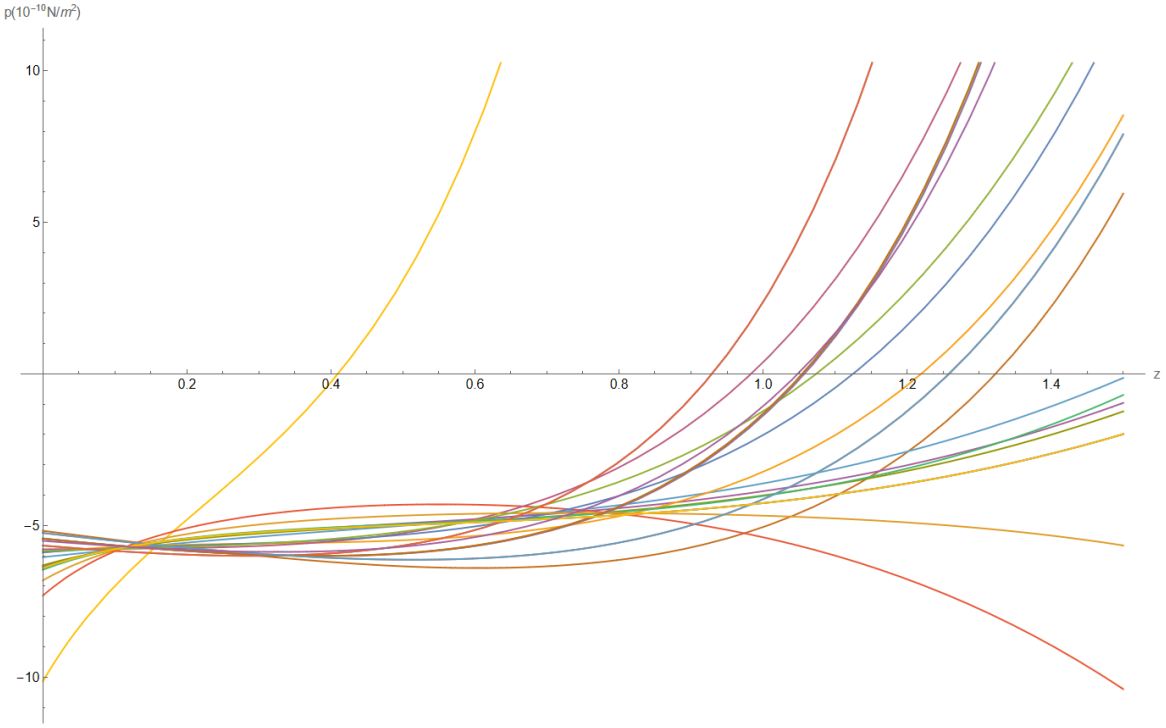


Figure 4.11. Reconstructed pressure as a function of redshift for all selected functions.

decide to call that part "Generalized Dark Energy", (GDE) since the concept of Dark Energy (DE) was invented to provide a source for accelerated expansion of the universe, hence has to satisfy $\rho + 3p < 0$, however, the source we find can have both energy density and pressure positive, so it can violate the DE property. So we plot in Figure 4.12 parametrically p as function of ρ, again for the different Ω_m values used in Figure 4.7. We attempted to find functions that would reproduce the dependence shown in the figure, at least for the single-valued curves, and quadratics gave reasonable fits, better than for example, an exponential version we tried. As discussed above, the disturbing

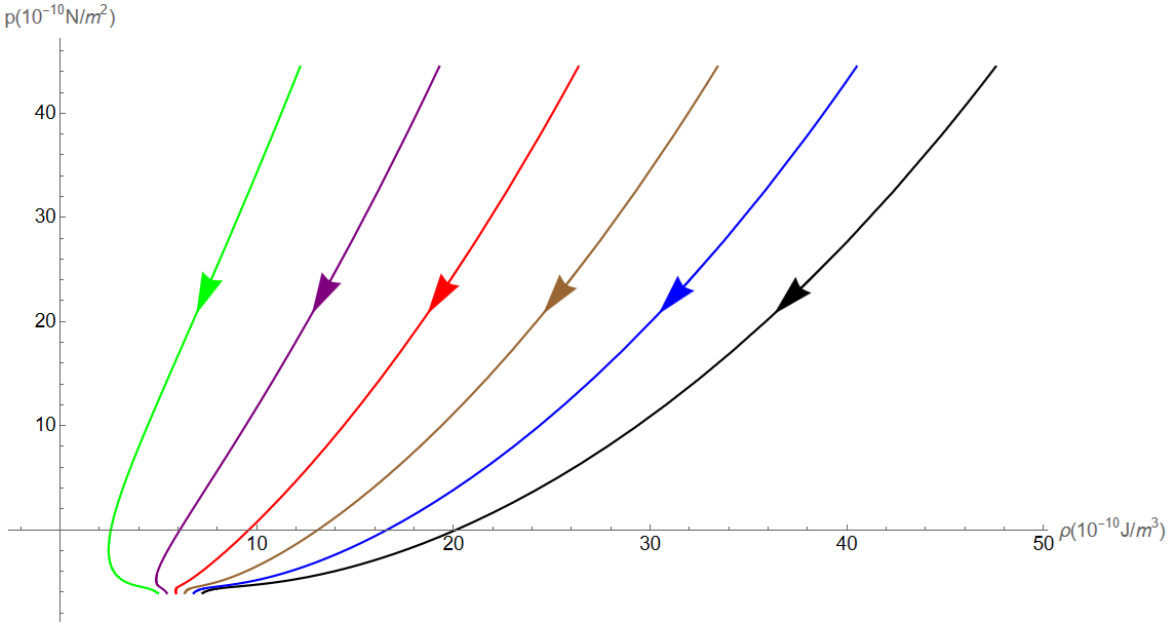


Figure 4.12. Parametric function pressure in terms of dark energy density. The curves correspond to the same Ω_m values as in Figure 4.7: (0.2, 0.25, 0.3, 0.35, 0.4, 0.45), with colors matched accordingly.

possibility of a transition to positive pressure around $z \approx 1$ should be rechecked with new and alternative data. If confirmed, one would have to look for models of sources that can account for the feature, maybe a kind of dark radiation becoming dominant in that redshift range. But coming up with different ad hoc sources for different epochs would look epicyclical, so either a well-motivated particle/field model should be found to explain the GDE EoS over the whole range, or the assumptions leading to this result should be questioned: The Cosmological Principle, leading to LTB-like models or backreaction arguments, that is, effects of structure formation on assumed large-scale

metric (subject of the rest of this thesis); the standardization of the candles [36], since they are the cornerstone observational support of the accelerating expansion concept; and the theory of gravity, namely, GR, leading to modified-gravity theories.

5. EXTENDING MODEL-INDEPENDENT ANALYSIS TO RADIALLY INHOMOGENEOUS SPACETIMES

The standard cosmological model, based on the FLRW metric, has been remarkably successful in describing a wide range of observations under the assumption of spatial homogeneity and isotropy. However, this model also requires the introduction of a dominant dark energy component—an otherwise unknown form of energy—to account for the observed accelerated expansion. Given that our observations are limited to the past light cone and our location may not be representative of the global average, it is worth questioning whether some of the inferred acceleration could result from geometric effects rather than exotic energy components. In this section, we explore a radially inhomogeneous but isotropically expanding spacetime to investigate whether curvature inhomogeneities alone can partially reproduce the observed acceleration signal. We adapt our model-independent reconstruction techniques to this generalized geometry and examine their implications.

5.1. Validity of Our Method in Inhomogeneous Geometry

In this subsection, we justify the applicability of our previously developed model-independent method for extracting cosmological information from luminosity distance data to a class of inhomogeneous metrics. Specifically, we consider a radially inhomogeneous but spherically symmetric spacetime described by the line element:

$$ds^2 = -c^2dt^2 + a(t)^2[b(r)^2dr^2 + r^2(d\theta^2 + \sin^2\theta d\phi^2)]. \tag{5.1}$$

Here, the time-dependent scale factor $a(t)$ governs the overall expansion, while the spatial inhomogeneities are introduced via the radial function $b(r)$. Because the metric is spherically symmetric and the spatial curvature is encoded only in $b(r)$, the propagation of light (along radial null geodesics) remains tractable and allows us to carry over much of the formalism developed for the FLRW case.

Because $a(t)$ is the only time-dependent part of the spatial metric, it determines the overall expansion rate of the universe in this model. Importantly, any metric of the form

$$ds^2 = -c^2dt^2 + a(t)^2\gamma_{ij}(x)dx^i dx^j \tag{5.2}$$

admits a natural four-velocity field $u^\mu = (1, 0, 0, 0)$ whose expansion tensor is

$$\Theta_{ij} = \nabla_{(i}u_{j)} = \frac{\dot{a}}{a}h_{ij} \tag{5.3}$$

with $h_{ij} = a(t)^2\gamma_{ij}(x)$ the spatial metric. This expansion is shear-free and locally isotropic, since all directions at a given point stretch at the same rate $\dot{a}/a$. Hence, despite spatial inhomogeneity, the expansion remains isotropic and is governed entirely by $a(t)$, justifying our treatment of redshift and expansion in analogy to FLRW.

Despite the inhomogeneity, the form of the redshift–scale factor relation remains identical to the FLRW case, $a(t) = a_0/(1 + z)$. This holds because $a(t)$ is the only time-dependent term in the spatial part of the metric, and hence determines the overall cosmic expansion experienced by null rays. A simple argument using two wave crests emitted at times t_e and $t_e + \epsilon$ and received at t_0 and $t_0 + \epsilon$ (as used in standard FLRW derivations) confirms this. Moreover, since the radial part of the metric is separable into $a(t)^2b(r)^2$, the redshift expression derived from the geodesic equations remains unchanged.

The angular diameter distance in this metric is given by:

$$d_A = \frac{a_0}{1 + z}r \tag{5.4}$$

and thus the luminosity distance becomes:

$$d_L = (1 + z)^2 d_A = a_0(1 + z)r. \tag{5.5}$$

This is structurally identical to the FLRW result. Therefore, any empirical or fitted model for $d_L(z)$ can be used in the same way as before, without the need to modify the definition of distance observables.

Given the above relations, and assuming that we have a fit for $d_L(z)$, we can again write:

$$\frac{dt}{dz} = -\frac{1}{c(1+z)} b\left(\frac{d_L}{(1+z)a_0}\right) \frac{d}{dz}\left(\frac{d_L}{(1+z)}\right). \tag{5.6}$$

This generalizes the expression derived in the FLRW case by introducing a correction factor $b(r)$ that accounts for spatial inhomogeneities. Once dt/dz is known, we can use the chain rule and the redshift-scale factor relation $a(z) = a_0/(1+z)$ to compute $\dot{a}(z)$, $\ddot{a}(z)$, and eventually derive quantities like the deceleration parameter or effective equation of state as before.

The key idea is that, due to the structure of the metric, the redshift–scale factor relation and the form of the luminosity distance remain unchanged. This allows us to reuse our model-independent techniques—originally developed in the context of FLRW cosmology—for a wider class of inhomogeneous models. The only modification required is the inclusion of the spatial inhomogeneity function $b(r)$ in the expression for dt/dz. Therefore, the entire formalism of reconstructing the expansion history from $d_L(z)$ fits remains valid in this setting.

5.2. Modified Field Equations in the Inhomogeneous Metric

To interpret the reconstructed expansion history within the context of our radially inhomogeneous spacetime, we now present the Einstein field equations derived from the metric:

$$ds^2 = -c^2dt^2 + a(t)^2[b(r)^2dr^2 + r^2(d\theta^2 + \sin^2\theta d\phi^2)] \tag{5.7}$$

where $a(t)$ governs the global time evolution (the expansion), and $b(r)$ introduces spatial inhomogeneity through the radial curvature structure. The inhomogeneity modifies the spatial geometry but preserves isotropic expansion. As discussed in Section 5.1, the expansion tensor remains proportional to the spatial metric, making the expansion locally isotropic and shear-free. This form enables us to retain the relation $1+z = a_0/a(t)$, and the angular diameter distance and luminosity distances take the same form as in FRW, $d_L(z) = a_0(1+z)r$. Given these, we can reuse our model-independent formalism to reconstruct $\dot{a}(z)$, $\ddot{a}(z)$ and $H(z)$, and now seek to interpret these results using the field equations for the new geometry.

Using the Einstein equations with a perfect fluid energy–momentum tensor, the G_0^0 and G_i^i components yield generalized Friedmann-like equations. Denoting the energy density and pressure as $\rho(t,r)$ and $p(t,r)$, we obtain:

$$H^2 = \frac{\dot{a}}{a} = \frac{8\pi G}{3c^2}\rho - \frac{c^2}{3}\left[\frac{1}{r^2} + 2\frac{b'}{rb^3} - \frac{1}{r^2b^2}\right]\frac{1}{a^2}, \tag{5.8}$$

$$\frac{\ddot{a}}{a} = -\frac{4\pi G}{3c^2}\left(\rho(t,r) + p_r(t,r) + 2p_\theta(t,r)\right). \tag{5.9}$$

Equation (5.8) generalizes the first Friedmann equation to include a radial dependence in the curvature term, it comes from G_0^0. The term in parentheses can be interpreted as a generalized curvature function, which may vary with r, depending on the choice of $b(r)$. Equation (5.9) retains the same form as the FRW acceleration equation, now radial pressure is different from angular pressures. It is derived using G_α^α (α from 0 to 3).

The covariant conservation of the energy–momentum tensor yields the continuity equation:

$$\dot{\rho} + 3\frac{\dot{a}}{a}\left(\rho + \frac{p_r}{3} + \frac{2p_\theta}{3}\right) = 0. \tag{5.10}$$

This equation is similar in form to the FRW case, and governs the time evolution of the energy density at each fixed spatial point. For pressureless dust ($p = 0$), it leads

to:

$$\rho(t,r) \propto a(t)^{-3} \;\rightarrow\; \rho(z,r) \propto (1+z)^3 \tag{5.11}$$

Thus, even in the presence of spatial inhomogeneity, each spatial shell evolves like matter in FRW. The amplitude $\rho_0(r)$ may vary with radius, but the redshift dependence follows the familiar scaling.

These equations justify the use of a modified Friedmann-like expression when fitting $H(z)$ in this inhomogeneous context. Since the curvature term in equation (5.8) scales effectively as $\propto a^{-2} \propto (1+z)^2$, and the matter term evolves as $\propto (1+z)^3$, we are motivated to fit reconstructed Hubble data using:

$$\left(\frac{H(z)}{H_0}\right) = \sqrt{\Omega_m(1+z)^3 + \Omega_k(1+z)^2 + \Omega_X} \tag{5.12}$$

with

$$\Omega_m + \Omega_k + \Omega_X = 1 \tag{5.13}$$

where

$$\Omega_m = \frac{8\pi G}{3H_0^2}\rho_{m_0}, \tag{5.14}$$

$$\Omega_k = -\frac{c^2}{3H_0^2}\left[\frac{1}{r^2} + 2\frac{b'}{rb^3} - \frac{1}{r^2b^2}\right]\frac{1}{a_0^2}. \tag{5.15}$$

They represent the effective curvature, matter, and residual (dark) energy components, respectively.

This form generalizes the standard flat ΛCDM model and allows us to assess how much of the observed expansion history can be attributed to curvature inhomogeneities rather than a cosmological constant.

5.3. Extracting Effective Density Parameters from Reconstructed $H(z)$

Having established the form of the modified Friedmann equations for our radially inhomogeneous spacetime in Section 5.2, we now turn to fitting our reconstructed Hubble parameter $H(z)$ with the corresponding generalized expression. The aim is to quantify how much of the observed expansion history can be accounted for by inhomogeneous curvature and matter, and whether a dark energy component remains necessary.

To do this, we use the average of the 24 accepted $\ddot{a}(z)$ functions (as defined in Section 3.3), computed within the inhomogeneous model using the profile:

$$b(r)^2 = 1 + \frac{1}{1 + r^2 + \epsilon \sin r}, \tag{5.16}$$

with $\epsilon = 5.2$, a value chosen to ensure that the average acceleration $\ddot{a}(z)$ remains negative over the entire redshift range while maintaining positive energy density. The resulting average acceleration function $\ddot{a}(z)$, shown in Figure 5.1, remains strictly negative throughout the redshift range considered.

The reconstructed Hubble parameter is then calculated via $H(z) = (1 + z)\dot{a}(z)$, and normalized by its present-day value, H_0, yielding the dimensionless function $H(z)/H_0$. Since propagating full uncertainties from all 24 functions would be computationally intractable, we again adopt the uncertainty band $\sigma_H(z)$ derived from the representative fit y5-F3 as an effective 1-σ error band for the average. This method was previously shown to be a reliable approximation in Section 4.2.

We then fit the reconstructed $H(z)/H_0$ with the expression motivated by equation (5.8):

$$\left(\frac{H(z)}{H_0}\right) = \sqrt{\Omega_m^{\text{eff}}(1+z)^3 + \Omega_k^{\text{eff}}(1+z)^2 + 1 - \Omega_m^{\text{eff}} - \Omega_k^{\text{eff}}}. \tag{5.17}$$

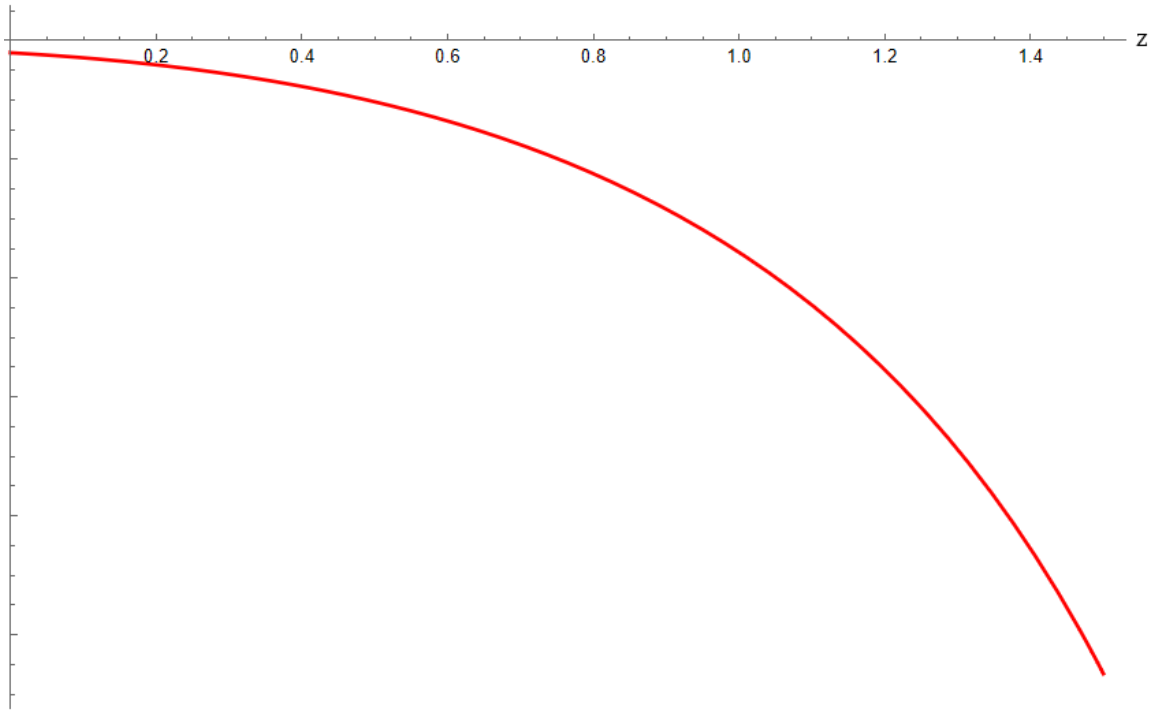


Figure 5.1. Average reconstructed acceleration $\ddot{a}(z)$ for the chosen inhomogeneous profile. The result remains negative over the entire redshift range, indicating that the observed expansion history may be explained without invoking accelerated expansion in this model.

We consider two versions of the fit:

- One in which H_0 is treated as a free parameter,
- One in which H_0 is fixed to the reconstructed value $H_0 \approx 51.7$ km/s/Mpc.

The fixed$-H_0$ case yields a lower Bayesian Information Criterion (BIC), indicating a statistically preferred fit. The best-fit(Figure 5.2) parameters for this case are(effective density parameters):

$$\Omega_m^{\text{eff}} \approx 0.50, \quad \Omega_k^{\text{eff}} \approx 0.22, \quad \Omega_X^{\text{eff}} \approx 0.28. \tag{5.18}$$

These values indicate that a substantial portion of the expansion can be attributed to spatial curvature and ordinary matter, with a significantly reduced need for dark energy

compared to standard ΛCDM (where typically $\Omega_m \approx 0.3$, $\Omega_k \approx 0$, and $\Omega_\Lambda \approx 0.7$).

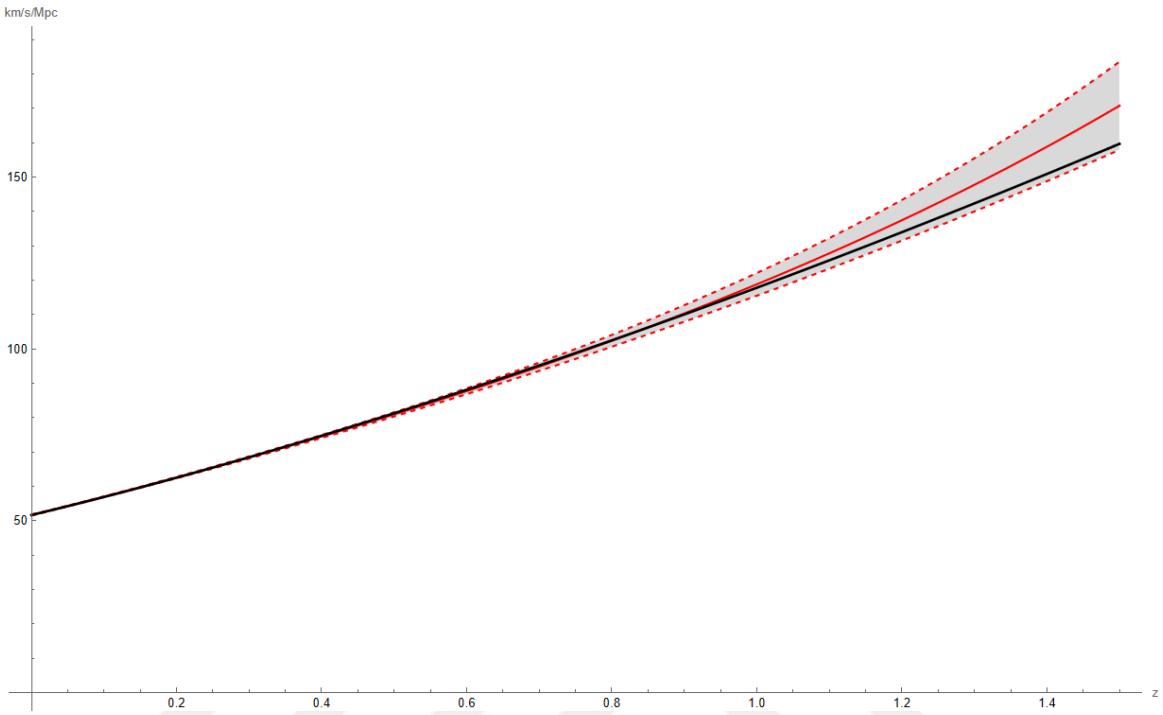


Figure 5.2. Reconstructed Hubble parameter $H(z)$, obtained by averaging the 24 accepted $\dot{a}(z)$ functions within the inhomogeneous model using $b(r, \epsilon = 5.2)$. The shaded region represents the 1-σ confidence band derived from the y5–F3 representative function. The black curve shows the best-fit model of the form $H(z)/H_0$, with parameters given in the text.

For fitting purposes, we define effective cosmological parameters $\Omega_m^{\text{eff}}(z)$ and $\Omega_k^{\text{eff}}(z)$, corresponding to the matter and curvature. We emphasize that these values represent effective parameters, reconstructed along the observer's past light cone. In the inhomogeneous model, energy density and curvature vary spatially, so these quantities should not be interpreted as global averages. Nonetheless, the analysis illustrates that spatial inhomogeneities—particularly in curvature—can influence the inferred expansion history in ways that mimic acceleration. This highlights the importance of geometric assumptions in the interpretation of cosmological data, and provides a concrete demonstration of how relaxing homogeneity can affect our understanding of cosmic dynamics.

Alternatively, one could interpret the expansion equation through the lens of spatial averaging, in the spirit of Buchert's formalism [15]. While our primary reconstruction follows the observer's past light cone, we may also consider averaging the generalized Friedmann equation (Eq. (5.8)) over a spatial domain at fixed cosmological time. In doing so, we note that the left-hand side of the equation, $H^2 = (\dot{a}/a)^2$, remains unaffected by averaging, since H is purely a function of time in our isotropically expanding metric. However, the right-hand side—comprising the position-dependent energy density and curvature terms—does change under averaging. The form of the averaged equation remains the same, featuring terms that scale as $(1+z)^2$, $(1+z)^3$, and a constant, and thus the same fitting procedure and resulting ω-parameters apply. What changes, however, is their interpretation: instead of encoding the effective energy contributions along the observer's light cone, they now represent spatial averages over constant-time hypersurfaces. This dual perspective reinforces the robustness of the result—namely, that a large portion of the apparent acceleration can emerge from spatial curvature structure, whether considered observationally or geometrically.

The analysis in this section shows that introducing a modest degree of radial inhomogeneity—through a varying curvature function—can notably shift the inferred energy content required to explain the observed expansion history. While we do not eliminate the need for dark energy, the effective energy budget derived from the generalized Friedmann equations suggests that part of the apparent acceleration may arise from geometric effects rather than unknown components. These results underscore the interpretational role of symmetry assumptions in cosmology and motivate further investigation of inhomogeneous, yet isotropic, spacetimes as meaningful alternatives to fully homogeneous models.

6. EFFECTIVE DYNAMICS FROM SPATIAL AVERAGING: BUCHERT'S FORMALISM

6.1. Spatial Averaging and the Buchert Formalism

In standard cosmology, the dynamics of the universe is described by applying Einstein's equations directly to a homogeneous and isotropic FLRW spacetime. However, on intermediate scales, the real universe exhibits significant inhomogeneity, and it is not guaranteed that Einstein's equations applied to a smoothed-out FLRW metric yield the same effective dynamics as those of the actual inhomogeneous universe. The Buchert formalism [15] addresses this issue by spatially averaging scalar parts of Einstein's equations over inhomogeneous domains, resulting in effective evolution equations for a domain-dependent scale factor $a_D(t)$, which captures the averaged expansion behavior of the inhomogeneous universe.

For a general irrotational dust spacetime, the metric can be written in synchronous and comoving gauge as

$$ds^2 = -dt^2 + h_{ij}(x, y, z, t)dx^i dx^j. \tag{6.1}$$

where h_{ij} is the 3-metric on constant-time hypersurfaces

The Einstein equations take the form

$$G_{\alpha\beta} = 8\pi G T_{\alpha\beta} = 8\pi G \rho u_\alpha u_\beta \tag{6.2}$$

where $T_{\alpha\beta}$ is the energy-momentum tensor for pressureless dust, ρ is energy density and u^α is the four-velocity vector of the comoving observers.

The covariant derivative u_α can be decomposed into scalar, traceless symmetric, and antisymmetric parts:

$$\nabla_\beta u_\alpha = \frac{1}{3} h_{\alpha\beta}\Theta + \sigma_{\alpha\beta} + \omega_{\alpha\beta}, \tag{6.3}$$

where $h_{\alpha\beta}$ is the first fundamental form (metric of the hypersurface orthogonal to u^α). The trace $\Theta = \nabla_\alpha u^\alpha$ is the expansion scalar, the traceless symmetric part, $\sigma_{\alpha\beta}$, is the shear tensor and the antisymmetric part, $\omega_{\alpha\beta}$, is the vorticity tensor. In FRW spacetimes, the shear and vorticity vanish, and $\Theta = 3H$.

By projecting Einstein's equations onto spatial hypersurfaces orthogonal to u^α, one obtains the scalar evolution equations:

$$\frac{1}{2}{}^3R + \frac{1}{3}\Theta^2 - \sigma^2 = 8\pi G\rho + \Lambda, \tag{6.4}$$

$$\dot{\Theta} + \frac{1}{3}\Theta^2 + 2\sigma^2 + 4\pi G\rho - \Lambda = 0, \tag{6.5}$$

$$\dot{\rho} = -\Theta\rho \tag{6.6}$$

where the dot is the derivative with respect to proper time t, $\sigma^2 = \frac{1}{2}\sigma^i_j\sigma^j_i$ is the rate of shear, ${}^3R$ is the Ricci scalar of the 3-hypersurface of contant t. The Hamiltonian constraint (6.4) is the local equivalent of the Friedmann equation for an arbitrary dust spacetime, and it relates the expansion rate to the energy density, spatial curvature, shear. The Raychaudhuri equation (6.5) gives the local acceleration. Equation (6.6) shows simply that the energy density is proportional to the inverse of the volume, in other words that mass is conserved. Vorticity tensor is zero since Buchert works with irrotational dust.

The Buchert formalism introduces the spatial average of a scalar quantity $\Psi(t, x^i)$ over a comoving domain D as

$$\langle\Psi(t, x^a)\rangle_D = \frac{1}{V_D}\int_D \sqrt{h}dx^3\Psi(t, x^a) \tag{6.7}$$

where V_D is the volume of the comoving domain and h is the determinant of the first fundamental form. With this definition and using the commutation relation

$$\langle\Theta\rangle\dot{}_D - \langle\dot{\Theta}\rangle_D = \langle\Theta^2\rangle_D - \langle\Theta\rangle_D^2\,, \tag{6.8}$$

the scalar equations (6.4)-(6.6) can be averaged to obtain Buchert's equations [15]:

$$3\left(\frac{\dot{a}_D}{a_D}\right)^2 - 8\pi G\,\langle\rho\rangle_D + \frac{1}{2}\,\langle R\rangle_D - \Lambda = -\frac{Q_D}{2}, \tag{6.9}$$

$$3\frac{\ddot{a}_D}{a_D} + 4\pi G\,\langle\rho\rangle_D - \Lambda = Q_D, \tag{6.10}$$

$$\langle\dot{\rho}\rangle_D = -\,\langle\Theta\rangle\,\langle\rho\rangle\,. \tag{6.11}$$

Where $\langle R\rangle_D$ is the averaged spatial Ricci scalar, and Q_D is the kinematical backreaction term which encodes the influence of inhomogeneities on the effective expansion rate,

$$Q_D = \frac{2}{3}(\langle\Theta^2\rangle_D - \langle\Theta\rangle_D^2) - 2\,\langle\sigma^2\rangle_D\,. \tag{6.12}$$

The effective scale factor $a_D(t)$ is defined such that the volume of the domain satisfies $V_D(t) \propto a_D(t)^3$,

$$a_D(t) = \left(\frac{\int_D \sqrt{h(t,x^a)}dx^3}{\int_D \sqrt{h(t_0,x^a)}dx^3}\right)^{1/3}, \tag{6.13}$$

where a_D has been normalized to unity at time t_0. Since the expasion, Θ, gives fractional rate of change of the volume, the averaged expansion rate may be written in terms of the scale factor:

$$\langle\Theta\rangle_D = \frac{\dot{V}_D}{V_D} = 3\frac{\dot{a}_D}{a_D}. \tag{6.14}$$

The system is closed by the integrability condition, which ensures consistency between the two dynamical equations (6.9 and 6.10):

$$\dot{Q}_D + 6\frac{\dot{a}_D}{a_D}Q_D + \langle R\rangle^{\cdot}_D + 2\frac{\dot{a}_D}{a_D}\langle R\rangle_D = 0. \tag{6.15}$$

These equations describe how the volume-averaged expansion evolves in the presence of inhomogeneities, encoded in Q_D and $\langle R\rangle_D$. While their structure closely resembles the Friedmann equations, they include additional degrees of freedom that can mimic effects otherwise attributed to dark energy.

In the next subsection, we follow the proposal of Paranjape and Singh [37], who advocate for a "template metric" approach in which one assumes that the universe is effectively FLRW on large scales, allowing standard light propagation and redshift–distance relations to hold. This interpretation allows us to use the same reconstructed expansion history from Section 3—obtained via dt/dz and $d_L(z)$—but now interpreted as describing the evolution of the effective scale factor $a_D(t)$ governed by Buchert's averaged equations.

6.2. Applicability of the FLRW-Based Reconstruction within the Buchert Averaging Framework

In the Buchert formalism, the evolution of the universe is governed by spatial averages over inhomogeneous domains rather than pointwise Einstein equations. While this leads to a modification of the dynamical equations (as discussed in previous section), it raises the question of whether standard observational tools—such as luminosity distance, redshift, and scale factor relations—remain valid in this context.

This issue was addressed in the work of Paranjape and Singh [37], who proposed the use of a template metric (6.16) to describe the observed universe. Their key insight is that while the underlying spacetime may be inhomogeneous and evolve according to Einstein's equations, the average geometry can still be described effectively by a

homogeneous and isotropic metric of FLRW form. In this view, the effective scale factor $a_D(t)$ governs the large-scale volume expansion, obeys Buchert's equations, and standard relations for redshift and luminosity distance can be preserved in a coarse-grained sense.

$$ds^2_{\text{eff}} = -dt^2 + a_D(t)^2 \left(\frac{dr^2}{1 - k_D r^2} + r^2 d\Omega^2 \right). \tag{6.16}$$

Crucially, Paranjape's approach justifies the use of standard light-cone observables—including the relation:

$$1 + z = \frac{a_D(t_0)}{a_D(t)}, \quad d_L(z) = a_D(t_0)(1 + z)r(z), \tag{6.17}$$

as long as one interprets $a_D(t)$ as the domain-averaged scale factor. This directly validates our reconstruction method based on the luminosity distance data. The derivation of dt/dz, which relies on the form of null geodesics and the luminosity distance–redshift relation, remains formally unchanged under this template metric interpretation.

This motivates a powerful idea: since the luminosity distance–redshift relation remains valid in the Buchert setting, we can apply spread-LDF method—originally developed for FLRW cosmology—to this framework with minimal modification. The functions $H_D(z) = \dot{a}_D/a_D$ and $\ddot{a}_D(z)$, reconstructed in Section 3 from luminosity distance data, are now reinterpreted as describing the effective expansion of an averaged inhomogeneous universe, rather than a homogeneous one. This reinterpretation allows us to insert these functions directly into Buchert's equations to constrain effective matter content and roughly quantify the contribution of backreaction.

The spatial Ricci scalar of the effective metric (6.16) is given by $R_{\text{eff}} = \frac{6k_D}{a_D^2}$. However, this represents the Ricci scalar of the averaged geometry, and it generally differs from the domain-averaged Ricci scalar computed from the actual inhomogeneous metric. The discrepancy is denoted by $\mathcal{A}R$, such that the average of the scalar curvature

satisfies

$$\langle R\rangle = \Delta R + \frac{6k_D}{a_D^2}. \tag{6.18}$$

Using this, Buchert's equations can be recast in terms of the effective Ricci scalar as follows:

$$3\left(\frac{\dot{a}_D}{a_D}\right)^2 + 3\frac{k_D}{a_D^2} = 8\pi G\langle\rho\rangle_D - \frac{1}{2}(\Delta R + Q_D), \tag{6.19}$$

$$3\frac{\ddot{a}_D}{a_D} = -4\pi G\langle\rho\rangle_D + Q_D, \tag{6.20}$$

where Q_D denotes the kinematical backreaction term, $\langle\rho\rangle_D$ is the domain-averaged energy density, and a_D is the effective scale factor associated with the averaging domain D.

As discussed in the previous section, Buchert's equations are not closed in their general form; additional assumptions regarding the evolution of the kinematical backreaction Q_D and the averaged spatial curvature are necessary. In [21], the authors propose scaling solutions of the form:

$$Q_D = Q_{D_i}a_D^n, \quad \langle R\rangle_D = R_{D_i}a_D^p, \tag{6.21}$$

where Q_{D_i} and R_{D_i} are constants representing the initial values of the backreaction and curvature, respectively.

A specific solution of the Eq. (6.15) is $n = -6$ and $p = -2$, originally presented in [15], is the only case where $n \neq p$. In this scenario, the backreaction becomes negligible at late times, and the cosmological dynamics asymptotically approach those of a standard FRW universe. As such, we do not focus on this case in the present work.

More generally, when $n = p$, the averaged spatial curvature becomes directly proportional to the kinematical backreaction. This relationship can be written as:

$$Q_{D_i} = rR_{D_i}, \quad r = -\frac{n+2}{n+6}, \quad \text{or equivalently,} \quad n = -2\left(\frac{3r+1}{r+1}\right). \tag{6.22}$$

Solutions of this form for the relation between Q_D and $\langle R\rangle_D$ can be linearly combined to construct new valid solutions. For instance, consider the following two solutions:

$$\langle R\rangle_D = \frac{6k_D}{a_D^2}, \quad Q_D = 0, \tag{6.23}$$

$$\langle R\rangle_D = \frac{\beta}{r}a_D^n, \quad Q_D = \beta a_D^n. \tag{6.24}$$

Their sum yields another valid solution [37]:

$$\langle R\rangle_D = \frac{6k_D}{a_D^2} + \frac{\beta}{r}a_D^n, \quad Q_D = \beta a_D^n. \tag{6.25}$$

With this, Buchert's equations (i.e., the effective Friedmann equations) can be recast in terms of the effective scale factor a_D as:

$$\frac{\dot{a}_D^2}{a_D^2} + \frac{k_D}{a_D^2} = \frac{8\pi G}{3}\langle\rho\rangle_D + \frac{2}{3}\frac{\beta}{n+2}a_D^n, \tag{6.26}$$

$$\frac{\ddot{a}_D}{a_D} = -\frac{4\pi G}{3}\langle\rho\rangle_D + \frac{\beta}{3}a_D^n, \tag{6.27}$$

where the matter density evolves as $\langle\rho\rangle_D = \langle\rho\rangle_i/a_D^3$, in accordance with the continuity equation.

Analogous to standard FLRW cosmologies, we may define dimensionless, domain-dependent average cosmological parameters as follows:

$$\Omega_m = \frac{8\pi G}{3H_{D_0}^2}\langle\rho\rangle_0, \tag{6.28}$$

$$\Omega_k = -\frac{k_D}{H_{D_0}^2 a_{D_0}^2}, \tag{6.29}$$

$$\Omega_R = -\frac{1}{6H_{D_0}^2}\frac{\beta}{r}a_{D_0}^n, \tag{6.30}$$

$$\Omega_Q = -\frac{1}{6H_{D_0}^2}\beta a_{D_0}^n, \tag{6.31}$$

where H_{D_0} is the present-day Hubble parameter associated with the effective scale factor a_D, and subscript zero indicates evaluation at the present time. In light of Eqs. (6.26) and (6.27), these parameters satisfy the generalized expansion and acceleration equations expressed in terms of redshift z, defined via $1 + z = a_{D_0}/a_D$:

$$\left(\frac{H_D}{H_{D_0}}\right)^2 = \Omega_m(1+z)^3 + \Omega_k(1+z)^2 + (\Omega_R + \Omega_Q)(1+z)^{-n}, \tag{6.32}$$

$$\frac{\ddot{a}_D}{a_D} = -\frac{3}{2}H_{D_0}^2\Omega_m(1+z)^3 - 2H_{D_0}^2\Omega_Q(1+z)^{-n}. \tag{6.33}$$

These relations allow one to interpret the impact of averaged inhomogeneities and backreaction on cosmological dynamics in a form directly comparable to standard cosmological models.

In the following subsection, we use this reinterpretation to fit the Buchert expansion equation to our reconstructed Hubble function and assess the contribution of kinematical backreaction to the observed acceleration.

6.3. Fitting the Effective Hubble Parameter and Extracting Backreaction

Following the reinterpretation of our reconstructed expansion history within the Buchert formalism (as discussed previously on this section), we now use the averaged Raychaudhuri equation to fit a model Hubble parameter and assess the dynamical role of backreaction. Specifically, we fit our reconstructed effective Hubble function $H_D(z) \equiv \frac{\dot{a}_D}{a_D}$ to a modified version of the Friedmann equation, which incorporates both the averaged matter content and the effects of curvature and kinematical backreaction.

In analogy with previous sections, we define an effective energy balance equation in the form:

$$H_D^2(z) = H_{D_0}^2(\Omega_m(1+z)^3 + \Omega_X(1+z)^{-n}), \tag{6.34}$$

where:

- H_{D_0} is the present value of the effective Hubble parameter,
- Ω_m is the effective matter density parameter,
- $\Omega_X \equiv 1 - \Omega_m$ represents the total contribution from spatial curvature and kinematical backreaction, and
- n is a free parameter encoding the redshift dependence of this combined geometric term.

This form mimics a two-fluid model, where the second term behaves like a dark energy component with equation-of-state parameter $w_{\text{eff}} = -n/3 - 1$. Importantly, although this resembles phenomenological two-component models, we stress that Ω_X here includes both the kinematical backreaction Q_D and the averaged curvature $\langle R \rangle_D$, which are coupled through Buchert's integrability condition. Thus, Ω_X does not correspond to a physical fluid but rather to the net dynamical impact of inhomogeneities.

We fit this model to our reconstructed $H_D(z)$, which is obtained by averaging the $\dot{a}(z)$ curves from the 24 selected luminosity distance functions (as in Section 4). As in previous sections, we turn this into a set of 76 data points evenly spaced in redshift from $z = 0$ to $z = 1.5$, and we propagate the 1-σ uncertainty band from the representative fit y5-F3 to estimate the error bars on $H_D(z)$. The fit is performed using a nonlinear least-squares approach, treating all four parameters (H_{D_0}, Ω_m, Ω_X, n) as free, but enforcing the constraint $\Omega_m + \Omega_X = 1$ to ensure a consistent energy balance.

To isolate the role of backreaction, we choose the spatial curvature parameter $k_D = 0$ in the template metric. This sets the curvature of the effective geometry to zero,

but still allows for a nonzero average of the physical Ricci scalar $\langle R \rangle_D$, consistent with the Buchert framework. The influence of curvature inhomogeneities is thus absorbed into Ω_X.

The best-fit results are:

$$H_{D_0} \approx 73.37 \pm 0.24, \quad \Omega_m \approx 0.43 \pm 0.03, \quad \Omega_X \approx 0.57 \pm 0.03, \quad n \approx 0.65 \pm 0.02. \tag{6.35}$$

This fit provides a very good agreement with the reconstructed $H_D(z)$, and the inferred value of H_{D_0} agrees with the direct reconstruction within the precision of our method. The deviation of n from zero indicates a significant redshift dependence in the backreaction-curvature combination, with an effective fluid behavior corresponding to:

$$w_{\text{eff}} = -\frac{n}{3} - 1 \approx -1.22. \tag{6.36}$$

This value is consistent with an accelerating universe and shows that, within the Buchert framework, a significant portion of the observed acceleration can be accounted for by the combined effects of spatial curvature and inhomogeneity-induced backreaction.

A plot comparing the reconstructed $H_D(z)$ and its 1-σ confidence band to the best-fit model curve is shown in Figure 6.1. The visual agreement and low residuals confirm the robustness of the fit and demonstrate the potential of backreaction to mimic dark energy–like behavior in effective expansion dynamics.

To further test the sufficiency of this geometric explanation, we introduced an explicit cosmological constant term Ω_Λ alongside the backreaction-curvature component Ω_X and refitted the model. Remarkably, the fit returned $\Omega_\Lambda \approx 10^{-16}$, effectively zero, and remained statistically consistent even when the Hubble parameter H_0 was varied

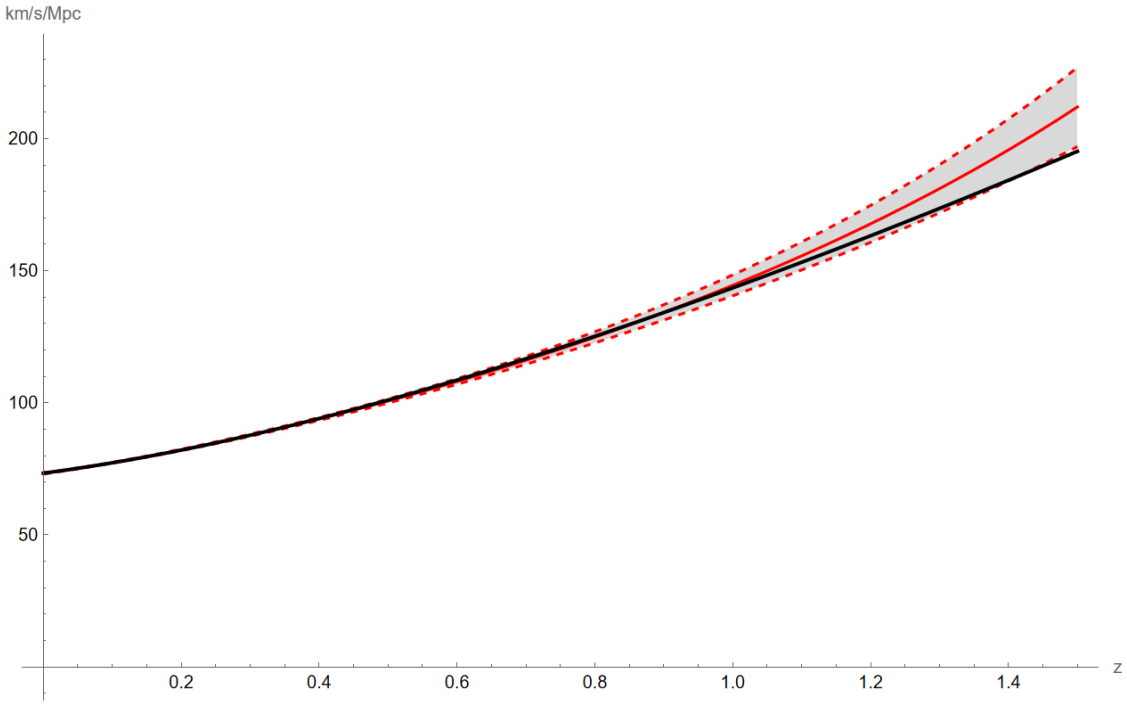


Figure 6.1. Reconstructed effective Hubble parameter $H_D(z)$, obtained by averaging the 24 accepted $\dot{a}(z)$ functions. The shaded region represents 1-σ confidence band derived from the y5–F3 representative function. The black curve shows the best-fit model of the form $H_D(z) = H_{D_0}\sqrt{\Omega_m(1+z)^3 + \Omega_X(1+z)^{-n}}$.

within reasonable bounds. This insensitivity to Λ supports the conclusion that the observed expansion might be fully accounted for by the inhomogeneous geometry encoded in the Buchert formalism, without invoking any additional dark energy component.

7. COORDINATE SYSTEM ADAPTED TO SUPERNOVA OBSERVATIONS

In this section, we reformulate the FLRW cosmology in a coordinate system that more naturally reflects the structure of supernova observations. Since Type Ia supernovae provide data in the form of luminosity distance $d_L(z)$ as a function of redshift, it is useful to develop a framework in which these observables directly inform the spacetime geometry. Our goal is to construct a coordinate system where both the time-like coordinate and the dynamical function of the metric are derived from observational quantities.

We begin with the standard FLRW metric:

$$ds^2 = -c^2dt^2 + a(t)^2\left[\frac{1}{1-kr^2}dr^2 + r^2d\Omega^2\right]. \tag{7.1}$$

Combining the null geodesic condition with the luminosity distance definition and the redshift–scale factor relation $1+z = \frac{a_0}{a}$, the look-back time can be expressed as:

$$t_0 - t = \int_0^z \frac{dz}{c(1+z)} \frac{1}{\sqrt{1-\kappa\frac{d_L^2}{(1+z)^2}}} \frac{d}{dz}\left(\frac{d_L}{1+z}\right), \tag{7.2}$$

$$\frac{dt}{dz} = -\frac{1}{c(1+z)} \frac{1}{\sqrt{1-\kappa\frac{d_L^2}{(1+z)^2}}} \frac{d}{dz}\left(\frac{d_L}{1+z}\right) \tag{7.3}$$

where $\kappa = \frac{k}{a_0^2}$ is the physical spatial curvature parameter.We then define a new variable,

$$y \equiv \frac{d_L(z)}{1+z}, \tag{7.4}$$

known as the photon-count distance, and introduce the function

$$b(y) = \frac{1}{c(1+z)\sqrt{1-\kappa y^2}}. \tag{7.5}$$

This transformation converts our original $(z, d_L(z))$ data into a new set of points (y_i, b_i) forming the dataset in the observation-adapted coordinate system. Since y depends on both redshift and luminosity distance, uncertainties in d_L propagate to the horizontal error bars. The vertical errors in $b(y)$ are negligible in comparison (often more than ten times smaller) and are ignored in the analysis. In the case $\kappa = 0$, the vertical error vanishes entirely (neglecting redshift uncertainties).

Our new observable dataset is thus (y_i, b_i), and we perform function fitting to reconstruct $b(y)$, the only free function in the metric once this transformation is made. From equation (7.3), we find

$$\frac{dt}{dz} = -b\frac{d}{dz}y, \quad \rightarrow \quad dt = -b(y)dy. \tag{7.6}$$

Additionally, combining equation (7.5) with the redshift–scale factor relation $a = \frac{a_0}{(1+z)}$, we can express the scale factor in terms of b and y:

$$b = \frac{a}{(a_0 c)\sqrt{1-\kappa y^2}} \rightarrow a(y) = (a_0 c)\sqrt{1-\kappa y^2}b(y), \tag{7.7}$$

We can now rewrite the FLRW metric in these new coordinates as:

$$ds^2 = c^2 b(y)^2 \left[-dy^2 + a_0^2\left(1 - \frac{k}{a_0^2}y^2\right)\left(\frac{1}{1-kr^2}dr^2 + r^2 d^2\Omega\right)\right]. \tag{7.8}$$

The four-velocity in this frame is given by:

$$u^\alpha = (-\frac{1}{b(y)}, 0, 0, 0), \qquad u_\alpha = (c^2 b(y), 0, 0, 0) \tag{7.9}$$

which remains future-directed even though $u^0 < 0$, since $y = 0$ is defined as the present, and y increases toward the past.

In this reformulated metric, the function $b(y)$ encodes all dynamical information, and the time-like coordinate is now an observable-derived quantity. This construction allows us to reconstruct the expansion history and metric geometry directly from data, without assuming a specific cosmological model.

When the spatial curvature is zero ($\kappa = 0$), the metric simplifies to a conformally flat form:

$$ds^2 = c^2 b(y)^2 \left[-dy^2 + a_0^2(dr^2 + r^2 d^2\Omega)\right], \tag{7.10}$$

in which $b(y)$ acts as an analogue of the conformal scale factor. This simplification provides both a consistency check and further motivation for working in this observational coordinate system.

7.1. Derivatives of the Scale Factor in the Transformed Frame

In the previous section, we introduced a reformulated version of the FLRW metric in which the time-like coordinate is given by the photon-count distance y, and the metric dynamics are encoded in a single function $b(y)$. To connect this framework to cosmological evolution, we now derive expressions for the scale factor a, its first time derivative $\dot{a}$, and its second derivative $\ddot{a}$, all expressed in terms of y and $b(y)$.

Recall that the differential relation between the original coordinate time t and the new coordinate y is:

$$dt = -b(y)dy. \tag{7.11}$$

This leads to the chain rule identities:

$$\frac{d}{dy} = -b\frac{d}{dt}, \quad \frac{d^2}{dy^2} = b^2\frac{d^2}{dt^2} + b\dot{b}\frac{d}{dt} \tag{7.12}$$

which in turn imply the relations:

$$b' = -b\dot{b}, \quad b'' = b^2\ddot{b} + b\dot{b}^2 \tag{7.13}$$

where primes denote derivatives with respect to y, and dots denote derivatives with respect to t, the coordinate time.

We can also invert the chain rule to express time derivatives in terms of y-derivatives:

$$\frac{d}{dt} = -\frac{1}{b}\frac{d}{dy}, \quad \frac{d^2}{dt^2} = \frac{1}{b^2}\frac{d^2}{dy^2} - \frac{b'}{b^3}\frac{d}{dy} \tag{7.14}$$

which yields:

$$\dot{a} = -\frac{1}{b}a' \quad \ddot{a} = \frac{1}{b^2}a'' - \frac{b'}{b^3}a'. \tag{7.15}$$

Using equation (7.6),

$$a = (a_0 c)b\sqrt{1-\kappa y^2}, \tag{7.16}$$

we compute:

$$\dot{a} = -a_0 c\left(\frac{b'}{b}\sqrt{1-\kappa y^2} - \frac{\kappa y}{\sqrt{1-\kappa y^2}}\right), \tag{7.17}$$

and

$$\ddot{a} = \frac{a_0 c}{b}\left[\frac{b''}{b}\sqrt{1-\kappa y^2} - \frac{b'\kappa y}{b\sqrt{1-\kappa y^2}} - \frac{b'^2}{b^2}\sqrt{1-\kappa y^2} - \frac{\kappa}{\sqrt{1-\kappa y^2}} - \frac{(\kappa y)^2}{(1-\kappa y^2)^{3/2}}\right]. \tag{7.18}$$

These expressions allow us to compute $\dot{a}$ and $\ddot{a}$ from the fitted function $b(y)$, giving a direct observational handle on the expansion rate and acceleration in this transformed frame. Unlike in traditional approaches, we do not require an explicit model for the matter or energy content of the universe. Instead, the function $b(y)$, obtained directly from data, determines the dynamics.

In particular, the transition redshift — the moment when the universe switches from decelerated to accelerated expansion — corresponds to the value of y for which $\ddot{y_T} = 0$, as given by equation (7.18). This can be located numerically from the reconstructed $b(y)$, and then mapped back to a redshift z using Eq. (7.5). This approach provides a clean and flexible tool to extract cosmic dynamics directly from observations, with minimal theoretical assumptions.

7.2. Acceleration from Scalar Quantities: A Coordinate-Invariant Perspective

The results of the previous subsection provide a method for reconstructing the expansion history and identifying the acceleration of the universe using the coordinate system y and the function $b(y)$. However, these expressions rely explicitly on coordinate-based definitions of time and derivatives. In this section, we seek to formulate a coordinate-invariant expression for acceleration, constructed purely from scalar quantities.

We begin with the well-known Friedmann equations for a homogeneous and isotropic universe:

$$\left(\frac{\dot{a}}{a}\right)^2 = \left(\frac{8\pi G}{3c^2}\rho - \frac{kc^2}{a^2}\right), \quad \frac{\ddot{a}}{a} = -\frac{4\pi G}{3c^2}(\rho + 3p). \tag{7.19}$$

In our reformulated metric, the function $b(y)$ determines the metric's time scaling, but $b''(y)$ by itself does not have a clear interpretation as physical acceleration. To address this, we express the right-hand side of the acceleration equation — which determines $\ddot{a}/a$ — in terms of scalar contractions of the energy-momentum tensor.

Assuming a perfect fluid with 4-velocity u^α, the following scalar combinations are relevant:

$$T^\alpha_\alpha = -\rho + 3p, \quad T_{\alpha\beta}u^\alpha u^\beta = \rho c^2. \tag{7.20}$$

Combining these, we obtain:

$$\rho + 3p = 2T_{\alpha\beta}u^\alpha u^\beta \frac{1}{c^2} + T^\alpha_\alpha. \tag{7.21}$$

Using Einstein equations $G_{\alpha\beta} = \frac{8\pi G}{c^4}T_{\alpha\beta}$, this becomes:

$$\rho + 3p = \frac{c^4}{8\pi G}\left(2G_{\alpha\beta}u^\alpha u^\beta \frac{1}{c^2} + G^\alpha_\alpha\right). \tag{7.22}$$

Substituting into the acceleration equation gives:

$$\frac{\ddot{a}}{a} = -\frac{4\pi G}{3c^2}\left[\frac{c^4}{8\pi G}\left(2G_{\alpha\beta}u^\alpha u^\beta \frac{1}{c^2} + G^\alpha_\alpha\right)\right]. \tag{7.23}$$

Thus, we arrive at a coordinate-invariant expression for the acceleration:

$$\frac{\ddot{a}}{a} = -\frac{c^2}{6}\left[2G_{\alpha\beta}u^\alpha u^\beta \frac{1}{c^2} + G^\alpha_\alpha\right]. \tag{7.24}$$

This result can be evaluated for any metric, including our modified form in equation (7.8). In the case of our reformulated metric, we use the 4-velocity:

$$u^\alpha = \left(-\frac{1}{b(y)}, 0, 0, 0\right) \tag{7.25}$$

which remains future-directed due to the definition of the coordinate y. The contraction $G_{\alpha\beta}u^\alpha u^\beta$ and the trace G^α_α can be calculated using the components of the Einstein tensor derived from the metric expressed in terms of $b(y)$. This provides a second, independent method for computing $\ddot{a}/a$ as a function of y, without relying on the time derivative expressions derived in Section 7.1.

As shown in later chapters, both this invariant method and the coordinate-based method yield consistent results for the transition point y_T where $\ddot{a} = 0$, validating the robustness of our reconstruction approach.

7.3. Scalar and Tensor Quantities in the Transformed Frame

In this section, we derive and analyze several physically relevant quantities in our observationally adapted coordinate system. These include the expansion scalar Θ, the Hubble function $H(y)$, and the components of the Einstein tensor $G_{\alpha\beta}$, all expressed in terms of the reconstructed function $b(y)$. Some of these quantities — such as Θ and the proper-time definition of H — are scalars and therefore coordinate-invariant, while others, like the Einstein tensor components, are coordinate-dependent but crucial for connecting geometry to the energy-momentum content via Einstein's equations.

7.3.1. Expansion Scalar

The expansion scalar $\Theta \equiv \nabla_\alpha u^\alpha$ is a key coordinate-invariant quantity in cosmology, describing the local volume expansion of a congruence of comoving observers. It is defined as the divergence of the four-velocity:

$$\Theta = u^\alpha_{;\alpha} = \partial_\alpha u^\alpha + \Gamma^\alpha_{\alpha\beta} u^\beta. \tag{7.26}$$

In our transformed coordinate system with the metric:

$$ds^2 = c^2 b(y)^2 \left[-dy^2 + a_0^2 \left(1 - \frac{k}{a_0^2} y^2\right) \left(\frac{1}{1-kr^2} dr^2 + r^2 d^2\Omega \right) \right], \tag{7.27}$$

the four-velocity is:

$$u^{\alpha} = (-\frac{1}{b(y)}, 0, 0, 0). \tag{7.28}$$

Because the only non-zero component of u^{α} is the temporal one, the expansion scalar simplifies to:

$$\Theta = \partial_0 u^0 + u^0 \Gamma^{\alpha}_{\alpha 0}. \tag{7.29}$$

Computing the Christoffel symbols for this metric yields:

$$\Gamma^{\alpha}_{\alpha 0} = \left(\frac{4b'}{b} - \frac{3\kappa y}{1-\kappa y^2} \right), \tag{7.30}$$

so the expansion scalar becomes:

$$\Theta = -\frac{1}{b} \left(\frac{3b'}{b} - \frac{3\kappa y}{1-\kappa y^2} \right). \tag{7.31}$$

This expression reflects the instantaneous local expansion rate of comoving worldlines in terms of the observationally determined function $b(y)$.

To study the dynamical behavior of this expansion, we also compute its proper-time derivative. Since proper time satisfies $d\tau = dt = -b(y)dy$, we have:

$$\dot{\Theta} = \frac{d\Theta}{d\tau} = -\frac{1}{b}\frac{\Theta}{dy}. \tag{7.32}$$

Differentiating equation (7.31) gives:

$$\begin{aligned} \dot{\Theta} &= -\frac{1}{b}\frac{d\Theta}{dy} \\ &= -\frac{1}{b}\left[\frac{3b'}{b^2}\left(\frac{b'}{b} - \frac{\kappa}{1-\kappa y^2} \right) - \frac{3}{b}\left(\frac{b''}{b} - \left(\frac{b'}{b} \right)^2 - \frac{\kappa}{1-\kappa y^2} - 2\frac{\kappa^2 y^2}{(1-\kappa y^2)^2} \right) \right]. \end{aligned} \tag{7.33}$$

This quantity represents the local rate of change of the expansion scalar with respect to proper time. Importantly, since both Θ and $\dot{\Theta}$ are scalars, these expressions are independent of the specific coordinate system and offer an invariant characterization of cosmic dynamics.

7.3.2. Hubble Function

The Hubble parameter describes the expansion rate of the universe and is traditionally defined as the fractional rate of change of the scale factor with respect to proper time:

$$H(t) = \frac{\dot{a}(t)}{a(t)}. \tag{7.34}$$

In our framework, we begin by expressing $\dot{a}(y)$ using equation (7.17) and divide it by $a(y)$ (from equation (7.7)) to obtain the Hubble function directly in terms of the coordinate y:

$$H(y) = \frac{\dot{a}}{a} = -\frac{1}{b}\left(\frac{b'}{b} - \frac{\kappa y}{1-\kappa y^2}\right). \tag{7.35}$$

This expression is also equal to $\frac{1}{3}\Theta$, consistent with the interpretation of H as the average expansion rate for an isotropic flow.

To further validate this result from a geometric standpoint, we consider the physical radial length scale l associated with the spatial part of the metric. From equation (7.8), we define the proper radial length as:

$$l = a_0 c b(y)\sqrt{1-\kappa y^2}\int \frac{dr}{\sqrt{1-kr^2}}, \tag{7.36}$$

which includes the y-dependence from both $b(y)$ and the curvature correction.

Differentiating $l(y)$ with respect to y, we find:

$$\frac{dl}{dy} = a_0 c \int \frac{dr}{\sqrt{1-kr^2}} \left(b' \sqrt{1-\kappa y^2} - \frac{b\kappa y}{\sqrt{1-\kappa y^2}} \right). \tag{7.37}$$

This allows us to define a generalized Hubble function, denoted $\mathcal{H}_y(y)$, as the logarithmic derivative of length with respect to y:

$$\mathcal{H}_y(y) = \frac{l'}{l} = \left(\frac{b'}{b} - \frac{\kappa y}{1-\kappa y^2} \right). \tag{7.38}$$

This function describes how spatial distances change with respect to the observational coordinate y, but does not account for proper time. Initially, it appears to differ from the Hubble function obtained via $\dot{a}/a$.

However, recognizing that proper time in this metric satisfies $d\tau = dt = -b(y)dy$, we compute the physically meaningful Hubble parameter using:

$$H(y) = \frac{1}{l}\frac{dl}{d\tau} = -\frac{1}{b(y)}\frac{l'}{l} = -\frac{1}{b}\left(\frac{b'}{b} - \frac{\kappa y}{1-\kappa y^2} \right). \tag{7.39}$$

7.3.3. Einstein Equation

To complete our formulation, we evaluate the Einstein tensor $G_{\alpha\beta}$ for the metric written in terms of the observational coordinate y and the function $b(y)$. This provides a direct link between the reconstructed spacetime geometry and the energy-momentum content of the universe through Einstein's field equations:

$$G_{\alpha\beta} = \frac{8\pi G}{c^4} T_{\alpha\beta}. \tag{7.40}$$

We assume a perfect fluid energy-momentum tensor:

$$T_{\alpha\beta} = \frac{1}{c^2}\left(\rho + p\right) u_\alpha u_\beta + p g_{\alpha\beta}, \tag{7.41}$$

where ρ is the energy density and p is the pressure. For the metric

$$ds^2 = c^2 b(y)^2 \left[-dy^2 + a_0^2 \left(1 - \frac{k}{a_0^2} y^2\right) \left(\frac{1}{1-kr^2} dr^2 + r^2 d^2\Omega \right) \right], \tag{7.42}$$

the non-zero components of the Einstein tensor are computed to be:

$$G_0^0 = \frac{3\kappa}{c^2(1-\kappa y^2)^2 b(y)^2} - \frac{6\kappa y b'(y)}{c^2(1-\kappa y^2) b(y)^3} + \frac{3b'(y)^2}{c^2 b(y)^4}, \tag{7.43}$$

$$G_1^1 = G_2^2 = G_3^3 = \frac{\kappa b(y)^2 + (1-\kappa y^2)^2 b'(y)^2 + 2(1-\kappa y^2) b(y)(2\kappa y b'(y) - (1-\kappa y^2) b''(y))}{c^2(1-\kappa y^2)^2 b(y)^4}. \tag{7.44}$$

Using these expressions, we can express the energy density ρ and pressure p in terms of $b(y)$ and its derivatives. First, from equation (7.39), we rewrite the Friedmann-like relation for the Hubble parameter as:

$$H^2 = \frac{8\pi G}{3c^2}\rho - \frac{1}{b(y)^2} \frac{\kappa}{1-\kappa y^2} \tag{7.45}$$

which mirrors the first Friedmann equation but with curvature and expansion expressed in terms of y and $b(y)$. Similarly, combining G_0^0 and G_1^1 , we find:

$$-G_0^0 + 3G_1^1 = \frac{8\pi G}{c^4} (\rho + 3p) \tag{7.46}$$

which gives:

$$\rho + 3p = \frac{6c^2}{8\pi G b(y)^2} \left(\frac{\kappa}{(1-\kappa y^2)^2} + \frac{\kappa y}{1-\kappa y^2} \frac{b'(y)}{b(y)} + \left(\frac{b'(y)}{b(y)} \right)^2 - \frac{b''(y)}{b(y)} \right). \tag{7.47}$$

7.4. Theoretical Construction and Fitting of $b(y)$

With the theoretical framework in place, we now proceed to extract and analyze the function $b(y)$ using combined Pantheon+ and calibrated GRB data, as introduced

in Section 2. The aim is twofold:

- To construct a theoretical prediction for $b(y)$ under the assumption of a spatially flat ΛCDM cosmology,
- To compare this with empirical fits to the transformed observational data y_i, b_i, assessing the accuracy and stability of both approaches.

Due to the definition of $b(y)$, which involves the square root $\sqrt{1-\kappa y^2}$, the transformed data and the allowed domain of y depend on the spatial curvature $\kappa = \frac{k}{a_0^2}$. For large values of y, especially with positive curvature, $b(y)$ may become imaginary. To avoid this, and for consistency with earlier sections, we adopt a fiducial curvature radius of $a_0 = 10,000$ Mpc and consider:

$$k = (-0.1, 0, 0.1), \ \rightarrow \ \kappa = \left(-\frac{0.1}{10000^2}, 0, \frac{0.1}{10000^2}\right). \tag{7.48}$$

Although positive curvature limits the maximum usable value of y, the negative curvature case allows arbitrarily large y. For symmetry and consistency, however, we apply the same magnitude of curvature in both directions. In the analysis that follows, we primarily work with the spatially flat case ($\kappa = 0$), both for simplicity and because the theoretical prediction and empirical data align most naturally in this regime.

7.4.1. Constructing Theoretical $b(y)$ from ΛCDM

In a spatially flat ΛCDM universe, the Hubble parameter is given by:

$$H(z) = H_0\sqrt{\Omega_m(1+z)^3 + (1-\Omega_m)} \tag{7.49}$$

where H_0 is the present-day Hubble constant, and Ω_m is the matter density parameter. The corresponding luminosity distance is:

$$d_L(z) = (1+z)\frac{c}{H_0}\int_0^z \frac{dz'}{\sqrt{\Omega_m(1+z')^3 + (1-\Omega_m)}}, \tag{7.50}$$

from which we compute the photon-count distance:

$$y(z) = \frac{d_L(z)}{1+z} = \frac{c}{H_0}\int_0^z \frac{dz'}{\sqrt{\Omega_m(1+z')^3 + (1-\Omega_m)}}. \tag{7.51}$$

We evaluate this integral numerically over a grid of redshifts and construct the inverse function $z(y)$ via interpolation[1] . Substituting into the definition of $b(y)$ for the flat case (from equation (7.5)):

$$b(y) = \frac{1}{c(1+z(y))}, \tag{7.52}$$

yields the theoretical prediction of $b(y)$ for a flat ΛCDM universe, expressed in the observational coordinate y.

The function $z(y)$ is constructed numerically via inversion of the integral for photon-count distance, and interpolated using standard spline methods. This is consistent with the interpolation methods employed in cosmological data analysis, including [38], where luminosity or expansion functions are reconstructed from gridded values using smooth interpolation.

We adopt the best-fit cosmological parameters $H_0 \approx 73$ km/s/Mpc and $\Omega_m \approx 0.37$, obtained from prior fits to the combined Pantheon+ and GRB datasets. Using these, we numerically compute $y(z)$, invert to get $z(y)$, and then evaluate $b(y)$. This gives a smooth, model-based prediction for comparison with the observationally transformed (y_i, b_i) data.

To analyze acceleration, we compute $\ddot{a}(y)$ using the reconstructed $b(y)$ and the expression derived in equation 7.18. The point y_T at which $\ddot{a}(y_T) = 0$ marks the transition from deceleration to acceleration. This is converted to a transition redshift

[1] All interpolated functions are constructed using Mathematica's default cubic spline interpolation to ensure smooth differentiability.

z_T using:

$$b(y) = \frac{1}{c(1+z)}, \qquad z = \frac{1}{cb(y)} - 1. \tag{7.53}$$

Using the theoretical $b(y)$ curve, we find $y_T \approx 1782$, corresponding to $z_T \approx 0.50$, in agreement with previous analysis (see Section 3.3).

We also tested the consistency of the two approaches presented in Sections 8.1 and 8.2 for evaluating acceleration. Specifically, we computed the quantity $\frac{\ddot{a}}{a}(y)$ using:

- The coordinate-based method from Section 7.1, which expresses $\ddot{a}(y)$ and $a(y)$ explicitly in terms of $b(y)$ and its derivatives, and
- The coordinate-invariant method from Section 7.2, which reconstructs $\frac{\ddot{a}}{a}(y)$ from scalar contractions of the Einstein tensor using the four-velocity u^α.

Both methods were applied to the same reconstructed $b(y)$ derived from ΛCDM, and both yielded an identical transition point $y_T \approx 1782$. This numerical agreement confirms the internal consistency of our geometric reformulation and validates the use of either method for probing acceleration in the transformed framework. Although the two curves for $\frac{\ddot{a}}{a}(y)$ visually overlap, the agreement in their zero-crossing point (transition to acceleration) provides a strong consistency check on the framework. Figure 7.1 illustrates the near-perfect overlap between the two expressions for $\frac{\ddot{a}}{a}(y)$, further reinforcing this result.

7.4.2. Empirical Fitting of $b(y)$

We now compare the theoretical $b(y)$ to direct empirical fits using the transformed data points (y_i, b_i). We tested several functional forms for fitting. However, many of these produced unphysical behaviors when second derivatives were computed — including non-real or always-positive acceleration. Only two fitting forms produced physically plausible $\ddot{a}(y)$ profiles:

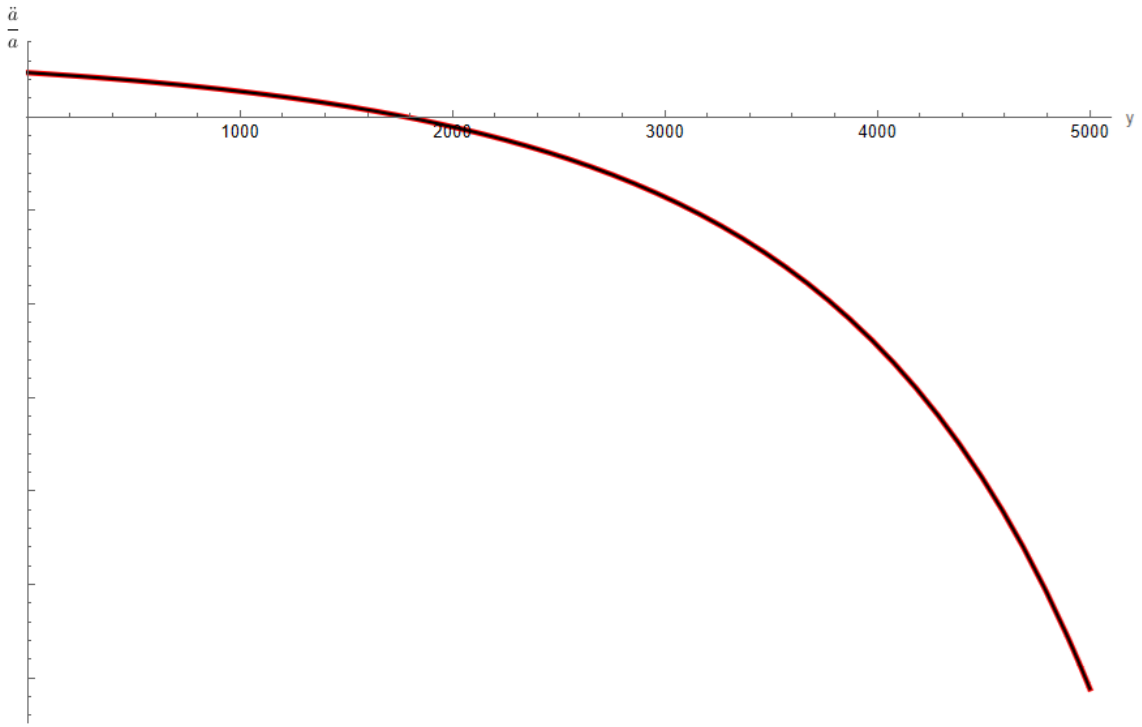


Figure 7.1. Comparison of the coordinate-based (black) and coordinate-invariant (red, thick) computations of the cosmic acceleration $\frac{\ddot{a}}{a}(y)$, both using the ΛCDM-derived $b(y)$. The two curves are numerically indistinguishable, confirming the internal consistency of the two reconstruction approaches. The transition point $y_T \approx 1782$ is identical in both cases.

- A fourth-order polynomial:

$$b_{\text{poly}}(y) = \frac{1}{c} + c1y + c2y^2 + c3y^3 + c4y^4, \tag{7.54}$$

- A two-parameter Padé approximation:

$$b_{\text{padé}}(y) = \frac{1/c + c1y}{1 + c2y}. \tag{7.55}$$

The coefficients c_i are determined using Mathematica's NonlinearModelFit with weights proportional to the inverse square of the propagated horizontal errors σ_y^2. While this does not constitute a full orthogonal distance regression, it is a reasonable approximation here, as the dominant uncertainties are in y, not b.

In Figure 7.2, we compare:

- The observational data,
- The flat ΛCDM-based $b(y)$,
- And the best-fitting Padé curve.

All three agree closely for $y < 2000$, but diverge slightly at higher values of y. These small differences, however, significantly affect the computed acceleration due to the sensitivity of $\ddot{a}(y)$ to second derivatives.

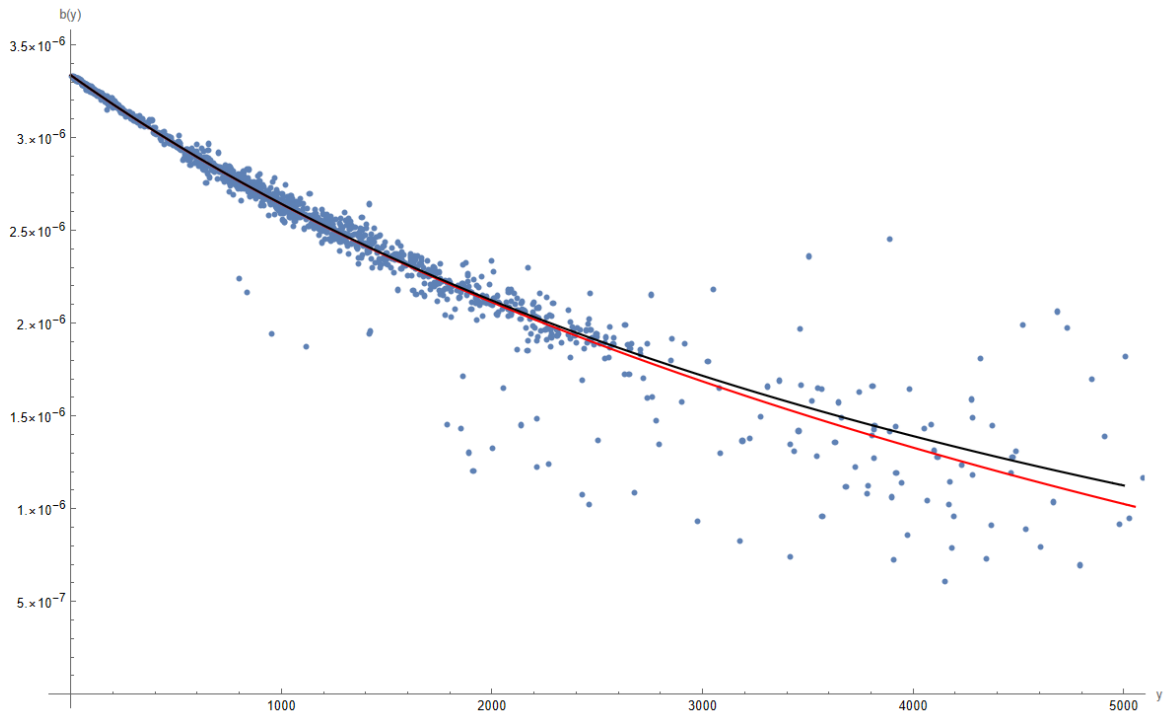


Figure 7.2. Comparison of the observationally transformed data (y_i, b_i), red curve is the theoretical $b(y)$ curve derived from a flat ΛCDM model, and black curve is the empirical Padé fit. All curves closely agree for $y < 2000$, but begin to diverge at larger values of y. This subtle divergence leads to significant differences in the second derivative $\ddot{a}(y)$, as shown in Figure 7.3

.

Notably, the Padé fit predicts a much later acceleration transition: $y_T \approx 3481$, corresponding to $z_t \approx 1.15$. This contrasts sharply with the ΛCDM-based $z_T = 0.50$, despite the two fits appearing similar at first glance. This discrepancy underscores the importance of a physically motivated functional form when evaluating higher-order derivatives from data.

Because of this sensitivity, and the strong agreement of the ΛCDM-derived $b(y)$ with observations, we include it alongside the Padé fit in our calculation of $\ddot{a}(y)$ to illustrate how even small differences in the reconstructed function can lead to significant differences in the inferred acceleration history (see Figure 7.3).

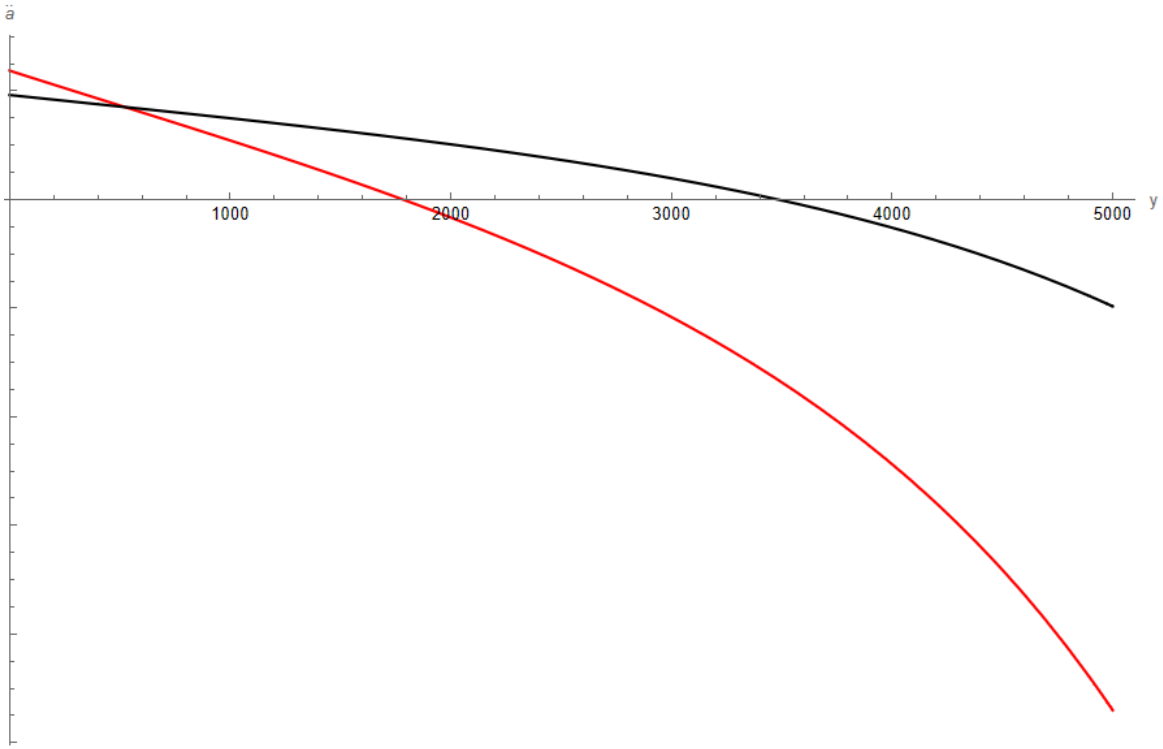


Figure 7.3. Acceleration profile $\ddot{a}(y)$ computed from two fitted models of $b(y)$. The red curve corresponds to the ΛCDM-predicted $b(y)$; the black curve is computed from the empirical Padé fit. Although both models produce nearly indistinguishable b(y) curves (Figure 7.2), the resulting acceleration profiles differ significantly, showing the high sensitivity of $\ddot{a}(y)$ to the form of $b(y)$.

This comparison highlights a central insight of our framework: although different functional forms for $b(y)$ may offer similar fits to the observational data, their implications for cosmic acceleration can diverge significantly. Because the second derivative $\ddot{a}(y)$ is highly sensitive to the detailed structure of $b(y)$, empirical fits—especially those not physically constrained—can lead to unstable or unphysical acceleration histories. In contrast, the ΛCDM-derived $b(y)$ not only provides a stable result but also yields a transition point $y_T \approx 1782$, corresponding to $z_T \approx 0.5$, which is in close agreement with the value reported previously in Section 3.3.

8. A DYNAMICALLY-WARPED METRIC WITH STEADY PHYSICAL PROPERTIES

In this section, we investigate a class of inhomogeneous and anisotropic spacetimes that exhibit an unusual and counterintuitive set of physical characteristics. Specifically, we present a metric whose components depend exponentially on time but yield time-independent curvature invariants and stress-energy components. We found this interesting family while trying to construct a spacetime with structure formation where at least some (exact) metric components and stress-energy-momentum variables can be analytically averaged. One would then compare the time-evolution of the exact quantities and that of the averaged ones.

That search was unsuccessful for the time being, but consider the diagonal spacetime metric:

$$ds^2 = -dt^2 + e^{tf(x)}dx^2 + e^{tg(y)}dy^2 + e^{th(z)}dz^2 \tag{8.1}$$

where $f(x), g(y)$ and $h(z)$ are arbitrary real-valued functions. The exponential dependence on time suggests dynamical evolution, but the spacetime reveals steady behavior under physical scrutiny.

Despite the inhomogeneity and anisotropy, the spatial slices at constant are flat. That is the induced 3-metric

$$h_{ij} = \text{diag}(e^{tf(x)}, e^{tg(y)}, e^{th(z)}) \tag{8.2}$$

has vanishing intrinsic curvature. Thus, the spatial geometry is flat in the Riemannian sense, even though the metric appears highly warped.

We compute several curvature scalars and find that they are all independent of time. These include: The Kretschmann scalar $R^{\alpha\beta\gamma\delta}R_{\alpha\beta\gamma\delta}$, the Ricci-square contraction $R^{\alpha\beta}R_{\alpha\beta}$, the Ricci scalar R,

$$R^{\alpha\beta\gamma\delta}R_{\alpha\beta\gamma\delta} = \frac{1}{4}(f(x)^4 + g(y)^4 + h(z)^4 + f(x)^2g(y)^2 + f(x)^2h(z)^2 + g(y)^2h(z)^2), \quad (8.3)$$

$$R^{\alpha\beta}R_{\alpha\beta} = \frac{1}{16}(f(x)^2(f(x) + g(y) + h(z))^2 + g(y)^2(f(x) + g(y) + h(z))^2 \quad (8.4)$$

$$+ h(z)^2(f(x) + g(y) + h(z))^2 + (f(x)^2 + g(y)^2 + h(z)^2)^2), \quad (8.5)$$

$$R = \frac{1}{2}(f(x)^2 + g(y)^2 + h(z)^2 + g(y)h(z) + f(x)g(y) + f(x)h(z)) \quad (8.6)$$

and all components of the Einstein tensor G^{α}_{β}

$$G^0_0 = -\frac{1}{4}(f(x)g(y) + f(x)h(z) + g(y)h(z)), \quad (8.7)$$

$$G^1_1 = -\frac{1}{4}(g(y)^2 + g(y)h(z) + h(z)^2), \quad (8.8)$$

$$G^2_2 = -\frac{1}{4}(f(x)^2 + f(x)h(z) + h(z)^2), \quad (8.9)$$

$$G^3_3 = -\frac{1}{4}(f(x)^2 + f(x)g(y) + g(y)^2). \quad (8.10)$$

This time independence results from precise cancellations in the derivatives of the metric, despite its explicit exponential dependence on t.

We identify comoving observers with 4-velocity $u^{\alpha} = (1, 0, 0, 0)$, who follow geodesics due to the constancy of the lapse and the absence of shift vectors. The Einstein tensor components suggest an energy-momentum tensor of the form:

$$T^{\alpha}_{\beta} = \mathrm{diag}(\rho, p_x, p_y, p_z), \quad (8.11)$$

where:

$$\rho = \frac{1}{32\pi G}(fg + fh + gh), \quad (8.12)$$

$$p_x = -\frac{1}{32\pi G}(g^2 + gh + h^2), \quad (8.13)$$

$$p_y = -\frac{1}{32\pi G}(f^2 + fh + h^2), \tag{8.14}$$

$$p_z = -\frac{1}{32\pi G}(f^2 + fg + g^2). \tag{8.15}$$

These expressions are also independent of time and vary spatially according to the functional forms of $f(x)$, $g(y)$, $h(z)$. The matter content can thus be interpreted as an anisotropic and inhomogemeous fluid.

We can calculate expansion scalar for these observers $\Theta = \nabla_\alpha u^\alpha$, we get

$$\Theta = \frac{1}{2}(f(x) + g(y) + h(z)) \tag{8.16}$$

which is also time independent. Hubble parameters are given by $H_x = \frac{f}{2}$, $H_y = \frac{g}{2}$ and $H_z = \frac{h}{2}$.

8.1. SEC

A notable property of this spacetime is its guaranteed violation of the Strong Energy Condition (SEC). For comoving observers, the SEC requires:

$$\rho + p_x + p_y + p_z \geq 0. \tag{8.17}$$

For this metric, the combination evaluates to:

$$\rho + p_x + p_y + p_z = -\frac{1}{32\pi G}(f^2 + g^2 + h^2), \tag{8.18}$$

which is strictly negative. Thus, the Strong Energy Condition is violated for all real-valued nontrivial choices of the functions $f(x), g(y), h(z)$, as the combination $\rho + p_x + p_y + p_z$ is always strictly negative.

In contrast, the Weak Energy Condition depends on the specific spatial behavior of the functions. It requires $\rho \geq 0$ and $\rho + p_i \geq 0$ for $i = x, y, z$. These expressions involve combinations of products and squares of f, g, h, and can be either positive or negative depending on the choice of functions. Therefore, the WEC is not universally violated, but not guaranteed to hold either.

This metric presents a rare example of a spacetime with the following properties:

- Strong time dependence in its components
- Flat spatial slices despite inhomogeneity
- Time-independent curvature scalars and Einstein tensor
- Guaranteed violation of the Strong Energy Condition
- Matter source neither dilutes despite expansion, nor does it grow like phantom matter
- Inhomogeneous and anisotropic matter source constitutes structure, but no new structure formation despite existing seeds.

This spacetime seems to be an inhomogeneous/anisotropic generalization of deSitter, and its properties could be a useful toy model when exploring the role of SEC-violating matter in general relativity can also be seen as a structure-bearing version of the old steady-state models.

9. CONCLUSION

In this thesis, we have systematically developed, updated, and applied a model-independent framework—referred to as the spread–luminosity distance fitting (spread-LDF) method—for reconstructing the expansion history of the universe from observational data with minimal theoretical assumptions. Building upon our earlier work, we employed the improved Pantheon+ Type Ia supernova dataset alongside a rescaled gamma-ray burst (GRB) sample to extend the redshift coverage and enhance the stability of reconstructions. By fitting a diverse family of functional ansätze across several redshift reparameterizations and selecting optimal models via the Bayesian Information Criterion (BIC), we ensured statistical rigor and avoided overfitting.

Our updated reconstruction confirms a robust transition from decelerated to accelerated cosmic expansion at a redshift of approximately $z_T \approx 0.44^{+0.04}_{-0.03}$, assuming flat spatial geometry. This key result is consistent with the acceleration inferred in standard ΛCDM cosmology, but it emerges here entirely from the data and geometric structure of the FLRW metric, without invoking a specific matter or energy content. By analytically deriving the Hubble parameter and acceleration function from the reconstructed luminosity distance-redshift relation, we obtained a direct picture of the universe's expansion history.

We then introduced a semi-model-independent approach by assuming the validity of General Relativity, while still refraining from adopting a detailed model of the universe's matter-energy content. Through this, we derived effective energy density $\rho(z)$, pressure $p(z)$, and equation of state parameter $w(z)$ from the reconstructed expansion. Our results indicate that the observed acceleration cannot be explained by matter alone. Specifically, we found that the energy density significantly deviates from the matter-dominated scaling $\rho_m \propto (1+z)^3$ at low redshifts, requiring a component with negative pressure—consistent with dark energy or modified gravity effects. Quantita-

tively, we derived bounds such as $\Omega_m^{\max} \approx 0.48$ and $\Omega_\Lambda^{\min} \approx 0.52$, in good agreement with ΛCDM expectations, but obtained without assuming a cosmological constant.

Moreover, we also reconstructed the effective equation-of-state parameter $w(z)$. Our findings show that while the CPL parametrization agrees with the reconstructed curve within the estimated errors, it fails to reproduce the qualitative behaviour of $w(z)$, especially since we find that the pressure becomes positive for $z >\approx 1$. This mismatch emphasizes the limitations of commonly used dark energy parametrizations when interpreted too literally and highlights the utility of our concept of going back from the observations to contents of the universe, rather than from assumed contents to the observations. Furthermore, the finding of positive pressure for the cosmic fluid at $z >\approx 1$, if confirmed by future studies, will have profound implications on behaviour of Generalized Dark Energy; or alternatively, provide strong motivation for modified/alternative gravity theories.

Beyond homogeneous cosmologies, we investigated two major generalizations. First, we applied our reconstruction method to a class of radially inhomogeneous geometries by introducing a spatially varying curvature profile $b(r)$. We showed that such models can, in principle, mimic the effects of dark energy under certain conditions. By tuning $b(r)$, we identified profiles that yield zero or negative present-day acceleration, demonstrating that the inference of cosmic acceleration is sensitive to geometric assumptions. While such constructions may not be physically realistic, they emphasize the importance of carefully assessing homogeneity assumptions in interpreting observational data.

Second, we explored the implications of our reconstruction in the context of the Buchert averaging formalism, which addresses the impact of inhomogeneities on cosmic evolution. Treating the reconstructed Hubble parameter as an effective large-scale expansion rate, we computed the corresponding kinematical backreaction and averaged curvature. Using scaling ansätze for these quantities, we quantified how much of the observed acceleration could be attributed to averaging effects rather than a distinct

dark energy component. While our findings suggest that backreaction can, in principle, play a significant role, its capacity to fully replace dark energy depends on the validity of specific assumptions about the evolution of inhomogeneities—highlighting a key open question in cosmology.

In a further theoretical development, we reformulated the FLRW metric using a coordinate system adapted to supernova observations. By rewriting the metric in terms of a new variable y derived from photon-count distance, and fitting the corresponding function $b(y)$ directly to data, we constructed a data-driven description of spacetime geometry. This approach offers a novel way to encode observational information directly into the metric and may prove useful for future efforts in cosmographic reconstruction.

Finally, we presented a toy model metric with strong time-dependence in the metric components but time-independent curvature and stress-energy quantities. This peculiar configuration violates the Strong Energy Condition while preserving a steady physical content, and may serve as a simplified testbed for studying SEC-violating dynamics or exotic cosmological fluids.

Taken together, the results of this thesis reaffirm that much of the key information about the universe's expansion can be extracted with minimal theoretical bias, using only the assumption of metric gravity and observational data. However, we also demonstrate that the interpretation of this expansion—particularly the necessity of dark energy—is contingent on the assumptions about geometry, averaging, and gravity theory.

REFERENCES

1. Henderson, T., "On the Parallax of Alpha Centauri", *Memoirs of the Royal Astronomical Society*, Vol. 11, p. 61, 1840.

2. Filippenko, A. V., "Optical Spectra of Supernovae", *Annual Review of Astronomy and Astrophysics*, Vol. 35, No. 1, pp. 309–355, 1997.

3. Peebles, P. J. E., *Principles of Physical Cosmology*, Princeton University Press, Princeton, 2020.

4. Weinberg, S., *Cosmology*, OUP Oxford, Oxford, 2008.

5. Planck Collaboration, N. Aghanim *et al.*, "Planck 2018 Results. VI. Cosmological Parameters", *Astron. Astrophys*, Vol. 641, p. A6, 2020.

6. Riess, A. G., A. V. Filippenko, P. Challis, A. Clocchiatti, A. Diercks, P. M. Garnavich, R. L. Gilliland, C. J. Hogan, S. Jha, R. P. Kirshner, B. Leibundgut, M. M. Phillips, D. Reiss, B. P. Schmidt, R. A. Schommer, R. C. Smith, J. Spyromilio, C. Stubbs, N. B. Suntzeff and J. Tonry, "Observational Evidence from Supernovae for an Accelerating Universe and a Cosmological Constant", *The Astronomical Journal*, Vol. 116, No. 3, p. 1009, 1998.

7. S. Perlmutter, G. Aldering, G. Goldhaber, R. A. Knop, P. Nugent, P. G. Castro, S. Deustua, S. Fabbro, A. Goobar, D. E. Groom, I. M. Hook, A. G. Kim, M. Y. Kim, J. C. Lee, N. J. Nunes, R. Pain, C. R. Pennypacker, R. Quimby, C. Lidman, R. S. Ellis, M. Irwin, R. G. Mcmahon, P. Ruiz-Lapuente, N. Walton, B. Schaefer, B. J. Boyle, A. V. Filippenko, T. Matheson, A. S. Fruchter, N. Panagia, H. J. M. Newberg and W. J. Couch, "Measurements of Ω and Λ from 42 High-Redshift Supernovae", *The Astrophysical Journal*, Vol. 517, No. 2, p. 565, 1999.

8. Trotta, R., "Bayes in the Sky: Bayesian Inference and Model Selection in Cosmol-

ogy", *Contemporary Physics*, Vol. 49, No. 2, pp. 71–104, 2008.

9. Visser, M., "Jerk, Snap and the Cosmological Equation of State", *Classical and Quantum Gravity*, Vol. 21, No. 11, p. 2603, 2004.

10. Capozziello, S., R. Lazkoz and V. Salzano, "Comprehensive Cosmographic Analysis by Markov Chain Method", *Physical Review D—Particles, Fields, Gravitation, and Cosmology*, Vol. 84, No. 12, p. 124061, 2011.

11. Semiz, İ. and A. K. Çamlıbel, "What Do the Cosmological Supernova Data Really Tell Us?", *Journal of Cosmology and Astroparticle Physics*, Vol. 2015, No. 12, p. 038, 2015.

12. Çamlıbel, A. K., İ. Semiz and M. A. Feyizoğlu, "Pantheon Update on a Model-Independent Analysis of Cosmological Supernova Data", *Classical and Quantum Gravity*, Vol. 37, No. 23, p. 235001, 2020.

13. Scolnic, D. M., D. O. Jones, A. Rest, Y. C. Pan, R. Chornock, R. J. Foley, M. E. Huber, R. Kessler, G. Narayan, A. G. Riess, S. Rodney, E. Berger, D. Brout, P. J. Challis, M. Drout, D. Finkbeiner, R. Lunnan, R. P. Kirshner, N. E. Sanders, E. Schlafly, S. Smartt, C. W. Stubbs, J. Tonry, W. M. Wood-Vasey, M. Foley, J. Hand, E. Johnson, W. S. Burgett, K. C. Chambers, P. W. Draper, K. W. Hodapp, N. Kaiser, R. P. Kudritzki, E. A. Magnier, N. Metcalfe, F. Bresolin, E. Gall, R. Kotak, M. McCrum and K. W. Smith, "The Complete Light-Curve Sample of Spectroscopically Confirmed SNe Ia from Pan-STARRS1 and Cosmological Constraints from the Combined Pantheon Sample", *The Astrophysical Journal*, Vol. 859, No. 2, p. 101, 2018.

14. Starobinsky, A. A., "A New Type of Isotropic Cosmological Models without Singularity", *Physics Letters B*, Vol. 91, No. 1, pp. 99–102, 1980.

15. Buchert, T., "On Average Properties of Inhomogeneous Fluids in General Rela-

tivity: Dust Cosmologies", *General Relativity and Gravitation*, Vol. 32, No. 1, pp. 105–125, 2000.

16. Zalaletdinov, R. M., "Averaging Out the Einstein Equations", *General Relativity and Gravitation*, Vol. 24, No. 10, pp. 1015–1031, 1992.

17. Zalaletdinov, R. M., "Towards a Theory of Macroscopic Gravity", *General Relativity and Gravitation*, Vol. 25, No. 7, pp. 673–695, 1993.

18. Brout, D., D. Scolnic, B. Popovic, A. G. Riess, J. Zuntz, R. Kessler, A. Carr, T. M. Davis, S. Hinton, D. Jones, W. D. Kenworthy, E. R. Peterson, K. Said, G. Taylor, N. Ali, P. Armstrong, P. Charvu, A. Dwomoh, A. Palmese, H. Qu, B. M. Rose, C. W. Stubbs, M. Vincenzi, C. M. Wood, P. J. Brown, R. Chen, K. Chambers, D. A. Coulter, M. Dai, G. Dimitriadis, A. V. Filippenko, R. J. Foley, S. W. Jha, L. Kelsey, R. P. Kirshner, A. Möller, J. Muir, S. Nadathur, Y.-C. Pan, A. Rest, C. Rojas-Bravo, M. Sako, M. R. Siebert, M. Smith, B. E. Stahl and P. Wiseman, "The Pantheon+ Analysis: Cosmological Constraints", *The Astrophysical Journal*, Vol. 938, No. 2, p. 110, 2022.

19. Demianski, M., E. Piedipalumbo, D. Sawant and L. Amati, "Cosmology with Gamma-Ray Bursts-i. the Hubble Diagram through the Calibrated Ep, i–Eiso Correlation", *Astronomy & Astrophysics*, Vol. 598, p. A112, 2017.

20. Riess, A. G., W. Yuan, L. M. Macri, D. Scolnic, D. Brout, S. Casertano, D. O. Jones, Y. Murakami, L. Breuval, T. G. Brink, A. V. Filippenko, S. Hoffmann, S. W. Jha, W. D. Kenworthy, G. Anand, J. Mackenty, B. E. Stahl and W. Zheng, "A Comprehensive Measurement of the Local Value of the Hubble Constant with 1 km s- 1 Mpc- 1 Uncertainty from the Hubble Space Telescope and the SH0ES Team", *The Astrophysical Journal Letters*, Vol. 934, No. 1, p. L7, 2022.

21. Buchert, T., J. Larena and J.-M. Alimi, "Correspondence Between Kinematical Backreaction and Scalar Field Cosmologies—the 'Morphon Field"', *Classical and*

Quantum Gravity, Vol. 23, No. 22, p. 6379, 2006.

22. Izzo, L., S. Capozziello, G. Covone and M. Capaccioli, "Extending the Hubble Diagram by Gamma Ray Bursts", *Astronomy & Astrophysics*, Vol. 508, No. 1, pp. 63–67, 2009.

23. Tripp, R., "A Two-Parameter Luminosity Correction for Type IA Supernovae", *Astronomy and Astrophysics, v. 331, p. 815-820 (1998)*, Vol. 331, pp. 815–820, 1998.

24. Gruber, C. and O. Luongo, "Cosmographic Analysis of the Equation of State of the Universe through Padé Approximations", *Physical Review D*, Vol. 89, No. 10, p. 103506, 2014.

25. Aviles, A., A. Bravetti, S. Capozziello and O. Luongo, "Precision Cosmology with Padé Rational Approximations: Theoretical Predictions Versus Observational Limits", *Physical Review D*, Vol. 90, No. 4, p. 043531, 2014.

26. Wei, H., X.-P. Yan and Y.-N. Zhou, "Cosmological Applications of Pade Approximant", *Journal of Cosmology and Astroparticle Physics*, Vol. 2014, No. 01, p. 045, 2014.

27. Moresco, M., L. Amati, L. Amendola, S. Birrer, J. P. Blakeslee, M. Cantiello, A. Cimatti, J. Darling, M. Della Valle, M. Fishbach, C. Grillo, N. Hamaus, D. Holz, L. Izzo, R. Jimenez, E. Lusso, M. Meneghetti, E. Piedipalumbo, A. Pisani, A. Pourtsidou, L. Pozzetti, M. Quartin, G. Risaliti, P. Rosati and L. Verde, "Unveiling the Universe with Emerging Cosmological Probes", *Living Reviews in Relativity*, Vol. 25, No. 1, p. 6, 2022.

28. Chevallier, M. and D. Polarski, "Accelerating Universes with Scaling Dark Matter", *International Journal of Modern Physics D*, Vol. 10, No. 02, pp. 213–223, 2001.

29. Linder, E. V., "Exploring the Expansion History of the Universe", *Physical Review*

Letters, Vol. 90, No. 9, p. 091301, 2003.

30. Barboza Jr, E. and J. Alcaniz, "A Parametric Model for Dark Energy", *Physics Letters B*, Vol. 666, No. 5, pp. 415–419, 2008.

31. Akarsu, Ö., J. D. Barrow, L. A. Escamilla and J. A. Vazquez, "Graduated Dark Energy: Observational Hints of a Spontaneous Sign Switch in the Cosmological Constant", *Physical Review D*, Vol. 101, No. 6, p. 063528, 2020.

32. Soriano, J. F., S. Wohlberg and L. A. Anchordoqui, "New Insights on a Sign-Switching Λ", *Physics of the Dark Universe*, Vol. 48, p. 101911, 2025.

33. Dainotti, M. G., S. Bhardwaj, C. Cook, J. Ange, N. Lamichhane, M. Bogdan, M. McGee, P. Nadolsky, M. Sarkar, A. Pollo and S. Nagataki, "GRB Redshift Classifier to Follow up High-redshift GRBs Using Supervised Machine Learning", *The Astrophysical Journal Supplement Series*, Vol. 277, No. 1, p. 31, 2025.

34. Trefoloni, B., E. Lusso, E. Nardini, G. Risaliti, A. Marconi, G. Bargiacchi, A. Sacchi, P. Pietrini and M. Signorini, "Quasars as Standard Candles-VI. Spectroscopic Validation of the Cosmological Sample", *Astronomy & Astrophysics*, Vol. 689, p. A109, 2024.

35. Lusso, E., G. Risaliti and E. Nardini, "Are Quasars Reliable Standard Candles?", *Astronomy & Astrophysics*, Vol. 697, p. A108, 2025.

36. Chung, C., S. Park, J. Son, H. Cho and Y.-W. Lee, "Strong Progenitor Age Bias in Supernova Cosmology–I. Robust and Ubiquitous Evidence from a Larger Sample of Host Galaxies in a Broader Redshift Range", *Monthly Notices of the Royal Astronomical Society*, Vol. 538, No. 4, pp. 3340–3350, 2025.

37. Paranjape, A. and T. Singh, "Explicit Cosmological Coarse Graining via Spatial Averaging", *General Relativity and Gravitation*, Vol. 40, No. 1, pp. 139–157, 2008.

38. Riess, A. G., S. A. Rodney, D. M. Scolnic, D. L. Shafer, L.-G. Strolger, H. C. Ferguson, M. Postman, O. Graur, D. Maoz, S. W. Jha, B. Mobasher, S. Casertano, B. Hayden, A. Molino, J. Hjorth, P. M. Garnavich, D. O. Jones, R. P. Kirshner, A. M. Koekemoer, N. A. Grogin, G. Brammer, S. Hemmati, M. Dickinson, P. M. Challis, S. Wolff, K. I. Clubb, A. V. Filippenko, H. Nayyeri, U. Vivian, D. C. Koo, S. M. Faber, D. Kocevski, L. Bradley and D. Coes, "Type Ia Supernova Distances at Redshift$>$ 1.5 from the Hubble Space Telescope Multi-Cycle Treasury Programs: the Early Expansion Rate", *The Astrophysical Journal*, Vol. 853, No. 2, p. 126, 2018.